"Probing the Higgs potential at current and future colliders"

Zhao, Xiaoran

ABSTRACT

The Higgs boson provides unique opportunities for searching for phenomena that go beyond the Standard Model (SM). Among the least known properties of the scalar sector of the SM is the shape of Higgs potential. In the SM, the cu- bic and quartic Higgs self-couplings are completely determined by the Fermi constant and the Higgs boson mass. Measuring the self-interactions is there- fore essential to first test the SM and then to interpret possible deviations. The overarching goal of this thesis is to present a detailed study of the feasibility of measuring Higgs boson self-couplings at current and future colliders. One of the main novelties of this work is the systematic exploration of the possibility of accessing information on the self-couplings through effects that appear the first time via loops. In particular, we establish a framework based on the effec- tive field theory approach that allows to consistently evaluate loop corrections in presence of deformations of the Higgs potential. This method allows to per- form consistent computations and then to combine indirect constraints coming from loops to direct measurements. This study encompasses not only the cur- rent LHC and planned HL-LHC, but also a future 100 TeV hadron collider, circular and linear e + e − colliders, and a futuristic muon collider.

CITE THIS VERSION

Zhao, Xiaoran. *Probing the Higgs potential at current and future colliders.* Prom. : Maltoni, Fabio http://hdl.handle.net/2078.1/240619

UCLouvain
Institut de recherche
en mathématique et physique

Probing the Higgs potential at current and future colliders

Doctoral dissertation presented by

Xiaoran Zhao

in fulfilment of the requirements for the degree of Doctor in Sciences

Jury de thèse

Prof. Fabio Maltoni (promoteur)	UCLouvain, Belgium
Prof. Vincent Lemaître (président)	UCLouvain, Belgium
Prof. Céline Degrande	UCLouvain, Belgium
Dr. Claude Duhr	CERN, Switzerland
Prof. Gudrun Heinrich	KIT, Germany

September 2020

Acknowledgements

First and foremost, I would like to express my very great appreciation and my deep gratitude to my supervisor Fabio Maltoni for his patient guidance, continuous encouragements and support during my years at UCLouvain. I really appreciate that Fabio always gave me useful advice and kind help whenever I need throughout all aspects of my PhD studies. He has taught me not only much knowledge of physics but also about how to manage and perform excellent research. Without his great guidance, the completion of this thesis would not have been possible.

I would especially like to express my deepest gratitude to Qi-Shu Yan for collaborations, stimulating discussions and a great help during the past seven years.

My sincere thanks goes to Claude Duhr for fruitful collaboration. I benefited a great deal from his insights and expertise.

I would like to thank Davide Pagani, Ambresh Shivaji, Zhengwen Liu for collaborations and enormous interesting discussions on physics, mathematics and beyond.

I would also particularly like to thank all members of my thesis committee, Claude Duhr, Céline Degrande, Vincent Lemaître, Gudrun Heinrich as well as Fabio. They have taken a large amount of time to evaluate my work and provided me with many insightful comments and questions, which have helped to improve this thesis significantly. Besides, I would also like to thank the members of my "comité d'accompagnement", Giacomo Bruno, Marino Gran, Claude Duhr as well as Fabio, for their time taken at every stage of my PhD studies.

I would also like to extend my gratitude to other friends from physics community, Cen, Hua-Sheng, Jian, Long, Long-Bin, and Yang, for various discussion and help.

I am grateful to all CP3 members, together they made an ideal workplace with an excellent academic atmosphere. In particular, I express my special thanks to Carinne for her excellent secretarial support and Jerome and Andres for their IT support.

I also acknowledge the kind hospitality of many institutes, including CERN theory division in Geneva, Galileo Galilei Institute in Florence, INFN Padova, IISER Mohali, and Mainz Institute for Theoretical Physics, where part of the work was done.

Last but not least, I would like to express my heartfelt thanks to my family for their love and unconditional support.

This work has received funding from the European Union's Horizon 2020 research and innovation programme as part of the Marie Skłodowska-Curie Innovative Training Network MCnetITN3 (grant agreement no. 722104).

Abstract

The Higgs boson provides unique opportunities for searching for phenomena that go beyond the Standard Model (SM). Among the least known properties of the scalar sector of the SM is the shape of Higgs potential. In the SM, the cubic and quartic Higgs self-couplings are completely determined by the Fermi constant and the Higgs boson mass. Measuring the self-interactions is therefore essential to first test the SM and then to interpret possible deviations. The overarching goal of this thesis is to present a detailed study of the feasibility of measuring Higgs boson self-couplings at current and future colliders. One of the main novelties of this work is the systematic exploration of the possibility of accessing information on the self-couplings through effects that appear the first time via loops. In particular, we establish a framework based on the effective field theory approach that allows to consistently evaluate loop corrections in presence of deformations of the Higgs potential. This method allows to perform consistent computations and then to combine indirect constraints coming from loops to direct measurements. This study encompasses not only the current LHC and planned HL-LHC, but also a future 100 TeV hadron collider, circular and linear e^+e^- colliders, and a futuristic muon collider.

Contents

1 Introduction

The Standard Model of particle physics is one of the most successful theories of physics. It describes the behavior of all the known elementary particles and three out of four fundamental interactions observed in Nature. It is the result of two theories formulated during the 20th Century. One is the electroweak theory based on the gauge symmetry group $SU(2)_L \times U(1)_L$, which unifies the electromagnetic and weak interactions. The other is quantum chromodynamics (QCD), which describes the strong interaction between quarks and gluons, based on the $SU(3)_c$ group.

The SM is a quantum field theory, where all particles are treated as excited states of fields. In the SM, there are two kinds of fields: the first are the matter fields, which correspond to particles with half-integer spins, called fermions; The second corresponding to particles with integer spins, called bosons.

The fermions are divided into two categories: one includes the quarks, which have color charges and participate in the strong interactions; the other includes the leptons, which are color neutral and only participate in the electroweak interactions. In the SM (with massless neutrinos), all fermions are considered to be Dirac fermions, *i.e.*, there exists an antiparticle with identical mass but opposite sign of its quantum numbers for every of them.

While the left-handed and right-handed fermions are symmetric under the strong interaction, they are in different representations under the EW group $SU(2)_L \times U(1)_Y$. In particular, they are represented as Dirac chiral fields. The left-handed components transform as doublets under the weak isospin group $SU(2)_L$, while the right-handed components transform as singlets. In detail, we have the following three doublets for the leptons:

$$L_L^i = \begin{pmatrix} \nu_e \\ e_L \end{pmatrix}, \begin{pmatrix} \nu_\mu \\ \mu_L \end{pmatrix}, \begin{pmatrix} \nu_\tau \\ \tau_L \end{pmatrix}, \tag{1.1}$$

where e_L, μ_L, τ_L are the three fields corresponding to the left-hand part of three charged leptons e^-, μ^-, τ^-, and ν_e, ν_μ, ν_τ correspond to the left-handed part of three neutral leptons (called neutrinos). Note that, if massless, right-handed neutrinos are singlets and thus decouple in the SM, and we only consider the right-handed charged leptons

$$e_R^i = e_R, \mu_R, \tau_R. \tag{1.2}$$

Similarly we have the left-handed doublets for the quarks:

$$Q_L = \begin{pmatrix} u_L \\ d_L \end{pmatrix}, \begin{pmatrix} c_L \\ s_L \end{pmatrix}, \begin{pmatrix} t_L \\ b_L \end{pmatrix}, \tag{1.3}$$

and right-handed quarks

$$u_R^i = u_R, c_R, t_R \tag{1.4}$$

$$d_R^i = d_R, s_R, b_R \,. \tag{1.5}$$

The kinetic term of fermions in the Lagrangian is given by

$$\mathcal{L}^{\text{fermion},kin} = \sum_{f=L,e_R,Q_L,u_R,d_R} \bar{f} i \not{\partial} f \,. \tag{1.6}$$

In addition to the matter fields, the SM contains gauge fields which are mediator for the interactions between all the fermions. For each gauge group, we have the corresponding spin-1 particles associated to each generator of the group, *i.e.* eight gluons G_μ^a associated to the $SU(3)_c$ group, three weak boson W_μ^i associated to the $SU(2)_L$ group, and one boson B_μ associated to the $U(1)_Y$ group. The Lagrangian for the kinetic term of the gauge fields is given

f	L	e_R	Q_L	u_R	d_R
Y	-1	-2	$\frac{1}{3}$	$\frac{4}{3}$	$-\frac{2}{3}$

Table 1.1: The $U(1)_Y$ hypercharge for each fermion type is shown.

by

$$\mathcal{L}^{\text{gauge}} = -\frac{1}{4}B^{\mu\nu}B_{\mu\nu} - \frac{1}{4}G^{\mu\nu}{}_a G_{\mu\nu}{}^a - \frac{1}{4}W^{\mu\nu}{}_i W_{\mu\nu}{}^i, \tag{1.7}$$

where the field strength are defined as

$$B_{\mu\nu} = \partial_\mu B_\nu - \partial_\nu B_\mu \tag{1.8}$$
$$W^i_{\mu\nu} = \partial_\mu W^i_\nu - \partial_\nu W^i_\mu + g_2 \epsilon_{ijk} W^j_\mu W^j_\nu \tag{1.9}$$
$$G^a_{\mu\nu} = \partial_\mu G^a_\nu - \partial_\nu G^a_\mu + g_3 f_{abc} G^b_\mu G^c_\nu \,, \tag{1.10}$$

where $g_2(g_3)$ are the coupling constants of the $SU(2)_L(SU(3)_c)$ group, $\epsilon_{ijk}(f_{abc})$ are the structure constants of the $SU(2)_L(SU(3)_c)$ group, *i.e.*

$$[\sigma^i, \sigma^j] = \epsilon_{ijk}\sigma^k \tag{1.11}$$
$$[\lambda^a, \lambda^b] = f_{abc}\lambda^c \,, \tag{1.12}$$

where $\sigma^i (i = 1, 2, 3)$ are the three generators of the $SU(2)_L$ group, and $\lambda^a (a = 1, 2, \cdots, 8)$ are the eight generators of the $SU(3)_c$ group.

The gauge interaction of fermions can be obtained by replacing the partial derivatives with the covariant derivates:

$$\partial_\mu \to D_\mu = \partial_\mu - ig_3 G^a_\mu \lambda^a - ig_2 W^i_\mu \sigma^i - iY g_1 B_\mu \,, \tag{1.13}$$

where Y is the weak hypercharge given in Table 1.1. With the covariant derivates, we could obtain

$$\mathcal{L}^{\text{fermion}} = \sum_{f=L,e_R,Q_L,u_R,d_R} \bar{f} i \not{D} f \,. \tag{1.14}$$

While the above Lagrangian describes the interactions well, it has one serious problem: all the particles should be massless! This is a consequence of gauge invariance: adding masses for the gauge bosons would break gauge invariance explicitly; similarly the Dirac mass term for fermions also breaks gauge invariance.

On the other hand, experiments show that most of particles in the SM are massive, except the gluons and photons. Instead of explicitly breaking gauge invariance, a mechanism which breaks gauge invariance only through non-zero vacuum expectation value was proposed by Brout, Englert, and Higgs (BEH). The BEH mechanism adds a scalar Φ into the SM. The scalar field is a doublet under $SU(2)_L$ and thus it participates in the EW interaction. Furthermore, it has a non-trivial potential. The new terms in the Lagrangian are given by

$$\mathcal{L}^{\text{Higgs}} =(D\Phi)^\dagger(D\Phi) - V^{\text{SM}}\,. \tag{1.15}$$

The Higgs potential V^{SM} in the SM is fixed by gauge invariance and renormalisability, and it is given by

$$V^{\text{SM}} = -\mu^2\Phi^\dagger\Phi + \lambda(\Phi^\dagger\Phi)^2. \tag{1.16}$$

With $\mu^2 > 0, \lambda > 0$, the above Higgs potential achieves its minimum value when $\Phi \neq 0$. Applying $SU(2)_L$ transformations, we can arrange the vacuum state as

$$\langle\Phi\rangle_0 = \frac{1}{\sqrt{2}}\begin{pmatrix}0\\ v\end{pmatrix}\,, \tag{1.17}$$

where v is the vacuum expectation value(VEV) and it satisfies

$$v^2 = \frac{\mu^2}{2\lambda}. \tag{1.18}$$

While the Lagrangian is invariant under $SU(2)_L \times U(1)_Y$, the above vacuum state is not. To get the physical meaning of the Lagrangian we can parametrise the field Φ around its minimum such that

$$\Phi = \frac{1}{\sqrt{2}} e^{i\chi_i \sigma^i} \begin{pmatrix} 0 \\ v + H \end{pmatrix}. \tag{1.19}$$

We obtain

$$V^{\text{SM}} = \lambda v^4 + \frac{1}{2} m_H^2 H^2 + \lambda H^3 + \frac{\lambda}{4} H^4, \tag{1.20}$$

and we have the relations $\mu^2 = m_H^2, \lambda = \frac{m_H^2}{2v^2}$. With $\langle 0| H |0\rangle = 0$, H is associated to the Higgs boson. Therefore, the Higgs boson cubic and quartic self-coupling are fully fixed by the Higgs boson mass m_H and vacuum expectation value v. We could applying a new $SU(2)_L$ gauge transformation to eliminate χ^i terms, and get

$$\Phi = \frac{1}{\sqrt{2}} \begin{pmatrix} 0 \\ v + H \end{pmatrix}. \tag{1.21}$$

This particular choice is known as the unitary gauge. In this case the Goldstone bosons χ^i are combined with the weak gauge bosons to form massive gauge bosons. In particular, we can define the following combination of the gauge fields:

$$W_\mu^\pm = \frac{1}{2}(W_\mu^1 \mp i W_\mu^2) \tag{1.22}$$

$$A_\mu = \cos\theta_W B_\mu + \sin\theta_W W_\mu^3 \tag{1.23}$$

$$Z_\mu = -\sin\theta_W B_\mu + \cos\theta_W W_\mu^3, \tag{1.24}$$

where θ_W is the mixing angle determined by the coupling strength: $\sin\theta_W = \sqrt{g_1^2/(g_1^2 + g_2^2)}$. The fields $W_\mu^\pm, Z_\mu$ acquire their masses through their interactions with the Higgs fields, while A_μ remains massless. In fact, now the

Lagrangian in Eq. (1.15) becomes

$$
\begin{aligned}
\mathcal{L}_{Higgs} =& \frac{1}{2}(\partial_\mu H)^2 - V^{\text{SM}} && (1.25)\\
&+ \frac{v^2}{8}(2g_2^2 W_\mu^+ W^{-,\mu} + (g_2^2 + g_1^2)Z_\mu^2) && (1.26)\\
&+ \frac{v}{4}H(2g_2^2 W_\mu^+ W^{-,\mu} + (g_2^2 + g_1^2)Z_\mu^2) && (1.27)\\
&+ \frac{1}{8}H^2(2g_2^2 W_\mu^+ W^{-,\mu} + (g_2^2 + g_1^2)Z_\mu^2) && (1.28)
\end{aligned}
$$

where from the second line we can deduce the masses of $W^\pm, Z$ as

$$
\begin{aligned}
m_W =& \frac{1}{2}g_2 v && (1.29)\\
m_Z =& \frac{1}{2}\sqrt{g_1^2 + g_2^2}v. && (1.30)
\end{aligned}
$$

Finally, the Dirac mass term of the fermions can be obtained through their interaction with the Higgs field

$$
\mathcal{L}^{\text{Yukawa}} = - \bar{Q}_L Y_u \tilde{\Phi} u_R - \bar{Q}_L Y_d \Phi d_R - \bar{\ell} Y_e \Phi e_R + h.c.\,, \qquad (1.31)
$$

where $\tilde{\Phi}$ is the charge conjugate of the Φ field and it is given by $\tilde{\Phi} = i\sigma^2\Phi$. Y_u, Y_d, Y_L are the Yukawa parameters of the up-type quarks, down-type quarks, and charged leptons.

Adding only one scalar doublet as in Eq. (1.15) and adopting the potential in Eq. (1.20) is the minimal requirement to trigger spontaneous symmetry breaking. In fact, more scalar fields can be added, or other representations such as triplet instead of doublet can be adopted. For example, in the SM+singlet model, a new scalar singlet is added in addition to the scalar doublet, and the Higgs potential is given by [1]

$$
\begin{aligned}
V^{\text{Singlet}} =& \lambda(\Phi^\dagger\Phi - \frac{v^2}{2})^2 + \frac{a_1}{2}(\Phi^\dagger\Phi - \frac{v^2}{2})S + \frac{a_2}{2}(\Phi^\dagger\Phi - \frac{v^2}{2})S^2 && (1.32)\\
&+ \frac{1}{4}(2b_2 + a_2 v^2)S^2 + \frac{b_3}{3}S^3 + \frac{b_4}{4}S^4. && (1.33)
\end{aligned}
$$

After EWSB, it becomes

$$\begin{aligned} V^{\text{Singlet}} \supset& \lambda^{111} H^3 + \cdots & (1.34) \\ \lambda^{111} =& 6s^3 b_3 + \frac{3a_1}{2} s c^2 + 18 a_2 s^2 c v + 6c^3 \lambda v \,, & (1.35) \end{aligned}$$

where $s = \sin\theta, c = \cos\theta$, and θ is the mixing angle between H and S. Clearly, in such model we have more scalar bosons, and the couplings between them are different from the SM.

Since the discovery of the Higgs boson, the BEH mechanism gets finally confirmed. However, the dynamical origin of the Higgs potential is still unknown. Meanwhile, the Higgs sector is connected to several problems of the SM. One is the naturalness problem: there are large mass hierarchy between the fermion generations:

$$m_e \ll m_\mu \ll m_\tau ; m_u \ll m_c \ll m_t ; m_d \ll m_s \ll m_b . \tag{1.36}$$

In the SM the only mass scale is the VEV, and all fermions acquire masses through the Yukawa coupling with the Higgs field. However, the top quark is the only SM particles with a Yukawa coupling of order one; the Yukawa coupling of all other fermions are much smaller than one. In that sense, the tiny Yukawa couplings seem “unnatural”.

The Higgs boson also acquires mass from the VEV. However, the mass of the Higgs boson is not protected by any symmetry, and it receives quadratically divergent corrections through quantum corrections. As a result, the radiative corrections to the Higgs mass are proportional to the square of the masses of other particles, and could be much large than the Higgs mass. In order to retain a small mass (125GeV), fine-tuning is required to balance the radiative corrections. This problem is called the hierarchy problem and it motivates many theorists to introduce new physics beyond the SM.

The discovery of the Higgs boson brings particle physics into a new era. Examining the properties of the Higgs boson is essential to searching for NP. One important question is on the exact form of the Higgs potential, as various NP modifies the Higgs potential. Measuring the Higgs self-couplings is among the main task of current and future colliders.

In this thesis, I will focus on measuring the Higgs self-couplings at current and future colliders, considering both direct measurements and indirect constraints.

Chapter 2 describes the effective field theory framework, which parametrises the derivations from the SM. Renormalisation of the relevant operators are carried out, to allow the study of indirect probes of the Higgs self-couplings.

Chapter 3 focuses on hadron colliders. Firstly, I will briefly review the status of measuring the cubic Higgs self-coupling directly. After that, I will discuss the indirect constraints of the cubic Higgs self-coupling. Then I will move to the quartic Higgs self-coupling, considering direct measurements at a future 100 TeV hadron collider. Finally, I will discuss indirect constraints of the quartic Higgs self-coupling.

Chapter 4 focuses on future e^+e^- colliders. I will describe the calculation of single-, double-, and triple-Higgs processes at e^+e^- collider, including one-loop corrections when appropriately. Then I will consider various proposals of future e^+e^- colliders, and compare their reach on both Higgs cubic and quartic self-couplings, including both direct measurements and indirect constraints.

Chapter 5 considers the recent proposal of a high energy $\mu^+\mu^-$ collider. I will describe the effects of Higgs boson self-couplings on multi-Higgs processes at such high energy machine, and then discuss the constraints at various collider energy.

This work is based on the following publications:

- A. Costantini, F. De Lillo, F. Maltoni, L. Mantani, O. Mattelaer, R. Ruiz and X. Zhao, “Vector boson fusion at multi-TeV muon colliders,” [arXiv:2005.10289 [hep-ph]].
- M. Chiesa, F. Maltoni, L. Mantani, B. Mele, F. Piccinini and X. Zhao, Measuring the quartic Higgs self-coupling at a multi-TeV muon collider, [arXiv:2003.13628 [hep-ph]].
- S. Borowka, C. Duhr, F. Maltoni, D. Pagani, A. Shivaji, and X. Zhao, Probing the scalar potential via double Higgs boson production at hadron colliders, JHEP **1904** (2019) 016

- F. Maltoni, D. Pagani and X. Zhao, Constraining the Higgs self-couplings at e^+e^- colliders, JHEP **1807** (2018), 087
- F. Maltoni, D. Pagani, A. Shivaji and X. Zhao, Trilinear Higgs coupling determination via single-Higgs differential measurements at the LHC, Eur. Phys. J. C**77** (2017) no. 12, 887
- W. Kilian, S. Sun, Q.S. Yan, X. Zhao and Z. Zhao, New Physics in multi-Higgs boson final states, JHEP **1706** (2017), 145

During my PhD, I have published other works of research not presented in this manuscript:

- W. Kilian, S. Sun, Q.S. Yan, X. Zhao and Z. Zhao, Multi-Higgs Production and Unitarity in Vector-Boson Fusion at Future Hadron Colliders, Phys. Rev. D**101** (2020) no. 7, 076012
- F. Maltoni, M.K. Mandal and X. Zhao, Top-quark effects in diphoton production through gluon fusion at next-to-leading order in QCD, Phys. Rev. D**100** (2019) no. 7, 071501
- M.K. Mandal and X. Zhao, Evaluating multi-loop Feynman integrals numerically through differential equations, JHEP **1903**(2019), 190
- Z. Liu and X. Zhao, Bootstrapping solutions of scattering equations, JHEP **1902** (2019), 071
- G. Li, Z. Li, Y. Liu, Y. Wang and X. Zhao, Probing the Higgs boson-gluon coupling via the jet energy profile at e^+e^- colliders, Phys. Rev. D**98** (2018) no. 7, 076010
- Y. Gong, Z. Li, X. Xu, L.L. Yang and X. Zhao, Mixed QCD-EW corrections for Higgs boson production at e^+e^- colliders, Phys. Rev. D **95** (2017) no. 9, 093003

2 The SMEFT framework

The anomalous coupling approach has been widely used in studying the Higgs boson self-couplings. In this case, one considers the Lagrangian in the unitary gauge after EWSB, and modifies the Higgs boson self-couplings directly, *i.e.*,

$$\mathcal{L} \supset \lambda_3 v H^3 + \frac{\lambda_4}{4} H^4 \,. \tag{2.1}$$

While providing a very simple way of modifying the Higgs boson self-couplings, it features several limitations. One problem is that it only works in the unitary gauge. This brings difficulties when calculating loop corrections as Feynman gauge is widely adopted for these computations. In the Feynman gauge, unphysical pseudo-Goldstone bosons appear together with the Higgs boson, couple with it, and making it unclear, *in general*, whether the couplings among them are modified in such an approach.

Instead of the anomalous coupling approach, we consider the EFT approach. Since new particles beyond the SM have not been found yet, it is legitimate to assume that new physics scale is larger than the EW scale. At and right above the EW scale, such new physics can be described by a low-energy linear EFT called SMEFT, by adding higher dimensional operators into the SM. We consider the case that the Higgs potential is modified by adding a tower of higher-dimensional operators:

$$V^{\mathrm{NP}} = V^{\mathrm{SM}} + \sum_{n=3}^{\infty} \frac{c_{2n}}{\Lambda^{2n-4}} (\Phi^\dagger \Phi - \frac{1}{2} v^2)^n \tag{2.2}$$

Note that we put the extra $-\frac{1}{2}v^2$ terms in the bracket, instead of the "standard" notation as below

$$V^{\mathrm{NP}}_{\mathrm{std}} = V^{\mathrm{SM}} + \sum_{n=3}^{\infty} \frac{c'_{2n}}{\Lambda^{2n-4}} (\Phi^\dagger \Phi)^n \,. \tag{2.3}$$

The advantage of our convention is that c_{2n} only modify m-Higgs vertex when $m \geq n$, so that the connection between Higgs boson self-couplings and Wilson coefficients are simple and clear. We'd like to note that both convention are fully equivalent, at any order of Λ. On the other hand, the appearance of $-\frac{1}{2}v^2$ term requires special care when considering loop corrections, which we will discuss later.

We note that the above new physics operators only modify the Higgs boson self-couplings, without any other effect at the tree level.

After EWSB, we obtain

$$V^{NP} = \frac{1}{2}m_H^2 H^2 + \lambda_3 v H^3 + \frac{\lambda_4}{4} H^4 + \frac{\lambda_5}{v} H^5 + \cdots \tag{2.4}$$

the new physics operators modify the Higgs boson self-couplings. In detail, we have

$$\lambda_3 = \lambda + \frac{c_6 v^2}{\Lambda^2} \tag{2.5}$$

$$\lambda_4 = \lambda + \frac{6 c_6 v^2}{\Lambda^2} + \frac{4 c_8 v^4}{\Lambda^4} \tag{2.6}$$

$$\lambda_5 = \frac{3}{4}\frac{c_6 v^2}{\Lambda^2} + \frac{2 c_8 v^4}{\Lambda^4} + \frac{c_{10} v^6}{\Lambda^6} \tag{2.7}$$

$$\cdots = \cdots \,. \tag{2.8}$$

We note that in the SM $\lambda_3^{\mathrm{SM}} = \lambda_4^{\mathrm{SM}} = \lambda = \frac{m_H^2}{2v^2}$, and $\lambda_i = 0$ for $i \geq 5$. Therefore, the ratio of the Higgs cubic(quartic) self-couplings to the SM is given by:

$$\kappa_3 =\frac{\lambda_3}{\lambda_3^{\text{SM}}} = 1+\frac{c_6 v^2}{\lambda\Lambda^2} = 1+\bar{c}_6 \tag{2.9}$$

$$\kappa_4 =\frac{\lambda_4}{\lambda_4^{\text{SM}}} = 1+6\frac{c_6 v^2}{\lambda\Lambda^2}+4\frac{c_8 v^4}{\lambda\Lambda^4} = 1+6\bar{c}_6+\bar{c}_8\,. \tag{2.10}$$

The above EFT Higgs potential provides a convenient way of defining the derivation of Higgs boson self-couplings to the SM, while preserving gauge invariance. Working under R_ξ gauge, the Higgs doublet is given by

$$\Phi = \frac{1}{\sqrt{2}}\begin{pmatrix} G^+ \\ v+H+iG^0 \end{pmatrix}\,. \tag{2.11}$$

To renormalise it, the Higgs boson field and vacuum expectation value should be separated into renormalised quantity and counter terms, *i.e.* $H \to Z_H^{1/2}H, v \to v+\delta v$,

$$\Phi = \frac{1}{\sqrt{2}}\begin{pmatrix} G^+ \\ v+\delta v+Z_H^{\frac{1}{2}}H+iG^0 \end{pmatrix}\,. \tag{2.12}$$

On the other hand, the v entering in the new physics operators $(\Phi^\dagger\Phi-\frac{1}{2}v^2)$ is just a free mass scale, which we choose to be equal to the renormalised vacuum expectation value. As a result, we have

$$\left(\Phi^\dagger\Phi-\frac{1}{2}v^2\right)^n = \frac{1}{2}\left[(Z_H H^2+2vHZ_H^{\frac{1}{2}}(1+\frac{\delta v}{v})+\mathcal{R}\right]^n \tag{2.13}$$

where $\mathcal{R} = 2v\delta v$ stemming from the fact that the v enters in the l.h.s is not renormalised.

2.1 One-loop renormalisation in double Higgs production in EFT

In this section we provide all the ingredients that are necessary for one-loop renormalisation in double Higgs production with arbitrary c_6 and c_8 values. First of all, it is important to note that the only quantities that are renormalised and receive a contribution from c_6, c_8 and c_{10} are

$$Z_H\,, \quad m_H\,, \quad T\,, \quad c_6\,, \tag{2.14}$$

where Z_H is the Higgs wave function and T is the tadpole contribution, which we cancel via the δt counterterm so that the physical value of v does not get shifted. All the other quantities do not receive additional one-loop contributions on top of the SM ones, including δv, which is completely of SM origin.

Thus, for our calculation the necessary ingredients for the renormalisation of the virtual corrections are:

$$\delta Z_H = \delta Z_H^{\rm SM} + \delta Z_H^{\rm NP}\,, \tag{2.15}$$

$$\delta m_H^2 = (\delta m_H^2)^{\rm SM} + \delta(m_H^2)^{\rm NP} - 6\frac{c_6}{\Lambda^2}v^3\delta v\,, \tag{2.16}$$

$$\delta t = \delta t^{\rm SM} + \delta t^{\rm NP}\,, \tag{2.17}$$

$$\delta c_6 = \delta c_6^{\rm NP}\,. \tag{2.18}$$

All the quantities with “SM” as apex are the SM contributions and can be found in [2], those with “NP”, which indeed stands for new physics, are the new contributions from c_6, c_8 and c_{10}. Besides c_6, which is renormalised in the $\overline{\rm MS}$ scheme, all the other EW input parameters are assumed to be renormalised on-shell, with exception of fine structure α, which we renormalise in the G_μ-scheme. This is relevant for our calculation since in the SM the renormalisation of v is related to the charge renormalisation, δZ_e,

$$\frac{\delta v}{v} = \frac{\delta s_W}{s_W} - \delta Z_e + \frac{\delta m_W^2}{2m_W^2}\,, \tag{2.19}$$

where $s_W = \sin\theta_W = \sqrt{1-\frac{m_W^2}{m_Z^2}}$, and $\delta s_W/s_W$ is given in Ref. [2].

The appearance of the extra quantity $-6\frac{c_6}{\Lambda^2}v^3\delta v$ in eq. (2.16) is due to the presence of v in the parametrisation of eq. (2.2), which as we said has an impact on the renormalisation procedure. Before giving the explicit formulas for $\delta Z_H^{\rm NP}, \delta(m_H^2)^{\rm NP}, \delta t^{\rm NP}$ and the counterterms for the H^3 vertex and H propagator, we briefly discuss this technical aspect.

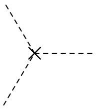

$$= \delta\lambda_{H^3} \tag{2.23}$$

Figure 2.1: The counter term for the triple Higgs vertex.

The explicit term v used in the parametrisation of eq. (2.2) is a subtle quantity. In a tree-level analysis it can be trivially identified with the location of the minimum of $V(\Phi)$, which defines the ground state $|0\rangle$ of the Higgs field

$$|\langle 0|\,\Phi\,|0\rangle|^2 = \frac{v^2}{2}\,. \tag{2.20}$$

However, strictly speaking, the v appearing in eq. (2.2) is, like Λ, just a mass parameter that we chose for mapping c'_{2n} into c_{2n}. In principle we could have chosen a generic mass $M \neq v$, but we would have not got any advantage. On the contrary, with $M = v$, SM relations such as

$$\delta\lambda = \frac{\delta m_H^2}{2v^2} - \frac{m_H^2\,\delta v}{v^3} + \frac{\delta t}{2v^3}\,, \tag{2.21}$$

$$\delta v = \delta v^{\rm SM} \;\leftrightarrow\; \delta v^{\rm NP} = 0\,, \tag{2.22}$$

are preserved (see ref. [3]); they would be different using eq. (2.3). The crucial point is that at one loop, or even at higher orders, $|\langle 0|\,\Phi\,|0\rangle|$ is involved in the renormalisation, while the term v in eq. (2.2) is not; as said it is just a mass parameter tuned to v for our purpose. For this reason, relations among the different renormalisation constant of the SM parameters are unaltered, but in the case of m_H and H^n vertexes the definitions of the renormalisation counterterms contain additional terms.

This mechanism is at the origin of the aforementioned term in eq. (2.16) as well as to some additional terms (second line of eq. (2.24)) that appear in the counterterm for the H^3 vertex in Fig. 2.1, where $\delta\lambda_{H^3}$ reads

$$
\begin{aligned}
\delta\lambda_{H^3} \quad = \quad & -i6\Big[\frac{c_6 v^3}{\Lambda^2}\left(\frac{\delta c_6}{c_6}+\frac{3}{2}\delta Z_H+3\frac{\delta v}{v}\right)+\lambda v\left(\frac{\delta\lambda}{\lambda}+\frac{3}{2}\delta Z_H+\frac{\delta v}{v}\right)\Big] \\
& -i6\Big[\frac{4c_8 v^4\delta v}{\Lambda^4}+3\frac{c_6}{\Lambda^2}v^2\delta v\Big]\,. \qquad (2.24)
\end{aligned}
$$

Similarly, the Feynman rule for the counterterm of the Higgs propagator (see eq. (A.4) in ref. [2]) is modified into

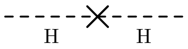

$$
= \; -i\left(\delta m_H^2+m_H^2\delta Z_H-\delta Z_H k^2+6\frac{c_6}{\Lambda^2}v^3\delta v\right)\,, \qquad (2.25)
$$

and therefore the additional term entering in eq. (2.16) is exactly canceled.

The only missing information are the NP contributions to the counterterms in eqs. (2.15)-(2.17), which we thus provide in the following:

$$
\delta t^{\mathrm{NP}} = -\frac{1}{16\pi^2}\frac{3c_6}{\Lambda^2}v^3 A_0(m_H^2)\,, \qquad (2.26)
$$

$$
\delta Z_H^{\mathrm{NP}} \quad = \quad \left(\frac{2c_6 v^2}{\lambda\Lambda^2}+\frac{c_6^2 v^4}{\lambda^2\Lambda^4}\right)\delta Z_H^{\mathrm{SM},\lambda}\,, \qquad (2.27)
$$

$$
\begin{aligned}
\delta(m_H^2)^{\mathrm{NP}} = & \frac{1}{16\pi^2}\Big[\frac{c_6}{\Lambda^2}v^2\left(18A_0(m_H^2)+3A_0(\xi_Z m_Z^2)+6A_0(\xi_W m_W^2)\right. \qquad (2.28) \\
& \left.+18m_H^2 B_0(m_H^2,m_H^2,m_H^2)\right)+ \\
& +\frac{v^4}{\Lambda^4}\left(12c_8 A_0(m_H^2)+c_6^2 18v^2 B_0(m_H^2,m_H^2,m_H^2)\right)\Big]\,, \qquad (2.29)
\end{aligned}
$$

$$
\begin{aligned}
\delta c_6 \quad = \quad & \frac{\Delta}{16\pi^2}\Bigg[c_6\left(54\lambda-9\frac{m_Z^2+2m_W^2}{v^2}+6\frac{N_c m_t^2}{v^2}\right) \\
+ \quad & \frac{c_8 v^2}{\Lambda^2}\left(64\lambda-6\frac{m_Z^2+2m_W^2}{v^2}+4\frac{N_c m_t^2}{v^2}\right)+\frac{45c_6^2 v^2}{\Lambda^2} \\
+ \quad & \frac{20c_{10}\lambda v^4}{\Lambda^4}+\frac{36c_6 c_8 v^4}{\Lambda^4}\Bigg]\,, \qquad (2.30)
\end{aligned}
$$

where

$$\delta Z_H^{\mathrm{SM},\lambda} \quad = \quad -\frac{9\lambda m_H^2}{16\pi^2} B_0'(m_H^2, m_H^2, m_H^2)\,, \tag{2.31}$$

is the contribution from the trilinear Higgs self-coupling to δZ_H in the SM and A_0 and B_0 are the standard scalar loop integrals and Δ is the UV divergence $\Delta \equiv 1/\epsilon - \gamma + \log(4\pi)$ in $D = 4 - 2\epsilon$ dimensions. As discussed in sec. 4.1.2 terms up to the order $(v/\Lambda)^6$ have to be in general considered. However, note that no terms beyond $(v/\Lambda)^2$ are present in δt, or beyond $(v/\Lambda)^4$ in δZ_H and δm_H^2, while c_6 is appearing at order $(v/\Lambda)^2$, so terms up to $(v/\Lambda)^6$ are in fact present in δc_6.

We want to stress that all these contributions have to be taken into account in order to obtain gauge invariance for the final finite result of double-Higgs production at one loop. We kept the explicit dependence on the ξ parameter for a generic R_ξ-gauge in order to verify that renormalised amplitudes do not depend on ξ. With this calculation setup, results are equivalent to those of a standard calculations based on the parameterisation of eq. (2.3) and c'_{2n} coefficients renormalised in the $\overline{\mathrm{MS}}$ scheme.

3 The Higgs boson self-couplings at hadron colliders

Multi-Higgs boson processes feature Higgs boson self-couplings at tree-level, and thus provide a way of directly measuring Higgs boson self-couplings. In particular, to measure the Higgs boson cubic self-coupling we need to consider double Higgs production, and to measure the Higgs boson quartic self-coupling we need to consider triple Higgs production.

Similar to single Higgs production, at hadron colliders there are several dominant production mechanisms for double and triple Higgs production. In Fig. 3.1 we show the cross section for Higgs boson pair production at pp collider. We can see that among them the dominant production channel is through gluon fusion, mediated by a heavy quark loop. The LO correction of $gg \to HH$ in the SM was calculated in Ref. [5] and Ref. [6], and full NLO QCD corrections was calculated in Ref. [7–9]. The NLO matched with shower effects [10–12], and the NNLO in the large top-mass limit [13–16] and improved with the full NLO [17] have been calculated. While many phenomenological studies have been performed [18–37], only an upper bound on cross section of $gg \to HH$ is set experimentally, and only a weak bound $\kappa_3 \in (-5.0, 12.0)$ [38] have been obtained till now. Other production modes, including vector boson fusion, vector boson associated production, and top pair associated production, are found to be complementary to gluon fusion [39–44]. While it is unclear on the final precision on κ_3 at the LHC with high-luminosity runs, it is commonly believable that at a 100 TeV future collider percent precision can be achieved [4, 45].

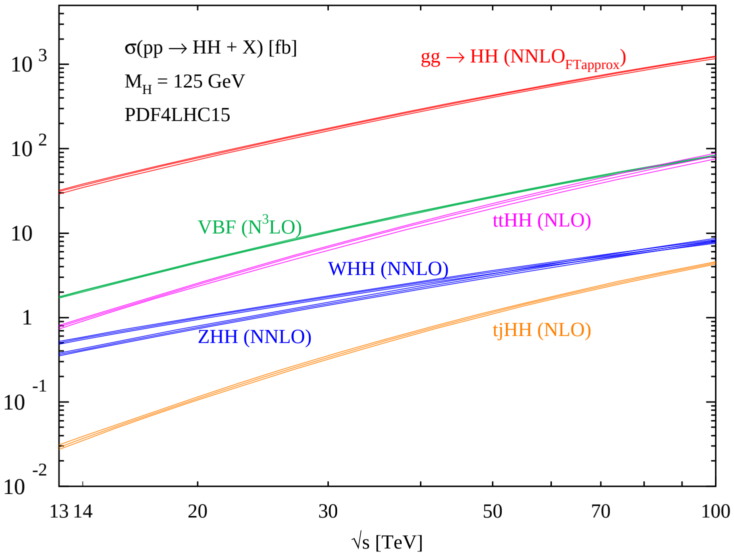

Figure 3.1: The cross section for Higgs boson pair production at pp collider is shown. Figure from Ref. [4].

On the other hand, the prospects of quartic Higgs boson self-coupling are very uncertain. Due to tiny cross section of $gg \to HHH$, at the LHC it is extremely challenging [46,47]. Even at future 100TeV pp collider, a considerable amount of integrated luminosity is required to obtain rather loose bounds [45,48–50]. Also precise predictions in the SM are available [51–53].

In the following sections, we begin with alternative approach of constraining the cubic Higgs boson self-coupling through loop corrections to single Higgs processes, then consider the feasibility of directly constraining the Higgs boson quartic self-couplings through triple Higgs boson production at future hadron colliders, and indirect constraints through loop corrections to double Higgs boson production.

3.1 Single Higgs and κ_3

Besides direct measurement, indirect measurements provide competitive and complementary constraints. In Ref. [54], an indirect method of measuring κ_3 via EW radiative corrections to $e^+e^- \to ZH$ process was proposed. The same idea has been extended to the LHC [55–58], by studying the κ_3-dependent EW corrections in single Higgs production and decay. The limits on κ_3 are found to be comparable to the one obtained from directly measuring κ_3 in double Higgs production. Moreover, constrains on κ_3 through two-loop effects in EW precision observables are also been studied [59, 60].

Going beyond inclusive cross section, we present an automated public code which can generate events including κ_3 effects at one loop, allowing the study of differential effects in VBF, VH and $t\bar{t}H$ production and all the relevant Higgs decays. Using the code, we extend the previous studies to the differential level, including all relevant single Higgs production and decay channels. Moreover, we repeat the calculation of NLO EW corrections, to check the robustness of the strategy.

3.1.1 The calculation framework

For single Higgs processes, the effects of κ_3 starts at one-loop level (two-loop if the LO is loop-induced, such as $gg \to H$ and $H \to \gamma\gamma$). In detail, the κ_3-dependent part of NLO corrections to the single Higgs processes can be divided into two categories: the first is the kinematic- and process-dependent part, which is linear in λ_3; the second is universal and proportional to λ_3^2, which arises from the wave-function renormalisation.

We have

$$\sigma^{\text{NLO}} = Z_H^{\text{BSM}} \sigma^{\text{LO}} (1 + C_1 \kappa_3 + \delta Z_H^{\text{SM},\lambda} + \delta_{\text{EW}}|_{\kappa_3=0}), \tag{3.1}$$

where $\delta Z_H^{\text{SM},\lambda}$ is the SM contribution of the cubic Higgs boson self-coupling to the Higgs boson wave function renormalisation, and it is given by

$$\begin{aligned} \delta Z_H^{\text{SM},\lambda} &= -\frac{9\lambda m_H^2}{16\pi^2} B_0'(m_H^2, m_H^2, m_H^2) \\ &= -\frac{9}{16\sqrt{2}\pi^2}\left(\frac{2\pi}{3\sqrt{3}} - 1\right) G_\mu m_H^2 \\ &\approx -1.536 \times 10^{-3}, \end{aligned} \tag{3.2}$$

where Z_H^{BSM} describes the BSM contribution of cubic Higgs boson self-coupling to the Higgs wave function renormalisation. We choose to resum this contribution, which is given by

$$Z_H^{BSM} = \frac{1}{1-(\kappa_3^2-1)\delta Z_H}\,, \tag{3.3}$$

where $\delta_{\mathrm{EW}}|_{\kappa_3=0}$ denotes the part of SM NLO EW corrections which does not depend on the Higgs boson self-coupling. Define the NLO EW K-factor in the SM:

$$K_{\mathrm{EW}} = \frac{\sigma^{\mathrm{SM}}_{\mathrm{NLO}}}{\sigma_{\mathrm{LO}}}\,, \tag{3.4}$$

we have

$$\delta_{\mathrm{EW}}|_{\kappa_3=0} = K_{\mathrm{EW}} - 1 - C_1 - \delta Z_H^{\mathrm{SM},\lambda}\,, \tag{3.5}$$

where C_1 is the kinematic- and process-dependent part contribution of the Higgs boson cubic self-coupling, while $\delta Z_H^{\mathrm{SM},\lambda}$ is a universal quantity. To compute C_1 at the differential level, we employed two independent methods. In the first one, we parametrise the finite one-loop corrections to the cubic Higgs self-coupling as form factors which are functions of the external momenta. Those form factors are implemented as effective vertex in a dedicated UFO model files [61] which is used in MadGraph5_aMC@NLO [62]. The code is then linked to the LoopTools package [63] for the computation of one-loop integrals. As a result, parton level events can be generated including $\mathcal{O}(\kappa_3)$ effects, and any further processing and analysis such as parton showering and detector simulation can be performed straightforwardly. Currently we have implemented the HVV form factor(see Appendix A for the formula), which allows the computation of processes where the Higgs boson only couples to vector boson at tree-level, *i.e.* VBF, VH, and $H \to 4\ell$ processes.

On the other hand, the implementation of form factors for $t\bar{t}H$ and tHj would be quite complicated, as they will include four-point form factors and even five-point form factors. Instead, we employ a different strategy which is based on reweighting. In the second method, one starts by generating LO parton-level events. These events are then used as input for a code that computes the new weights based the matrix elements:

$$w_i = \frac{2\mathrm{Re}(\mathcal{M}^{0*}\mathcal{M}^{1}_{\kappa_3^{\mathrm{SM}}})}{|\mathcal{M}^0|^2}\,, \tag{3.6}$$

where $\mathcal{M}^0$ refers to the tree-level amplitude and $\mathcal{M}^{1}_{\kappa_3^{\mathrm{SM}}}$ is the SM virtual corrections depending on κ_3, excluding the Higgs boson wave-function contribution. The LO events are reweighted by multiplying the weight of each event i by the new weight w_i. The resulting weighted events are corresponding to the differential C_1.

We use MadGraph5_aMC@NLO to evaluate the required one-loop matrix elements. For each process, we use diagram filters to select the relevant one-loop matrix elements featuring the Higgs cubic self-coupling. For VBF and VH, we compared the results obtained in both methods and found excellent agreement.

We adopt the following input parameters:

$$G_\mu = 1.1663787 \times 10^{-5}\ \mathrm{GeV}^{-2},\ m_W = 80.385\ \mathrm{GeV}, \tag{3.7}$$

$$m_Z = 91.1876\ \mathrm{GeV}, m_H = 125\,\mathrm{GeV}, m_t = 172.5\,\mathrm{GeV}\,. \tag{3.8}$$

We use PDF4LHC2015 sets for the parton distribution function with the factorisation scale and renormalisation scale are set to be $\mu_F = \mu_R = \frac{1}{2}\sum_i m(i)$, where $m(i)$ are the masses of particles i in the final state. We note that different choices of factorisation and renormalisation scale will affect the differential distribution of the LO cross section and the $\mathcal{O}(\lambda)$ corrections, which represents uncertainties due to QCD corrections. On the other hand, at the differential level the effects of different choices of scales factorise out in C_1, and thus they only change the weight of different phasespace region. In the following we provide the differential distribution for various relevant observables in VBF, VH, $t\bar{t}H$, and tHj production channels and in the $H \to 4\ell$ decay channel.

For the VBF channel, we require the EW production of Higgs plus two jets, which also include VH configuration where the vector boson V decays into two jets. To eliminate VH contribution, we apply the following kinematic

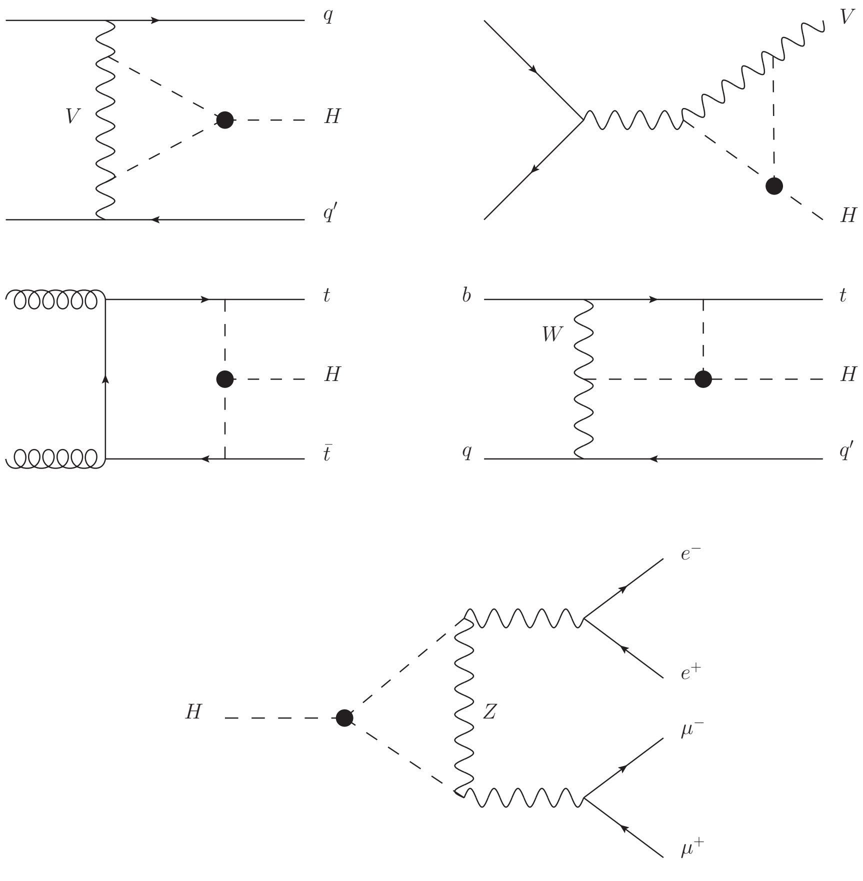

Figure 3.2: Representative Feynman diagrams of one-loop corrections to single Higgs production and decay which involves Higgs cubic self-couplings.

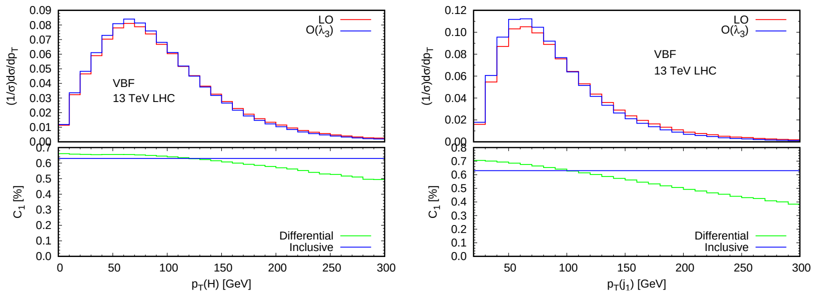

Figure 3.3: Effects of $\mathcal{O}(\kappa_3)$ corrections in VBF at 13 TeV LHC are shown for $p_T(H)$ and $p_T(j_1)$.

cuts [64] on the two final-state jets:

$$p_t^j \geq 20\,\text{GeV}, |\eta_j| < 5, |\eta_{j_1} - \eta_{j_2}| > 3, m(jj) \geq 130\,\text{GeV}\,. \qquad (3.9)$$

In Fig. 3.3, we show the distribution of the transverse momenta of the Higgs boson and the harder jet. We can see that C_1 is almost flat on those distributions. In fact, we have checked that similar effects are observed in other observables. As already noticed in Refs. [56, 57], the value of C_1 is not particular large. Here we found that $C_1 = 0.63\%$ at the inclusive level, and it never exceeds 0.70% at the differential level. Comparing to the cases of VH and $t\bar{t}H$, for this channel the Higgs boson is coupled to internal V propagators only. As a result, no Sommerfeld enhancement is present at threshold. Therefore, the interest of VBF on indirect determination of κ_3 is mainly limited to the shift of the total rate. Even such shift is modest, it is still relevant, since VBF is the channel with the second largest cross section and smallest of the theory uncertainties [64].

In Fig. 3.4, we show the $p_T(H)$ and $m(HV)$ distribution for ZH and WH production. As discussed in Refs. [56, 57], this channel receives Sommerfeld enhancement due to the non-relativistic regime, when the final states are just above the threshold. As a result, the $\mathcal{O}(\kappa_3)$ correction is softer than the LO case for $p_T(H)$ and $m(VH)$ distributions. Consequently, C_1 grows at the threshold, despite the LO cross section is rather small. In detail, C_1 is 1.19 (1.03)% for $ZH(WH)$ at the inclusive level, it is around 2.3(1.8)% for

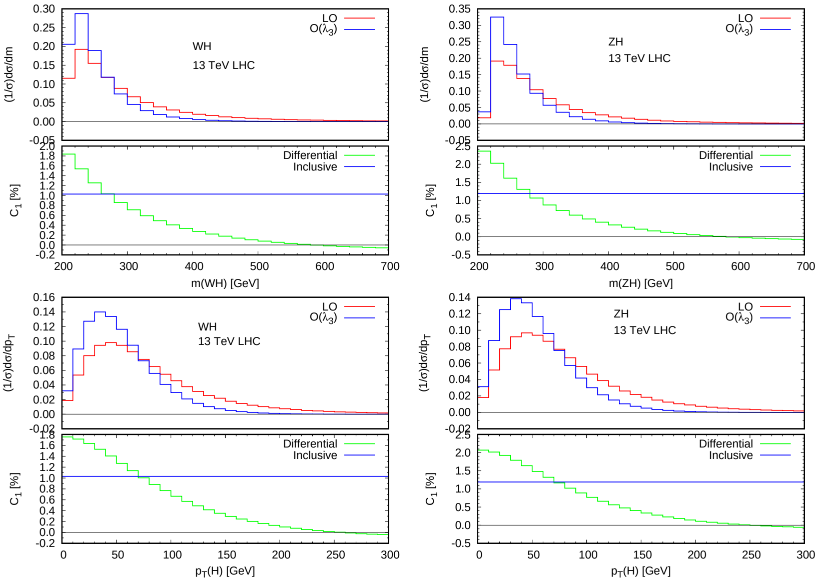

Figure 3.4: Differential C_1 for ZH and $WH(W = W^+, W^-)$ are shown for $p_T(H)$ and $m(HV)(V = W, Z)$.

$m(VH)$ at the threshold. Therefore, in order to detect anomalous κ_3 effects, dedicated measurements in the threshold region would be desirable.

In Fig. 3.5, we show the differential distribution for $t\bar{t}H$. Comparing to other processes, C_1 for $t\bar{t}H$ is the largest, and the kinematic dependence is the strongest [56]. While C_1 for inclusive cross section is 3.52%, it can increase up to $\sim 5\%$ in small p_T region. If we consider $m(t\bar{t}H)$ distribution, C_1 can reach 10% in the threshold region. The origin of such large C_1 in the threshold region is again due to Sommerfeld enhancement, and also the large top Yukawa coupling.

The tHj channel, which is characterised by a rather small cross section at the LHC, features Higgs coupling to both fermions and vector bosons, and that makes it an interesting process to determine relative phases among the Higgs couplings to fermions and bosons [65–68]. The $\mathcal{O}(\kappa_3)$ correction has not been

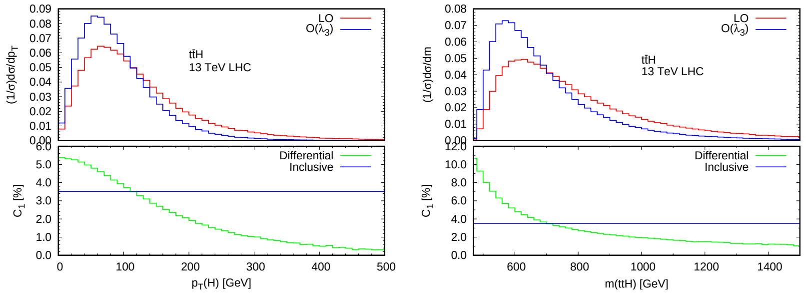

Figure 3.5: Differential C_1 for $t\bar{t}H$ are shown for $p_T(H)$ and $m(t\bar{t}H)$.

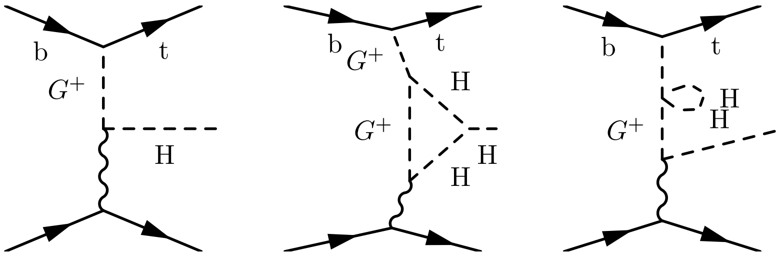

Figure 3.6: Representative Feynman diagrams involving Goldstone bosons at LO(left) and one-loop(middle and right) for single top production at hadron collider in Feynman gauge.

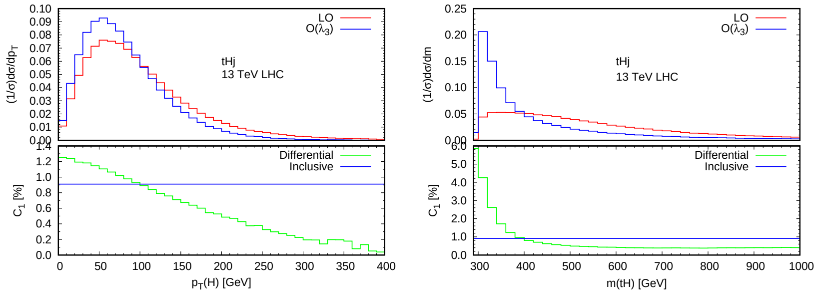

Figure 3.7: $\mathcal{O}(\kappa_3)$ corrections for tHj production are shown on $p_T(H)$ distribution and $m(tH)$ distribution.

considered in Ref. [56], and we compute it for the first time. Different from other production channel, Goldstone bosons appear in the Feynman diagrams at the LO as shown in the left of Fig. 3.6. Therefore, HGG as well as $HHGG$ interactions are present in one-loop EW corrections(see Fig. 3.6). While the former is not modified by the $(\Phi^\dagger\Phi)^n$ operators, the latter is indeed modified. The calculation can be consistently performed in two different ways: either directly employing the unitary gauge, or adopting the EFT and keeping track of the modification on couplings between Higgs boson and Goldstone bosons in $R\xi$ gauge. We adopt the second method, since the one-loop calculation in MadGraph5_aMC@NLO requires Feynman gauge. In a generic gauge, the on-shell renormalisation involves the counter terms for the Goldstone self-energy, which comes from the shift of `vev` and depends on the Higgs tadpole counter term δt, and receives contribution from the Higgs boson cubic self-coupling. If we only modify the value of κ_3, the Goldstone self-energy counter term receives a UV-divergent and gauge-dependent contribution proportioanl to $\kappa_3 - 1$, which is not cancelled by any divergence from loop diagrams. Instead, working under EFT the $HHGG$ vertex is also modified, which features a seegull in the Goldstone propagator(see the right of Fig. 3.6); such contribution cancel exactly the above UV-divergent and gauge-dependent contribution. Having understood this point, the calculation is straightforward and can be performed automatically within MadGraph5_aMC@NLO. In Fig.3.7, we show the $\mathcal{O}(\kappa_3)$ corrections for $p_T(H)$ and $m(tH)$. As expected, in $m(tH)$ distribution we can see that C_1 also receive enhancement at the threshold due to Sommerfeld effects, and it is smaller than corresponding C_1 for $t\bar{t}H$, since only one top quark in the final state is present.

Being a scalar, the Higgs boson decays to two-body decay channel in an isotrophic way; only four-body decay channel has nontrivial final state kinematics. Using the form factor code, we calculate C_1 for $H \to e^+e^-\mu^+\mu^-$ channel. We analysed C_1 for many observables, and we found that in general it has no kinematic dependence. As an example, in Fig. 3.8 we show C_1 for the invariant mass of leading and sub-leading lepton pair. Ignoring the tiny Yukawa between the Higgs boson and finalstate leptons, this result can be extended to all other decay channels where the Higgs boson is decayed into four fermions.

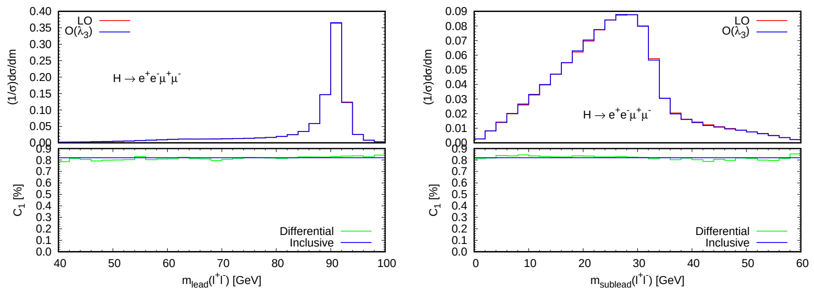

Figure 3.8: LO and $\mathcal{O}(\kappa_3)$ corrections on distribution of $m(\ell^+\ell^-)$ for the leading and subleading lepton pair are shown for $H \to 4\ell$.

Channels	ggF	VBF	ZH	WH	$t\bar{t}H$	tHj
$K_{\rm EW}$	1.049	0.932	0.947	0.93	1.014	0.95

Table 3.1: $K_{\rm EW}$ factor for NLO EW corrections of single Higgs production at 13 TeV LHC are shown.

3.1.2 SM EW corrections

The $\mathcal{O}(\kappa_3)$ contribution is gauge invariant and finite. However, in the SM, other contributions are present at the same order of accuracy. In other words, the $\mathcal{O}(\kappa_3)$ corrections should be considered as a gauge-invariant and finite subset of the complete NLO corrections, including both QCD and EW corrections. We assume that QCD corrections are factorisable, however, EW corrections may be non-factorisable. Therefore, we compute NLO EW corrections and study the impact of EW corrections. We perform the calculation via an extension of the MadGraph5_aMC@NLO framework which has already been used and validated in Refs. [69–74]. We adopt the G_μ-scheme as the renormalisation scheme, consistently with the input parameters listed before.

In table 3.1, we list the $K_{\rm EW}$ factors for single Higgs production at 13 TeV LHC. At the differential level, we show various observables for ZH, WH and $t\bar{t}H$ in fig. 3.9,3.10,3.11. In each figure, we plot the distribution of $p_T(H)$ and the invariant mass of final states. In the upper plots we show the ratio $(\sigma^{\rm BSM}_{\rm NLO} - \sigma_{\rm LO})/\sigma_{\rm LO}$, *i.e.* the size of NLO corrections including both SM NLO EW and $\mathcal{O}(\kappa_3)$ corrections. In the lower plots we show the ratio $\sigma^{\rm BSM}_{\rm NLO}/\sigma^{\rm SM}_{\rm NLO}$,

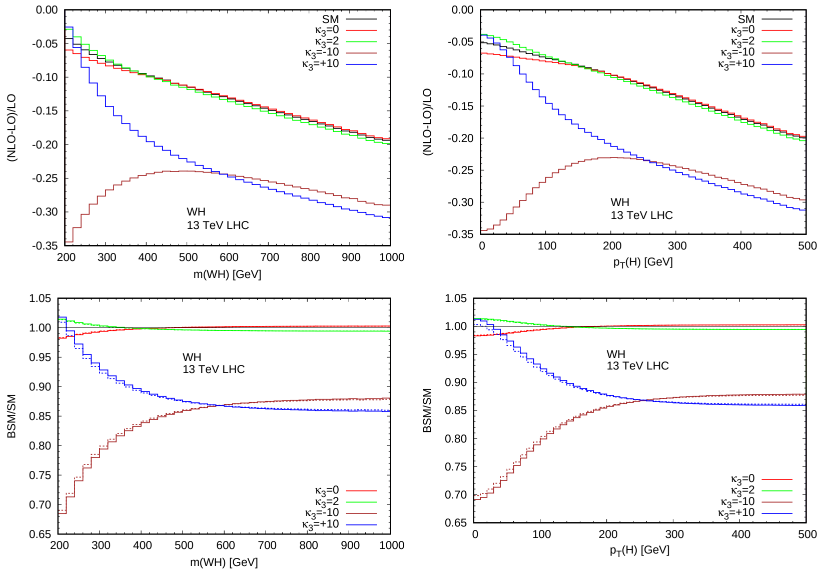

Figure 3.9: NLO EW corrections and effects of κ_3 are shown for WH production at 13 TeV LHC.

i.e. the ratio of NLO corrections between BSM and SM. In practice, it is our prediction at NLO EW accuracy for the signal strengths μ_i, while previous studies on κ_3 effects are at LO EW accuracy.

Firstly, we comment on the shape of the NLO EW corrections in the upper plots. In the tails, the NLO EW corrections in the SM is characterised by large negative Sudakov logarithms, especially for $p_T(H)$ in VH production. On one hand, C_1 is large in the threshold region, and changing the value of κ_3 will affect the shape of $\sigma_{\rm NLO}^{\rm BSM}/\sigma_{\rm LO}$, while it is not deformed in the tail. On the other hand, the change induced by κ_3 on $Z_H^{\rm BSM}$ results in a constant shift in the tail of distribution. We further notice that there is a small bump when $m(ZH)$ is around $2m_t$ or $p_T(H)$ is around m_t distribution in ZH production, which is due to the presence of top quark loop at NLO.

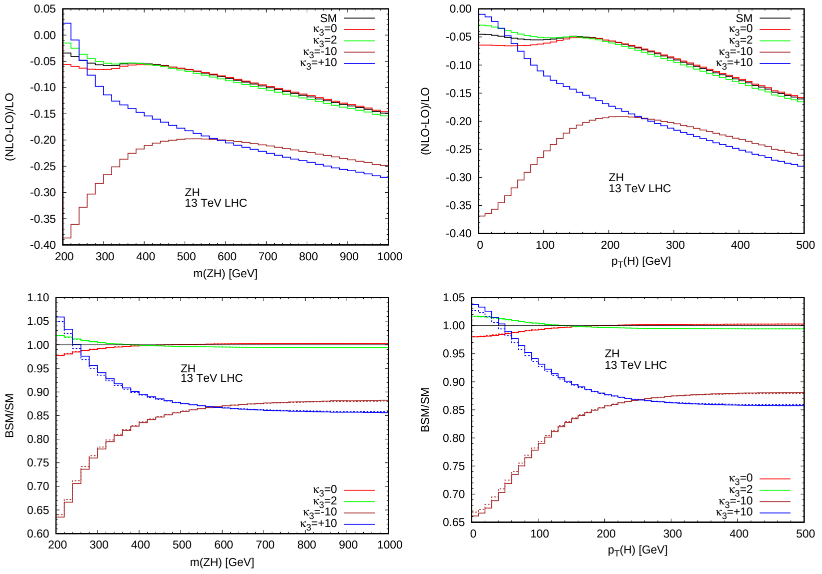

Figure 3.10: NLO EW corrections and effects of κ_3 are shown for ZH production at 13 TeV LHC.

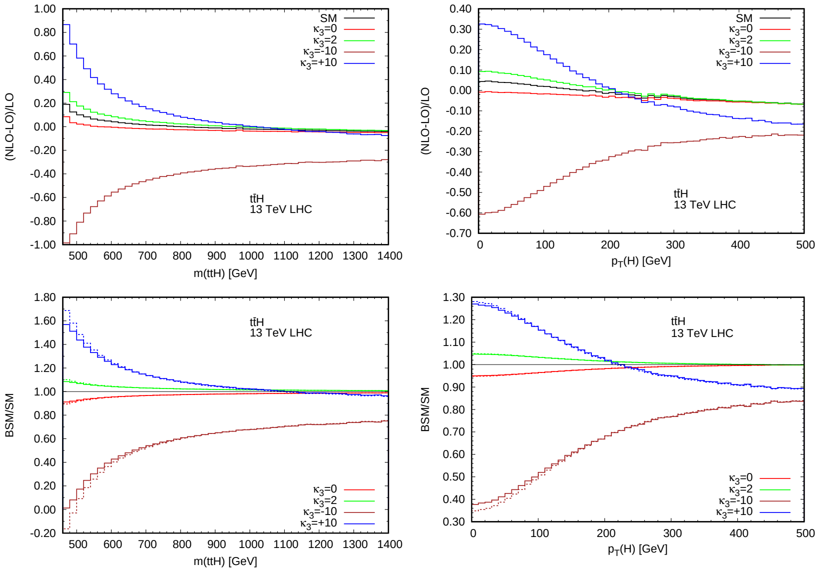

Figure 3.11: NLO EW corrections and effects of κ_3 are shown for $t\bar{t}H$ production at 13 TeV LHC.

In the lower plots in Fig. 3.9,3.10,3.11, we show the signal strengths, *i.e.* the ratio of the BSM and SM predictions, at NLO EW accuracy(solid lines) and LO EW accuracy(dashed lines). Solid and dashed lines are in general very close, which suggests that the sensitivity to κ_3 is unaffected by NLO EW corrections. It is very interesting to note that at the threshold region of $t\bar{t}H$, a value $\kappa_3 = -10$ leads to corrections that are negative and larger in absolute value than the LO, yielding negative cross section at this order. This is due to large C_1 in that region. On one hand, higher order κ_3-induced effects should be included, especially those coming from the square of one-loop contribution, so that the cross section could become positive. On the other hand, such large κ_3 implies a large Wilson coefficients of the corresponding EFT operator, which may break the validity of EFT approximation at this point. In any case, our theoretical prediction for such large κ_3 is unreliable.

3.1.3 Constraining κ_3

We define the signal strength as the ratio between BSM and SM at NLO EW accuracy, *i.e.*, for production channel i and decay channel f, as

$$\mu_i = \frac{\sigma(i)}{\sigma(i)^{\text{SM}}} \tag{3.10}$$

$$\mu^f = \frac{\text{BR}(f)}{\text{BR}^{\text{SM}}(f)} \tag{3.11}$$

$$\mu_i^f = \mu_i \times \mu^f \,, \tag{3.12}$$

where $i = (gg\text{F}, \text{VBF}, WH, ZH, t\bar{t}H)$, $f = \gamma\gamma, VV^*, ff$. This is also valid for differential distributions, where in that case $\sigma(i)$ refers the cross section in each bin instead of inclusive cross section.

The signal strength for production channel i is given by

$$\mu_i = \frac{\sigma_i^{\text{BSM}}}{\sigma_i^{\text{SM}}} = Z_H^{\text{BSM}} \left[\kappa_i^2 + \frac{(\kappa_3 - 1)}{K_{\text{EW}}} C_1 \right] \,, \tag{3.13}$$

where $\kappa_{gg\text{F}} = \kappa_{t\bar{t}H} = \kappa_t$ and $\kappa_{VH} = \kappa_{\text{VBF}} = \kappa_V$, *i.e.* we consider the scenario that the coupling between Higgs boson and top quark(vector boson) is scaled by a constant factor $\kappa_t(\kappa_V)$. K_{EW} and C_1 are corresponding values of K-factor and C_1 which depend on the specific production process. For differential distributions, corresponding differential K_{EW} and C_1 should be used. As noted above, we did not include κ_t and κ_V effects at one-loop. We will see in the results of the fit, the deviations on κ_t and κ_V will be at percent level and thus their effects at one-loop are negligible. On the other hand, we choose to resum the contribution due to NP in Higgs boson wave function renormalisation and thus terms of $\kappa_t^2\kappa_3^2$ and $\kappa_V^2\kappa_3^2$ are included. However, we verified that also such resummation has negligible impact on the results presented in the following.

Similarly, the signal strength for the Higgs decay channel f is given by

$$\mu_f = \frac{\mathrm{BR}^{\mathrm{BSM}}(f)}{\mathrm{BR}^{\mathrm{SM}}(f)} = \frac{\Gamma^{\mathrm{BSM}}(f)}{\Gamma^{\mathrm{SM}}(f)} \frac{\Gamma_H^{\mathrm{SM}}}{\Gamma_H^{\mathrm{BSM}}}\,, \tag{3.14}$$

where the partial decay width is given by

$$\Gamma^{\mathrm{BSM}}(f) = Z_H^{\mathrm{BSM}}(\kappa_f^2 + (\kappa_3 - 1)C_1^f)\Gamma_{\mathrm{LO}}^{\mathrm{SM}}(f)\,. \tag{3.15}$$

In order to ensure that the Higgs wave-function renormalisation does not affect the branching ratios, we resum the BSM contribution to the Higgs wave-function. Here we only keep the BSM contribution to Higgs self-couplings at NLO; the SM part is treated as part of full NLO EW corrections and we do not include them. For the $\gamma\gamma$ decay channel $\kappa_{\gamma\gamma}$ depends on κ_t and κ_V, $\kappa_{VV^*} = \kappa_V$, and $\kappa_{f\bar{f}} = 1$.

We focus on the future scenario at 14 TeV LHC (ATLAS-HL) considered in ref. [58]. We perform the fit considering two different scenarios on the uncertainties. In the first scenario (S1), only the statistical uncertainty is included. This assumption corresponds to the ideal situation where the theory and experimental systematic uncertainties are negligible. On the other hand, we consider a second scenario (S2), where both theory and experimental systematic uncertainties are taken into account, together with statistical uncertainties.

First, we consider only κ_3 can be different from the SM, *i.e.* we set $\kappa_t = \kappa_V = 1$, $\kappa_3 \neq 1$. In Fig. 3.12, we show the results under both scenarios, for different production channels. Note that for each production channel all decay channels are included. In the left plot of Fig. 3.12, we can see that in the scenario that only statistical uncertainty(S1) is included, the ggF-like channel provides the best constraints for κ_3, followed by $t\bar{t}H$-like channel. However, in the region $\kappa_3 < 1$ differential information does not lead to any significant improvements for all channels. On the other hand, in the region $\kappa_3 > 1$ we see a clear improvement due to differential information for $t\bar{t}H$ channel. In the right plot of Fig. 3.12, we shows that including theory and experimental systematic uncertaintes makes a difference. The $t\bar{t}H$ process is giving the strongest constraints in the region $\kappa_3 < 1$ and receives improvements from the differential information. This difference is due to the large systematic uncertainty in the ggF channel. Note that, the impact of the differential information for ggF production is not known.

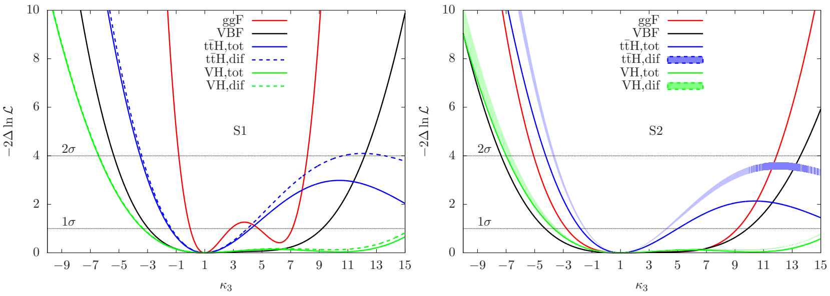

Figure 3.12: Results for κ_3 only fit in both scenarios.

Next, we perform the global fit including all experimental data as input and taking into account the anomalous couplings κ_t and κ_V. In Fig. 3.13 we present the combined bounds under four different assumptions: (κ_3) is anomalous; (κ_3, κ_t) are anomalous;(κ_3, κ_V) are anomalous;$(\kappa_3, \kappa_t, \kappa_V)$ are anomalous. In the presence of anomalous couplings other than κ_3, we marginalise over them and present the constraints on κ_3 only. In the left of Fig. 3.13 we show the results under scenarios S1, where only statistical uncertainties are included. As expected, the improvements due to including differential information are negligible. In the right of Fig. 3.13 we show the results under scenarios S2, where not only statistical uncertainties but also theoretical and experimental systematic uncertainties are included. We can see that in this scenario differential information leads to visible improvements on κ_3 constrains.

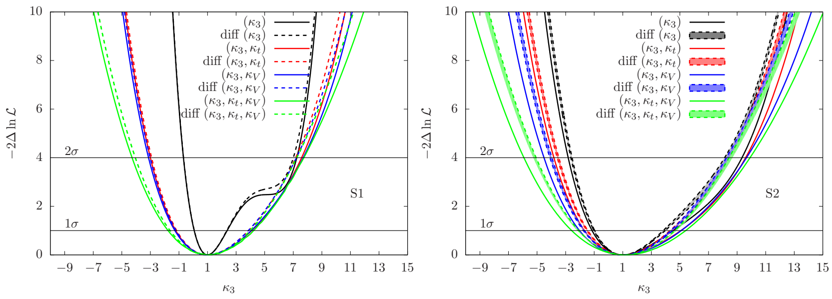

Figure 3.13: Results for κ_3 in both scenarios.

3.2 Triple Higgs and κ_4

We study triple Higgs production through gluon fusion at a future 100 TeV pp collider, $pp \to hhh$. We consider one Higgs boson decaying into a $b\bar{b}$ pair while the other Higgs bosons decaying into WW^*, and subsequently into leptons and jets, *i.e.* the final state $b\bar{b}\ell\ell\nu\nu jjjj$.

We interface the one-loop matrix element from MadGraph5_aMC@NLO [75] with VBFNLO [76–78]. For the backgrounds, we consider the two dominant backgrounds, namely $pp \to h(\to WW^*)t\bar{t}$ and $pp \to t\bar{t}W^+W^-$, and we generate them by MadGraph5_aMC@NLO. To veto further backgrounds from Z bosons, we only consider same-signed leptons in the final state.

In Table 3.2, we list the cross section of signal and backgrounds at 100 TeV pp collider. For the signal, we adopt the K-factor 2.0 estimated in Ref. [79]. For the $Ht\bar{t}$ background we use $K = 1.2$ [80], and for the $t\bar{t}W^+W^-$ background we adopt the K-factor 1.3 estimated in Ref. [81]. After taking into account branching ratio, in Table 3.2 we show the expected number of events for $30\,\mathrm{ab}^{-1}$ integrated luminosity. There are only 642 signal events in this final-state channel, and $\sim 10^7$ backgrounds events. Clearly, observing this channel is quite challenging.

To improve the sensitivity, we consider various features of signal and background. Firstly, we consider the parton-level results, without any parton shower and detector effects. In Fig. 3.14, we show the P_t distribution of visible final-state particles and missing transverse energy (MET). We find that the P_t dis-

Process	$\sigma \times BR$ (ab)	K-factor	Expected number of events
Signal	10.71	2.0	642
$h(WW^*)t\bar{t}$	2.55×10^5	1.2	9.18×10^6
$t\bar{t}W^-W^+$	3.68×10^4	1.3	1.55×10^6

Table 3.2: The cross section of signal and backgrounds for the $b\bar{b}\ell^\pm\ell^\pm jjjj + \not{E}$ final state at 100 TeV pp collider in the SM are shown, as well as the number of events corresponding to 30 ab^{-1} integrated luminosity.

tribution of the softest leptons and jets peak around $10\,\mathrm{GeV}$, which poses a challenge to reconstruct these objects.

Since there are two unobserved neutrinos in the final state, which can come from the decays of either on-shell or off-shell W bosons, reconstructing the W bosons and H bosons in the signal becomes difficult. Instead of attempting a full reconstruction, we consider a partial one. To extract this information, it is crucial to determine which jets and leptons come from one of the Higgs bosons. Considering there are four jets and two leptons in the final state, 12 different combinations need to be considered. To find the correct combination we adopt the following four methods:

1. The decay chain $H \to WW^* \to \ell\nu jj$ suggests that the lepton and hadronically decayed W boson should have a small distance $\Delta R(\ell, W_{jj})$. Since there are two Higgs bosons decaying semi-leptonically, we choose the combination with minimal value of $\Delta R_1(\ell, W_{jj}) + \Delta R_2(\ell, W_{jj})$.

2. The invariant masses of semi-leptonically decayed Higgs boson can be computed from the visible particles, and we denote them as $m_h^{\mathrm{vis}}(\ell, jj)$. We choose the combination which minimizes the sum $m_{h1}^{\mathrm{vis}}(\ell, jj) + m_{h2}^{\mathrm{vis}}(\ell, jj)$.

3. We compute the $mT2$ variable defined in Ref. [82–86] from the leptons, jets and MET. The observable is a lower bound on the Higgs mass, so we choose the combination which minimizes $mT2$.

4. The variable $mT2$ should have a value close to the Higgs mass, we choose the combination whose $mT2$ is closest to m_H, *i.e.* minimal $|mT2 - m_H|$.

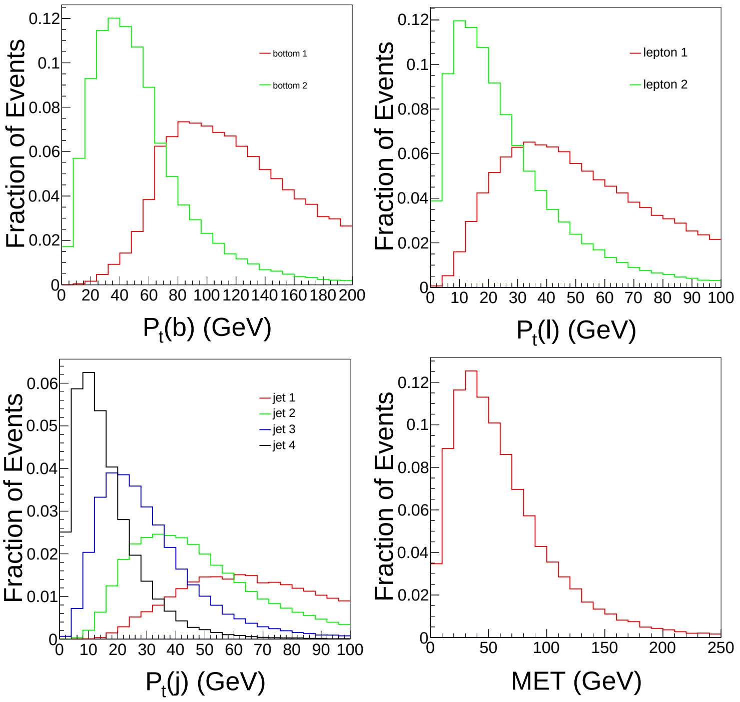

Figure 3.14: The kinematic distributions of final-state objects are shown, where the leptons, b-jets, and light jets are ordered by P_t.

Methods	The percentage of correctness
$\min[\Delta R_1(l,W_{jj})+\Delta R_2(l,W_{jj})]$	47.0%
$\min(m_{h1}^{\text{vis}}+m_{h2}^{\text{vis}})$	61.2%
$\min(mT2)$	66.8%
$\min\|mT2-m_H\|$	99.98%

Table 3.3: Methods for determining the correct combinations of (l,j,j) and their percentages of correctness.

In Table 3.3, we show the correctness of the above methods at parton level. We can see that the method relying on $\min|mT2-m_H|$ has the best performance, which can correctly assign almost all cases.

We use Pythia 6.4 [87] to perform parton shower and hadronization, to obtain hadronic events. We use DELPHES [88, 89] to perform detector simulation. Jets are clustered using anti-k_t algorithm [90] with $R = 0.5$ provided in the package FASTJET [91]. The setup of DELPHES is similar to Ref. [48], with the following modifications:

1. We assume the b-tagging efficiency is a constant $\epsilon_b = 0.7$, and mistagging rates are $\epsilon_c = 0.1$ for charm jets,and $\epsilon_j = 0.001$ for light jets. We require that the pseudorapidity for all jets to be $|\eta| < 5.0$.
2. We assume the efficiency of lepton identification is 95% when $P_t(\ell) > 5$ GeV and $|\eta_\ell| < 5.0$, and 0 otherwise.
3. We define isolated leptons as in Ref. [89]. That is to say, we compute the quantity

$$I(\ell) = \frac{\sum_{i\neq l}^{\Delta R<R, P_t(i)>P_t^{min}} P_t(i)}{P_t(l)}, \tag{3.16}$$

   where ℓ is a lepton. The sum in the numerator includes all other particles with $P_t > 0.1\,\text{GeV}$ within a cone with radius $R = 0.5$ around the ℓ. A lepton is considered to be isolated if $I(\ell) < 0.1$.

After the detector simulation, we apply three preselection cuts to enhance the signal over background ratio:

1. We require that at least one jet is tagged to be b jets. This can efficiently suppress backgrounds without b jets, while keeping a good efficiency for the signal.
2. To veto background including Z boson, we require the two leptons has the same electric charge, as discussed before. Note that this also removes half of signal events where they decay to opposite-sign leptons.
3. We require that there are at least 6 jets, including both b jets and light jets.

After the above preselection cuts, we first reconstruct the hadronically decayed Higgs boson. If at least two jets are tagged as b jets, the hardest two of them are combined and reconstructed as the hadronically decayed Higgs boson. In the case that only one jet is tagged as b jets, we combine it with one light jet which has the invariant mass $m(bj)$ closest to m_H, and we consider such light jet as b jet but failed to be tagged. In Fig. 3.15, we plot the invariant mass distribution $m(bb)$ of the hadronically decayed Higgs boson. We can see that the signal exhibits the expected $m(bb)$ peak around the Higgs mass, while the background is non-resonant. Furthermore, we plot $mT2$, m_{h1}^{vis}, and m_{h2}^{vis} in Fig. 3.15. While these observables should have an upper bound at the Higgs mass, many events show larger values. As discussed above, limitations in the reconstruction of the softest jet together with missing lepton isolation are responsible for this effect.

	Signal	$H(WW^*)t\bar{t}$	$t\bar{t}W^+W^-$
Preselection	24	9.73×10^5	2.59×10^6
$mT2 < 484$ GeV	23	9.40×10^5	2.35×10^5
$\lvert m_{bb} - m_h \rvert < 58$ GeV	21	6.73×10^5	1.42×10^5
$m_h^{\text{vis}} < 482$ GeV	21	6.72×10^5	1.42×10^5
S/B	2.56×10^{-5}		
$S/\sqrt{S+B}$	0.0231		

Table 3.4: Efficiencies of cuts are shown at 100 TeV pp collider with $30\,\text{ab}^{-1}$ integrated luminosity.

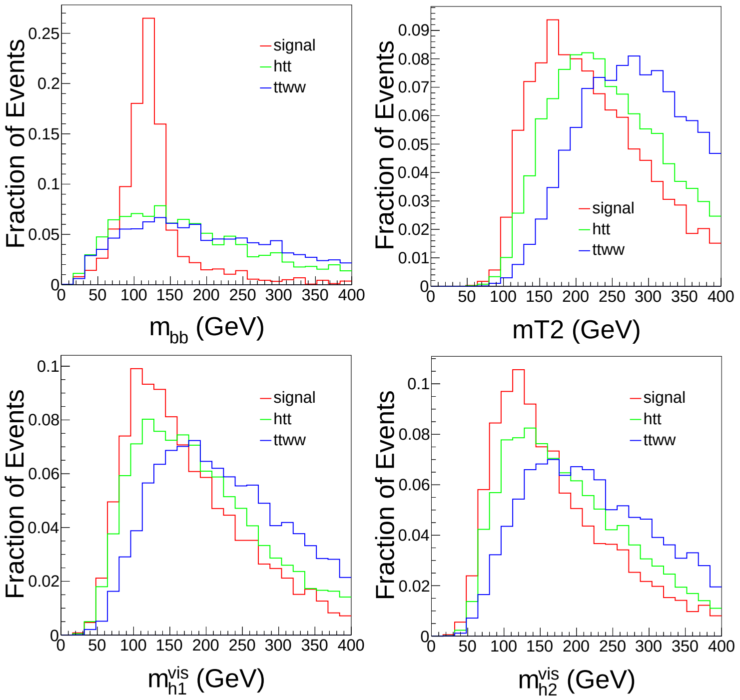

Figure 3.15: Distributions of reconstructed observables are shown for signal and backgrounds.

Nevertheless, we try to suppress the background by applying cuts on the above observables, and we list the efficiencies of each cut in Table 3.4. While $t\bar{t}W^+W^-$ backgrounds can be suppressed by an order of magnitude, the presence of a Higgs boson in $Ht\bar{t}$ backgrounds make it much harder to suppress. However, both backgrounds are still much larger than the signal, and the significance of the signal finally amounts to just 0.02, which is clearly much worse than could be expected from the parton-level calculation. We conclude that in the SM, measuring triple-Higgs production through this channel will be extremely challenging.

3.3 Double Higgs and κ_4

As discussed above, directly measuring κ_4 through triple Higgs boson production is extremely difficult even at future hadron collider. Considering other decaying channels such as $b\bar{b}b\bar{b}\gamma\gamma$ could be better than the $b\bar{b}WW^*WW^*$ considered above, but only a very loose bounds $\kappa_4 \in [-20, 30]$ can be obtained with $30\,\mathrm{ab}^{-1}$ integrated luminosity at 100 TeV pp collider. As in Sec. 3.1, we show that the indirect constraints to κ_3 through loop corrections to single Higgs boson processes are competitive to direct measurements, we would like to extend it to κ_4, by considering higher order corrections to double Higgs production.

3.3.1 Calculation Framework

We consider the loop correction involving κ_4 to the main production channel of Higgs boson pair at hadron colliders, *i.e.* the gluon fusion channel. At LO, the final state Higgs boson are produced through a heavy quark loop, dominated by the top quark loop due to its large Yukawa coupling. The amplitude depends on the Higgs cubic self-coupling linearly:

$$\mathcal{M}^{1\mathrm{L}} = \mathcal{M}_0^{1\mathrm{L}} + \bar{c}_6 \mathcal{M}_1^{1\mathrm{L}} \,. \tag{3.17}$$

As a result, the cross section depends on the Higgs cubic self-coupling quadratically:

$$\sigma_{\mathrm{LO}} = \sigma_0 + \sigma_1 \bar{c}_6 + \sigma_2 \bar{c}_6^2 \,. \tag{3.18}$$

At the two-loop level, the amplitudes receives contribution from $\bar{c}_6, \bar{c}_8$, and $\bar{c}_{10}$ (see Fig. 3.16), which can be written as

$$\begin{aligned}
\mathcal{M}^{2\mathrm{L}} =& \mathcal{M}^{2\mathrm{L}}_{00} + \mathcal{M}^{2\mathrm{L}}_{10}\bar{c}_6 && (3.19)\\
&+ \mathcal{M}^{2\mathrm{L}}_{20}\bar{c}_6^2 + \mathcal{M}^{2\mathrm{L}}_{30}\bar{c}_6^3 && (3.20)\\
&+ \mathcal{M}^{2\mathrm{L}}_{01}\bar{c}_8 + M^{2\mathrm{L}}_{11}\bar{c}_6\bar{c}_8 && (3.21)\\
&+ \mathcal{M}^{2\mathrm{L}}_{001}\bar{c}_{10}\,. && (3.22)
\end{aligned}$$

The terms in (3.19) are the NLO EW corrections to the contributions that appear already at LO. The quantity $M^{2\mathrm{L}}_{00}$, for instance, corresponds to the NLO EW corrections in the SM. The terms $\mathcal{M}^{2\mathrm{L}}_{10}$ is $\mathcal{O}(\alpha)$ corrections to $\mathcal{M}^{1\mathrm{L}}_{0}$. They should be included for precise determination of $\bar{c}_6$ values, yet being subdominant. We neglect both $\mathcal{M}^{2\mathrm{L}}_{00}$ and $\mathcal{M}^{2\mathrm{L}}_{10}$ in this first analysis, similarly to the case of single Higgs production.

The terms in (3.20) collect contributions that appear at NLO for the first time. For small values $\bar{c}_6 \ll 1$, these terms are suppressed w.r.t. $\mathcal{M}^{1\mathrm{L}}_{0}$ and $\mathcal{M}^{1\mathrm{L}}_{1}$ in (3.17), and may be neglected. However, we keep them in order to study the $\bar{c}_6$ and in turn κ_3 dependence beyond the linear approximation, which is not sufficient for large values of $\bar{c}_6$. As it has been discussed in ref. [92], its contribution can be large. Also, the presence of $(\bar{c}_6)^3$ effects indicates that terms up to the order $(v/\Lambda)^6$ have to be taken into account in the one-loop amplitudes and thus in the renormalisation constants. Schematically, each order in the (v/Λ) expansion implies that the following terms can be in principle present

$$\begin{aligned}
(v/\Lambda)^2 \to& \{\bar{c}_6\} && \to \{\lambda_3-\lambda\}, && (3.23)\\
(v/\Lambda)^4 \to& \{(\bar{c}_6)^2,\ \bar{c}_8\} && \to \{(\lambda_3-\lambda)^2, \lambda_4-\lambda\}^2, && (3.24)\\
(v/\Lambda)^6 \to& \{(\bar{c}_6)^3, \bar{c}_8\bar{c}_6, \bar{c}_{10}\} && \to \{(\lambda_3-\lambda)^3, (\lambda_3-\lambda)(\lambda_4-\lambda), \lambda_5\}. && (3.25)
\end{aligned}$$

Thus, the full dependence on λ_3 and λ_4 of the diagrams appearing in Fig. 3.16 is taken into account. On the other hand, $(v/\Lambda)^6$ terms include c_{10} contributions, which we re-parametrised in term of $\bar{c}_{10} \equiv (c_{10}v^6)/(\lambda\Lambda^6)$; they lead to an independent value also for λ_5, the factor in front of the H^5/v term appearing in $V^{\mathrm{NP}}(\Phi)$ after EWSB. The origin of the terms in (3.21) and (3.22) can be now understood on the base of Fig. 3.16 and eqs. (3.23)-(3.25) and are commented in the following. The terms in (3.21) are the contributions that depend on $\bar{c}_8$. Thus, they are the most relevant contributions in our study of double Higgs production, as they provide the sensitivity to $\bar{c}_8$ and therefore to the deviation from the quartic that one expects on top of the one determined by $\bar{c}_6$ only. Although the contribution from $\mathcal{M}_{11}^{2\mathrm{L}}$ would be suppressed for small c_6 we keep them to study the validity of our calculation in the $(\bar{c}_6, \bar{c}_8)$ plane, or equivalently (κ_3, κ_4) plane.

Finally, the last term (3.22), is related to $\bar{c}_{10}$-dependent contributions. These contributions arise from the diagram with the H^5 interactions in Fig. 3.16(g) and the corresponding term in the renormalisation constant δc_6 (see eq. (2.30) for the explicit δc_6 formula) entering Fig. 3.16(k), and can be expressed as

$$\mathcal{M}_{001}^{2\mathrm{L}} = \mathcal{M}_1^{1\mathrm{L}} \frac{5\lambda}{4\pi^2} (1 - \ln \frac{m_H^2}{\mu_{\mathrm{EFT}}}) \,. \tag{3.26}$$

Therefore, the contribution from that term can be written as a kinematically independent shift to $\bar{c}_6$,

$$\bar{c}_6 \to \bar{c}_6 + \frac{5\lambda\bar{c}_{10}}{4\pi^2}\left(1 - \log \frac{m_H^2}{\mu_{\mathrm{EFT}}^2}\right) \sim \bar{c}_6 + 0.016\bar{c}_{10}\left(1 - \log \frac{m_H^2}{\mu_{\mathrm{EFT}}^2}\right) \,. \tag{3.27}$$

In practice we can only constrain a linear combination of $\bar{c}_6$ and $\bar{c}_{10}$ that is in eq. (3.27). In the following we work in the assumptions that $\bar{c}_{10}$ effects are negligible and we set $\bar{c}_{10} = 1$, however, for not too large values of $\bar{c}_{10}$, *i.e.*, where the linear expansion in $\bar{c}_{10}$ is reliable, results of $\bar{c}_6$ can be translated into a linear combination of $\bar{c}_6$ and $\bar{c}_{10}$ via eq. (3.27).[1] In order to be directly sensitive to $\bar{c}_{10}$ one would need to consider one-loop effects in triple Higgs production, or evaluate quadruple Higgs production at the tree level.

In conclusion, in our phenomenological analysis, at two-loop level we evaluate $\bar{c}_6$ and $\bar{c}_8$ effects using the following approximation for the amplitude:

$$\mathcal{M}^{2\mathrm{L,pheno}} = \mathcal{M}_{\bar{c}_6}^{2\mathrm{L}} + \mathcal{M}_{\bar{c}_8}^{2\mathrm{L}} \,, \tag{3.28}$$

$$\mathcal{M}_{\bar{c}_6}^{2\mathrm{L}} = \mathcal{M}_{20}^{2\mathrm{L}} \bar{c}_6^2 + \mathcal{M}_{30}^{2\mathrm{L}} \bar{c}_6^3 \mathcal{M}_{\bar{c}_8}^{2\mathrm{L}} = \mathcal{M}_{01}^{2\mathrm{L}} \bar{c}_8 + \mathcal{M}_{11}^{2\mathrm{L}} \bar{c}_6 \bar{c}_8 \,, \tag{3.29}$$

---

[1] If $\bar{c}_{10}$ is so large that the shift induced by eq. (3.27) is even larger than $\bar{c}_6$ itself, then squared loop-diagrams involving the H^5 vertex would be larger than their interferences with Born diagrams. Thus, one-loop contributions, and consequently the level of accuracy of our calculation, would not be sufficient.

where we include all corrections from $\bar{c}_8$, but only the leading corrections induced by $\bar{c}_6$ are included. Using such approximation for the amplitude, we get the following approximation for the cross section at NLO,

$$\sigma_{\text{NLO}}^{\text{pheno}}(HH) \quad = \quad \sigma_{\text{LO}}(HH) + \Delta\sigma_{\bar{c}_6}(HH) + \Delta\sigma_{\bar{c}_8}(HH) \tag{3.30}$$

where $\Delta\sigma_{\bar{c}_6}$ captures the leading corrections induced by $\bar{c}_6$ on top of $\bar{c}_6$, and $\Delta\sigma_{\bar{c}_8}$ includes all $\bar{c}_8$ dependent contributions, *i.e.*

$$\Delta\sigma_{\bar{c}_6} \propto 2\text{Re}[\mathcal{M}^{1\text{L},*}\mathcal{M}^{2\text{L}}_{\bar{c}_6}] = 2\text{Re}[(\mathcal{M}^{1\text{L}}_0 + \bar{c}_6\mathcal{M}^{1\text{L}}_1)(\bar{c}_6^2\mathcal{M}^{2\text{L}}_{20} + \bar{c}_6^3\mathcal{M}^{2\text{L}}_{30})^*] \tag{3.31}$$

$$\Delta\sigma_{\bar{c}_8} \propto 2\text{Re}[\mathcal{M}^{1\text{L},*}\mathcal{M}^{2\text{L}}_{\bar{c}_8}] = 2\text{Re}[(\mathcal{M}^{1\text{L}}_0 + \bar{c}_6\mathcal{M}^{1\text{L}}_1)(\bar{c}_8\mathcal{M}^{2\text{L}}_{01} + \bar{c}_6\bar{c}_8\mathcal{M}^{2\text{L}}_{11})^*]\,. \tag{3.32}$$

In particular, we have

$$\Delta\sigma_{\bar{c}_6} = \bar{c}_6^2\left[\sigma_{30}\bar{c}_6 + \sigma_{40}\bar{c}_6^2\right] + \tilde{\sigma}_{20}\bar{c}_6^2 \tag{3.33}$$

$$\Delta\sigma_{\bar{c}_8} = \bar{c}_8\left[\sigma_{01} + \sigma_{11}\bar{c}_6 + \sigma_{21}\bar{c}_6^2\right]\,. \tag{3.34}$$

In other words, $\Delta\sigma_{\bar{c}_6}$ originate from the interference of $\mathcal{M}^{1\text{L}}$ with the terms with the largest dependence on $\bar{c}_6$, and $\Delta\sigma_{\bar{c}_8}$ corresponds to the interference of $\mathcal{M}^{1\text{L}}$ to all the terms depends on $\bar{c}_8$.

The two-loop contributions entering the different $\mathcal{M}_{ij}$ sub-amplitudes can be classified into three types:

- Factorisable contribution ($\mathcal{F}$);
- Non-factorisable contribution ($\mathcal{N}$);
- Higgs wave-function counter terms ($\mathcal{W}$);

The first category can be evaluated based on UV-finite form factors $P[HH]$, $V[HHH]$ given in App. A. The Higgs wave-function renormalisation constant involves a quadratic dependence on κ_3 and its contribution is UV-finite. We do not include their contributions in the $P[HH]$ and $V[HHH]$ form factors,

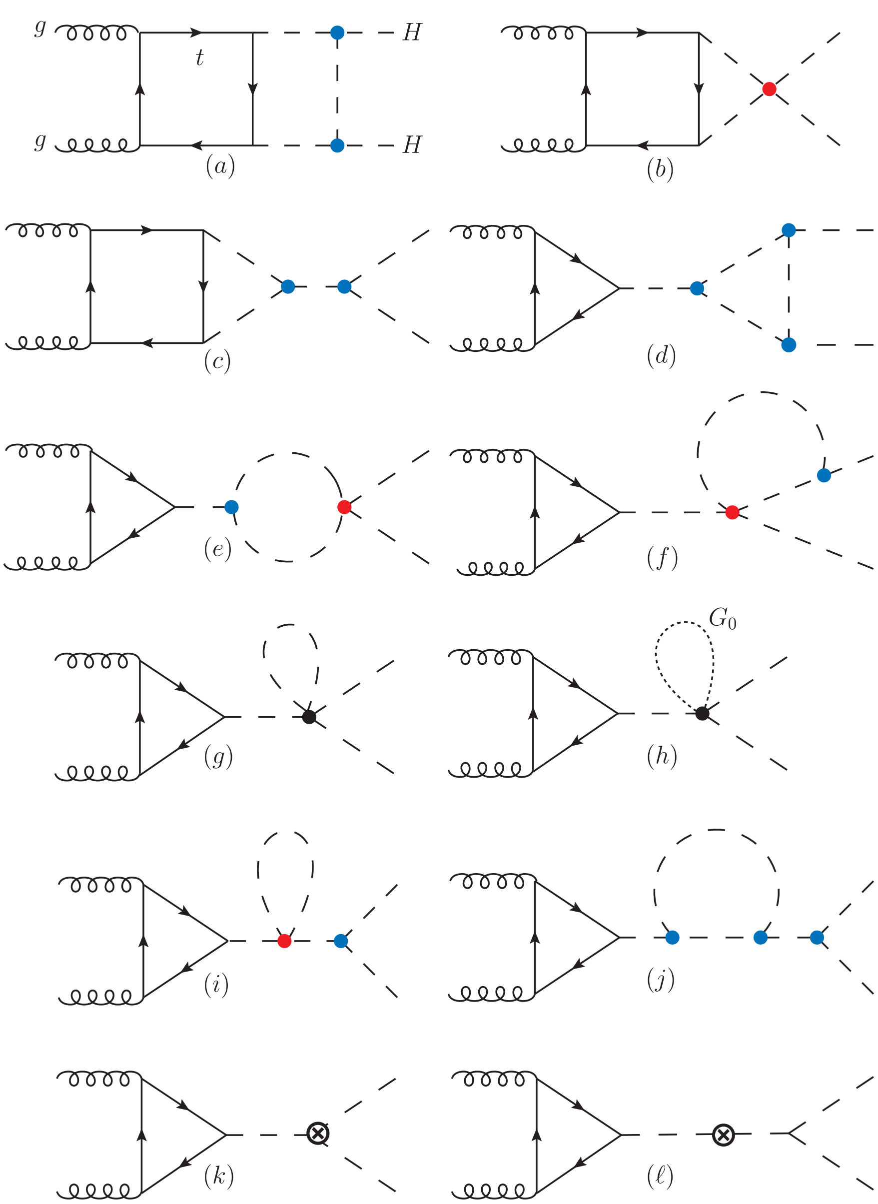

Figure 3.16: Representative Feynman diagrams for the two-loop corrections to $gg \to HH$ are shown.

and they should be separately added, as the third category $\mathcal{W}$. Indeed, it can be easily calculated based on the SM contribution of Higgs cubic self-coupling to the Higgs wave-function $\delta Z_H^{\mathrm{SM},\lambda}$ given in Eq. (3.2).

Based on the above classifications, we can divide different $\mathcal{M}_{ij}^{\mathrm{2L}}$ terms into

$$\mathcal{M}_{20}^{\mathrm{2L}} = \mathcal{M}_{20}^{\mathcal{W}} + \mathcal{M}_{20}^{\mathcal{F}} + \mathcal{M}_{20}^{\mathcal{N}} \,, \tag{3.35}$$

$$\mathcal{M}_{30}^{\mathrm{2L}} = \mathcal{M}_{30}^{\mathcal{W}} + \mathcal{M}_{30}^{\mathcal{F}} \,, \tag{3.36}$$

$$\mathcal{M}_{01}^{\mathrm{2L}} = \qquad \mathcal{M}_{01}^{\mathcal{F}} + \mathcal{M}_{01}^{N} \,, \tag{3.37}$$

$$\mathcal{M}_{11}^{\mathrm{2L}} = \qquad \mathcal{M}_{11}^{\mathcal{F}} . \tag{3.38}$$

Furthermore, we divide the amplitude according to its helicity structure. In detail, the amplitude includes both spin-0 and spin-2 component. At LO, the triangle is solely spin-0, and the box includes both component. All two-loop contribution considered here are solely spin-0, except topology (a). Therefore, we further define

$$\begin{aligned} \mathcal{M}_{0,20} &= \mathcal{M}_{0,20}^{\mathcal{W}} + \mathcal{M}_{0,20}^{\mathcal{F}} + \mathcal{M}_{0,20}^{\mathcal{N}} \,, \\ \mathcal{M}_{2,20} &= \mathcal{M}_{2,20}^{\mathcal{W}} + \qquad + \mathcal{M}_{2,20}^{\mathcal{N}} \,, \end{aligned} \tag{3.39}$$

where the first subscript denotes the spin component. With this notation we can directly express the wave-function contributions as

$$\mathcal{M}_{0,20}^{\mathcal{W}} = \delta Z_H^{\mathrm{SM},\lambda_3} (2\mathcal{M}_{0,1}^{\mathrm{1L}} + \mathcal{M}_{0,0}^{\mathrm{1L}}) \tag{3.40}$$

$$\mathcal{M}_{2,20}^{\mathcal{W}} = \delta Z_H^{\mathrm{SM},\lambda_3} \mathcal{M}_{2,0}^{\mathrm{1L}} \tag{3.41}$$

$$\mathcal{M}_{30}^{\mathcal{W}} = \mathcal{M}_{0,30}^{\mathcal{W}} = \delta Z_H^{\mathrm{SM},\lambda_3} \mathcal{M}_{0,1}^{\mathrm{1L}} \,. \tag{3.42}$$

Therefore, both the factorisable and wave-function contribution can be calculated based on Eq. and $P[HH]$ and $V[HHH]$ form factors. Only the non-factorisable contribution($\mathcal{N}$) are missing, which involves non-trivial two-loop diagrams.

All the non-factorisable ($\mathcal{N}$) contribution comes from the topologies (a),(b), and (c),

$$\mathcal{M}^{\mathcal{N}}_{2,20},\ \mathcal{M}^{\mathcal{N}}_{0,20} \Longleftarrow \mathcal{M}_a = 2(\mathcal{M}_{a_1} + \mathcal{M}_{a_2} + \mathcal{M}_{a_3})\,, \tag{3.43}$$

$$\mathcal{M}^{\mathcal{N}}_{0,01} = \mathcal{M}^{\mathcal{N}}_{01} \Longleftarrow \mathcal{M}_b = 2\mathcal{M}_{b_1} + \mathcal{M}_{b_2}\,, \tag{3.44}$$

$$\mathcal{M}^{\mathcal{N}}_{0,20} \Longleftarrow \mathcal{M}_c = \mathcal{M}_b \times \frac{6v^2}{\lambda_4}\frac{\lambda_3^2}{s - m_H^2}\,. \tag{3.45}$$

Due to several scales are involved in those non-factorisable two-loop diagrams, we adopt numerical methods to calculate them. Firstly we generated two-loop diagrams with QGRAF [93], and processes with FORM [94] in $d = 4 - 2\epsilon$ dimensions. We project the amplitudes onto spin-0 and spin-2 form factors. In detail, assigning the following on-shell p_i momenta to the external particles:

$$g(p_1) + g(p_2) \to H(-p_3) + H(-p_4) \tag{3.46}$$

where all the momenta are considered as incoming. Then both $\mathcal{M}^{1\mathrm{L}}$ and $\mathcal{M}^{2L}$, and any of their gauge-invariant sub-amplitudes, can be projected onto the spin-0 bases $\mathcal{A}_0$ and the spin-2 bases $\mathcal{A}_2$. Specifically,

$$\mathcal{M}^{\mu_1\mu_2}\epsilon_{1,\mu_1}\epsilon_{2,\mu_2} = \delta^{c_1c_2}\mathcal{A}_0^{\mu_1\mu_2}\epsilon_{1,\mu_1}\epsilon_{2,\mu_2}F_0 + \delta^{c_1c_2}\mathcal{A}_2^{\mu_1\mu_2}\epsilon_{1,\mu_1}\epsilon_{2,\mu_2}F_2\,, \tag{3.47}$$

where ϵ_1 and ϵ_2 are the (transverse) polarisation vectors for the two incoming gluons, with μ_1 and μ_2(c_1 and c_2) being their corresponding Lorentz(colour) indices. We choose to normalise the tensor bases according to the following conditions:

$$\mathcal{A}_0 \cdot \mathcal{A}_0 = \mathcal{A}_2 \cdot \mathcal{A}_2 = 2, \mathcal{A}_0 \cdot \mathcal{A}_2 = 0\,. \tag{3.48}$$

Explicitly, we have[2]

$$\mathcal{A}_0^{\mu_1\mu_2} = \sqrt{\frac{2}{d-2}}\left(g^{\mu_1\mu_2} - \frac{p_1^{\mu_2}p_2^{\mu_1}}{p_1\cdot p_2}\right)\,, \tag{3.49}$$

$$\mathcal{A}_2^{\mu_1\mu_2} = \sqrt{\frac{d-2}{2(d-3)}}\left(-\frac{d-4}{d-2}\left[g^{\mu_1\mu_2} - \frac{p_1^{\mu_2}p_2^{\mu_1}}{p_1\cdot p_2}\right] + g^{\mu_1\mu_2}\right. \tag{3.50}$$

$$\left. + \frac{(p_3\cdot p_3)p_1^{\mu_2}p_2^{\mu_1} + (2p_1\cdot p_2)p_3^{\mu_1}p_3^{\mu_2} - (2p_1\cdot p_3)p_2^{\mu_1}p_3^{\mu_2} - (2p_2\cdot p_3)p_3^{\mu_1}p_1^{\mu_2}}{p_T^2(p_1\cdot p_2)}\right)\,, \tag{3.51}$$

where $p_t^2 = (s_{13}s_{23} - m_H^4)/s_{12}$ is the square of the Higgs boson transverse momentum and we use the convention $s_{ij} = (p_i + p_j)^2$.

After the above projection, the non-factorisable amplitudes are written in terms of form factors, *i.e.* $F^{\mathcal{N}}_{0,20}$, $F^{\mathcal{N}}_{2,20}$, and $F^{\mathcal{N}}_{0,01}$, where

$$F^{\mathcal{N}}_{0,20} = F_{0,a} + F_{0,c} \tag{3.52}$$

$$F^{\mathcal{N}}_{2,20} = F_{2,a} \tag{3.53}$$

$$F^{\mathcal{N}}_{0,01} = F_{0,b}\,. \tag{3.54}$$

The form factors $F_{0,a}$, $F_{0,b}$, $F_{0,c}$ and $F_{2,a}$ are computed with PYSECDEC [96, 97]. PYSECDEC can compute loop integrals with massive internal lines and/or off-shell legs.

Before using PYSECDEC, we simplify the numerators of the loop integrals in the form factors, to optimise the speed of the computation. We note that the form factors $F_{0,a}$ and $F_{2,a}$ involve 7-propagator diagrams while $F_{0,b}$ and $F_{0,c}$ only involve up to 6-propagator ones. For simplicity, some overall factors such as coupling constants are removed from the tensor integrals. In particular, the quantities directly evaluated via PYSECDEC are $\tilde{F}_{0,a}$,$\tilde{F}_{2,a}$, and $\tilde{F}_{0,b}$, which are

---

[2] The expression for the second projector in Ref. [95] contains a typo that is corrected here.

related to the form factors through following relations:

$$F_{0,a} = \frac{1}{2} g_s^2 \frac{m_t^2}{v^2} (6\lambda v)^2 \left(\frac{i}{16\pi^2}\right)^2 \frac{1}{2} \tilde{F}_{0,a}\,, \tag{3.55}$$

$$F_{2,a} = \frac{1}{2} g_s^2 \frac{m_t^2}{v^2} (6\lambda v)^2 \left(\frac{i}{16\pi^2}\right)^2 \frac{1}{2} \tilde{F}_{2,a}\,, \tag{3.56}$$

$$F_{0,b} = \frac{1}{2} g_s^2 \frac{m_t^2}{v^2} (6\lambda) \left(\frac{i}{16\pi^2}\right)^2 \frac{1}{2} \tilde{F}_{0,b}\,, \tag{3.57}$$

$$F_{0,c} = \frac{1}{2} g_s^2 \frac{m_t^2}{v^2} (6\lambda v)^2 \frac{1}{s - m_H^2} \left(\frac{i}{16\pi^2}\right)^2 \frac{1}{2} \tilde{F}_{0,b}\,. \tag{3.58}$$

To improve the speed and convergence of the numerical evaluation, we adopt several further optimisations. Firstly, we only compute the finite parts. To handle it properly, we multiply the integrands with their prefactors which depends on ϵ, before the integration. We have cross-checked for several phase space points that UV-divergences cancel at the amplitude level, although individual integrals can be UV-divergent. Secondly, we add the integrals with the same denominator structure together before numerical integration. We have checked that summing integrals with different denominators prior to numerical integration does not improve the convergence. Thirdly, we choose different integrator for different integrals. For integrals with up to 5 dimension, we found that CUHRE [98] is very fast and accurate. Beyond 5 dimensions, we choose the integrator VEGAS [99]. Both integrators give a χ^2 estimate, and in the case that CUHRE reports too large χ^2 value, we perform the numerical integration with VEGAS, which is more adaptive but generally slower.

We have already mentioned that we checked the UV finiteness of the form factors explicitly. We further cross-checked the large m_t limits for the (b) and (c) topologies against analytical results [56] after setting $s_{12} = m_H^2$. For the (a) topology (double-box), we have numerically tested that by setting the mass in the Higgs propagator connecting the two final-state Higgs to be m_X artificially, it reduces to (b) topology in the limit $m_X \to \infty$ with an effective Higgs quartic coupling $\lambda_4 = -2\lambda_3^2/m_X^2$.

For phenomenological predictions, the partonic squared matrix-elements have to be integrated over the phase-space and convoluted with PDFs, which requires the evaluation of the matrix-elements at many phasespace points. Since the speed of evaluating the non-factorisable factors is slow, we build grids based on the numerical results evaluated at several pre-chosen points. Firstly, let us consider the spin-0 component at two loops. The form factor $\tilde{F}_{0,b}$ depends on only one kinematic variable s, hence a one-dimensional grid is sufficient. We sampled several values of s and perform a linear interpolation, and the grid points are shown in Fig. 3.17. We can see that $\tilde{F}_{0,b}$ features branch points at the threshold $\sqrt{s} = 2m_H$ and $\sqrt{s} = 2m_t$.

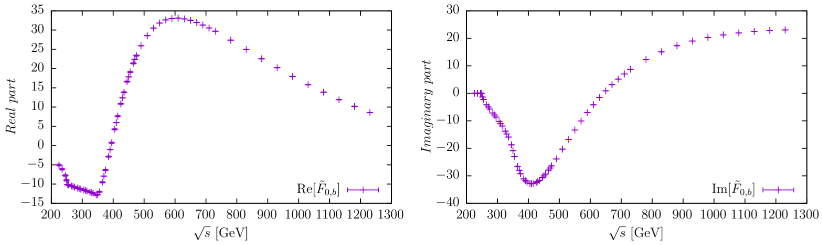

Figure 3.17: The grid points for the form factor $\tilde{F}_{0,b}$ are shown.

By contrast, the double-box diagrams depend on both s and the scattering angle θ. Therefore, we approximate it by the first few terms in the partial wave expansion [100] as

$$\tilde{F}_{0,a}(s,\theta) = \sum_{i=0}^{\infty} a'_i(s) d^i_{0,0}(\theta) = \sum_{i=0}^{\infty} a_i(s) P_i(\cos\theta)\,. \tag{3.59}$$

We found that the θ dependence is rather weak, especially for $s_{12} < 4m_t^2$, *i.e.* below the top-pair threshold. In that phasespace region the top-quark loop can be integrated out, obtaining an effective $HHgg$ coupling between the Higgs boson and the gluons. In such an EFT description corresponding to $m_t \to \infty$ limit there is no θ dependence. Therefore, the dominant contribution comes from the term without θ dependence, which is the $a_0(s)$ term. In order to check the θ dependence and test the validity of the partial wave expansion, we do not only include the first term by also the second term, *i.e.* we adopt the following approximation[3]

$$\tilde{F}_{0,a}(s,\theta) \approx a_0(s) + a_2(s) P_2(\cos\theta) \tag{3.60}$$

---

[3] Since $gg \to HH$ is symmetric, the $a_i(s)$ coefficients are zero for odd i.

For each value of s, different values of θ have been sampled, and we perform a linear regression to obtain the value of $a_0(s)$ and $a_2(s)$. Afterwards, we perform linear interpolations on $a_0(s)$ and $a_2(s)$ separately. In Fig. 3.18 we show the values of $a_0(s)$ and $a_2(s)$. We found that both the real parts and imaginary parts of $a_2(s)$ are much smaller than those of $a_0(s)$. Therefore, contributions from $a_i(s)(i > 2)$ terms are expected to be even smaller. Furthermore we have comparing the value obtained with the approximation and the actual value obtained to check the contribution of missing higher-order terms in the partial wave expansion. We can conclude that the truncation uncertainty is at the $\mathcal{O}(1\%)$ level. Similarly to $\tilde{F}_{0,b}$, both $a_0(s)$ and $a_2(s)$ have branch points at the thresholds $\sqrt{s} = 2m_H$ and $\sqrt{s} = 2m_t$.

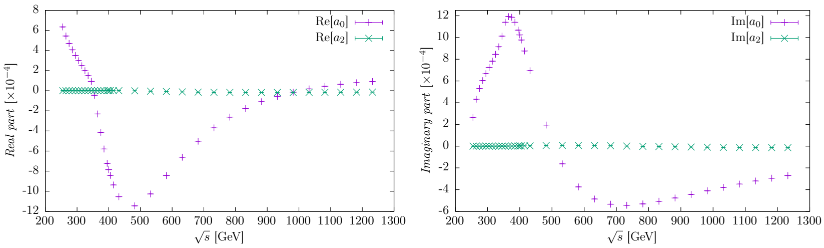

Figure 3.18: The values of $a_0(s)$ and $a_2(s)$ in the grid are shown.

Different from the spin-0 contribution $\tilde{F}_{0,a}$, the spin-2 contribution $\tilde{F}_{2,a}$ has a large dependence on θ. However, we have verified that its contribution is strongly suppressed respecting to the spin-0 contribution. Therefore we neglect the spin-2 contribution in our phenomenological study.

3.3.2 Numerical results

For the numerical calculation, we adopt the following input parameters for the masses of heavy particles

$$m_t = 173.2\,\text{GeV}, \quad m_W = 80.385\,\text{GeV}, \tag{3.61}$$

$$m_Z = 91.1876\,\text{GeV}, \quad m_H = 125.09\,\text{GeV}\,, \tag{3.62}$$

$\sqrt{s}$ [TeV]	$\sigma_{\rm LO}^{\rm SM} = \sigma_0$ [fb]	σ_1 [fb]	σ_2 [fb]
14	19.49 -	-15.59 (-80.0%)	5.414 (27.8%)
27	78.30 -	-59.39 (-75.8%)	19.58 (25.0%)
100	790.8 -	-556.8 (-70.5%)	170.8 (21.6%)

Table 3.5: The LO contributions to $\sigma_{\rm NLO}^{\rm pheno}$ are shown at hadron colliders with different collider energies, as well as their ratio with σ_0 at corresponding energy.

$\sqrt{s}$ [TeV]	$\tilde{\sigma}_{20}$ [fb]	σ_{30} [fb]	σ_{40} [fb]	σ_{01} [fb]	σ_{11} [fb]	σ_{21} [fb]
14	0.7112 (3.6%)	-0.5427 (-2.8%)	0.0620 (0.3%)	0.3514 (1.8%)	-0.0464 (-0.2%)	-0.1433 (-0.7%)
27	2.673 (3.4%)	-1.936 (-2.5%)	0.2102 (0.3%)	1.3552 (1.7%)	-0.137 (-0.2%)	-0.5127 (-0.7%)
100	24.55 (3.1%)	-16.53 (-2.1%)	1.663 (0.2%)	12.932 (1.6%)	-0.88 (-0.1%)	-4.411 (-0.6%)

Table 3.6: The two-loop contributions to $\sigma_{\rm NLO}^{\rm pheno}$ are shown at hadron colliders with different collider energies, as well as their ratio with σ_0 at corresponding energy.

and all the other masses are set to be zero. We renormalise the fine-structure constant α in the G_μ-scheme and we use the input parameter

$$G_\mu = 1.166\,378\,7 \times 10^{-5}\,\mathrm{GeV}^{-2}\,. \tag{3.63}$$

We set the renormalisation scale for α_S and factorisation scale to be $\mu_R = \mu_F = \frac{1}{2}m(HH) = \frac{1}{2}\sqrt{\hat{s}}$, and we use the PDF set CT14LO [101]. We set the renormalisation scale for $\bar{c}_6, \bar{c}_8$ to $\mu_{\mathrm{EFT}} = 2m_H$.

In Table 3.5, we list the three LO contributions to $\sigma^{\mathrm{pheno}}_{\mathrm{NLO}}$ at 14, 27 and 100 TeV pp colliders. Similarly, in Table 3.6, we list the two-loop contributions to $\sigma^{\mathrm{pheno}}_{\mathrm{NLO}}$. In addition to the value of each σ_{ij}, we also show their ratio with the LO prediction in the SM $\sigma_0 = \sigma^{\mathrm{SM}}_{\mathrm{LO}}$. As we can see in both tables, while all cross sections grow with the energy, the contributions induced by $\bar{c}_6$ and $\bar{c}_8$ mildly decrease in comparison with $\sigma^{\mathrm{SM}}_{\mathrm{LO}}$.

In Fig. 3.19, we show the results for the ratio $\sigma^{\mathrm{pheno}}_{\mathrm{NLO}}/\sigma^{\mathrm{SM}}_{\mathrm{LO}}$(top) and the ratio $\sigma^{\mathrm{pheno}}_{\mathrm{NLO}}/\sigma_{\mathrm{LO}}$(bottom) at 14 TeV pp collider. In the plots we consider the region $|\bar{c}_6| < 5$, $|\bar{c}_8| < 31$ which is determined by perturbativity. We show the results in both $(\bar{c}_6, \bar{c}_8)$ plane(left) and (κ_3, κ_4) plane. The upper plots show the ratio between our phenomenological prediction and the SM cross section, and we can see that for $\bar{c}_6 < 0$ the dependence on $\bar{c}_8$ is small, while for $\bar{c}_6 > 0$ the dependence on $\bar{c}_8$ is sizable. We note that while we expect outside this region perturbativity is broken, even inside this region our prediction may not be reliable for some choices of $(\bar{c}_6, \bar{c}_8)$. For example, in the up-right corner $(\bar{c}_6 \to 5, \bar{c}_8 \to 31)$ the cross sections becomes negative, and in the down-right corner $(\bar{c}_6 \to 5, \bar{c}_8 \to 31)$ the NLO corrections become larger than LO prediction. We note that in those cases we have large absolute value of $\bar{c}_6$ and $\bar{c}_8$, which may break the validity of EFT approximation. Including higher order corrections and/or the missing σ_{00}, σ_{01} terms may restore perturbativity, however it still implies that our current prediction is not reliable. For the phenomenological studies, we exclude the region where we get negative cross section, since it is clearly unphysical. We do not exclude explicitly the region where NLO corrections are larger than LO prediction, as it may be fixed by including the missing terms and/or higher order corrections.

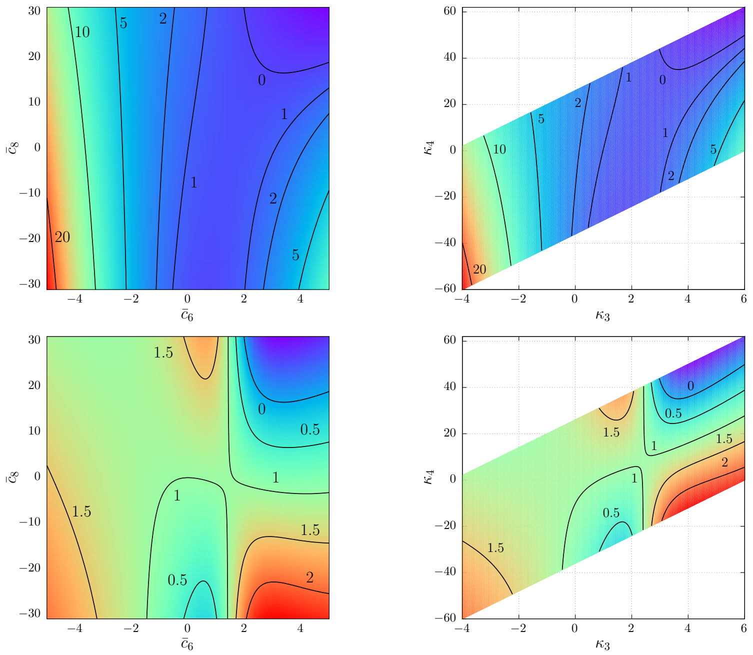

Figure 3.19: Contour plots at 14 TeV pp collider for $\sigma^{\text{pheno}}_{\text{NLO}}/\sigma^{\text{SM}}_{\text{LO}}$(top) and $\sigma^{\text{pheno}}_{\text{NLO}}/\sigma_{\text{LO}}$(bottom). In the left plots we show results in the $(\bar{c}_6, \bar{c}_8)$ plane, while right plots are in the (κ_3, κ_4) plane.

In Fig. 3.20, we show the $m(HH)$ distribution for σ_i(upper) and σ_{ij}(lower) contribution at 14 TeV. In the case of negative values we plot their absolute values and display the results as dashed lines. Furthermore, in Fig. 3.21 we show the ratio of $\sigma_{i(j)}$ to $\sigma^{\text{SM}}_{\text{LO}}$. In these plots the ratio are displayed as black lines, and we show the same quantity at the inclusive level with green lines. We found that the $\bar{c}_6$- and $\bar{c}_8$-induced contributions are more important close to threshold. In addition, the quantities σ_1, σ_{30}, and σ_{21} are negative. Therefore, large cancellations are present and the $m(HH)$ distribution strongly depend on the value of $\bar{c}_6$ and $\bar{c}_8$. To show this more explicitly, in Fig. 3.22 we show the $m(HH)$ distribution of σ_{LO} for representative values of $\bar{c}_6$, *i.e.* $\bar{c}_6 = \pm1, \pm2, \pm4$. Moreover, we also show the quantities $\Delta\sigma_{\bar{c}_6}$,$\Delta\sigma_{\bar{c}_8}/\bar{c}_8$ which is corresponding to the two-loop contribution induced by $\bar{c}_6$, and the two-loop $\bar{c}_8$-dependent part. We found that the normalisation and shape of σ_{LO} strongly

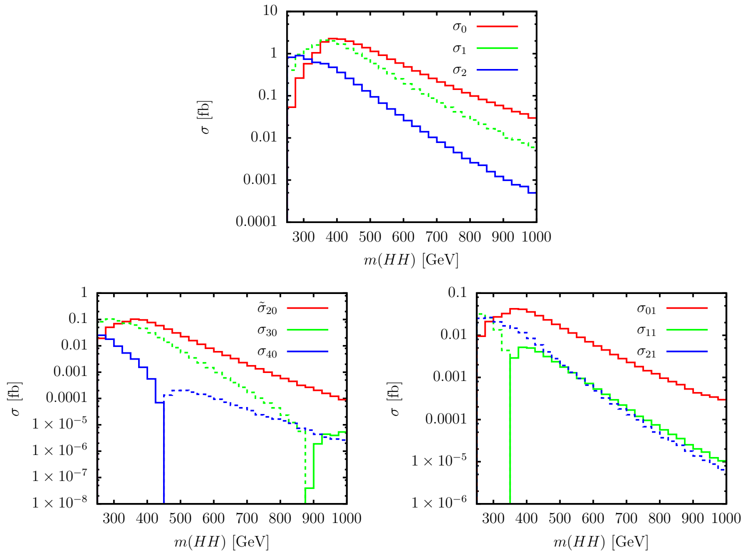

Figure 3.20: The $m(HH)$ distribution for individual σ_i and σ_{ij} at 14 TeV pp collider are shown.

depend on $\bar{c}_6$, and the difference in shape is crucial to discriminate different $\bar{c}_6$ values leading to the same total cross section, and we will show it latter in our analysis. The $\Delta\sigma_{\bar{c}_6}$ corrections grow for large $|\bar{c}_6|$, and both $\Delta\sigma_{\bar{c}_6}$ and $\Delta\sigma_{\bar{c}_8}/\bar{c}_8$ are larger when close to the threshold, as expected.

3.3.3 Constraining the Higgs self-couplings

Now we discuss the constraints on $\bar{c}_6$ and $\bar{c}_8$ that can be achieved from measurements of double Higgs production at the LHC and a 100 TeV future hadron collider. We consider the $b\bar{b}\gamma\gamma$ signature, which has been identified as the most promising channel and allow for the reconstruction of the di-Higgs invariant mass $m(HH)$. We follow the study of Ref. [22] for the case of HL-LHC and 100 TeV collider. In detail, we use the same selection cuts for the $b\bar{b}\gamma\gamma$ signature, and we divide the reconstructed $m(HH)$ distribution in the same six bins and for each bin we take the predictions for the background and for the signal in the SM directly from Ref. [22]. We note that results in Ref. [22] take into account higher-order QCD corrections for both the signal and the backgrounds and also parton showering, hadronisation and detector effects. As already said,

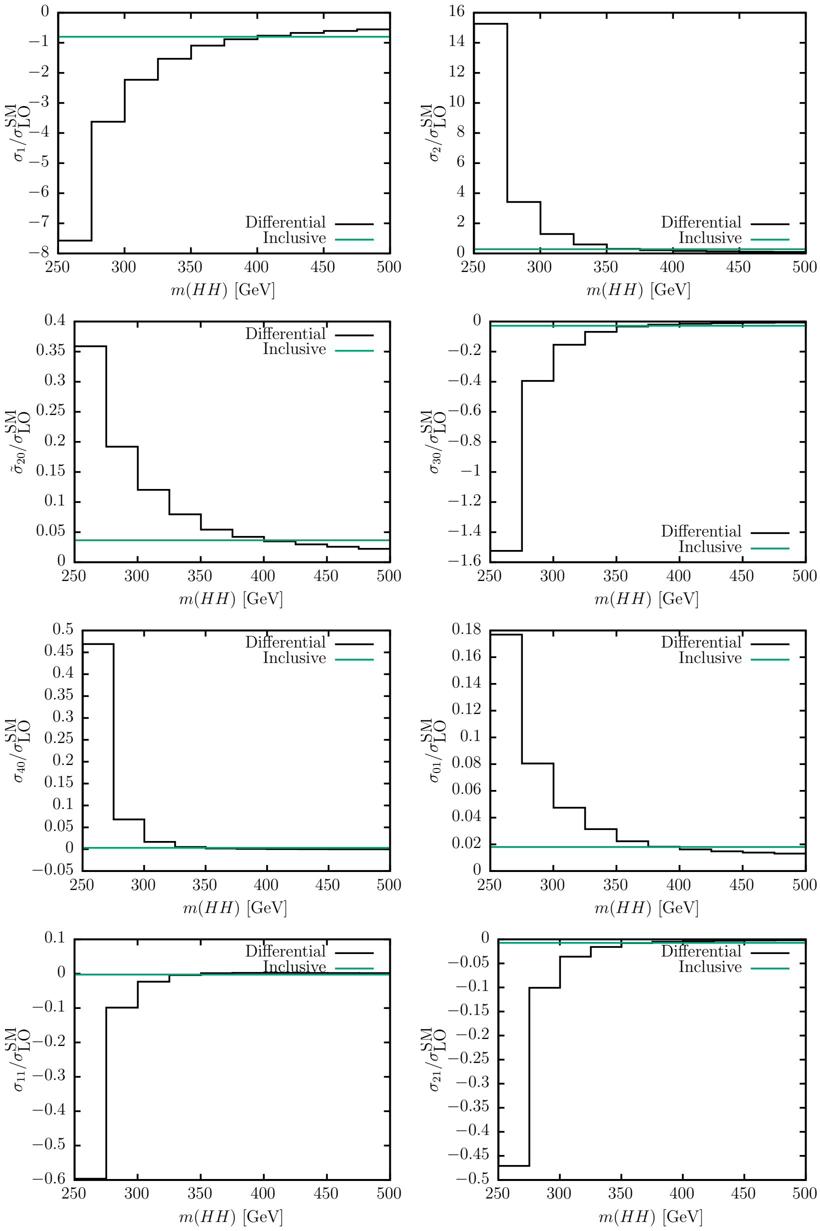

Figure 3.21: The ratio between $\sigma_{i(j)}$ contribution and $\sigma_{\rm LO}^{\rm SM}$ are shown at 14 TeV pp collider, on $m(HH)$ distribution(black) and on inclusive cross section(green).

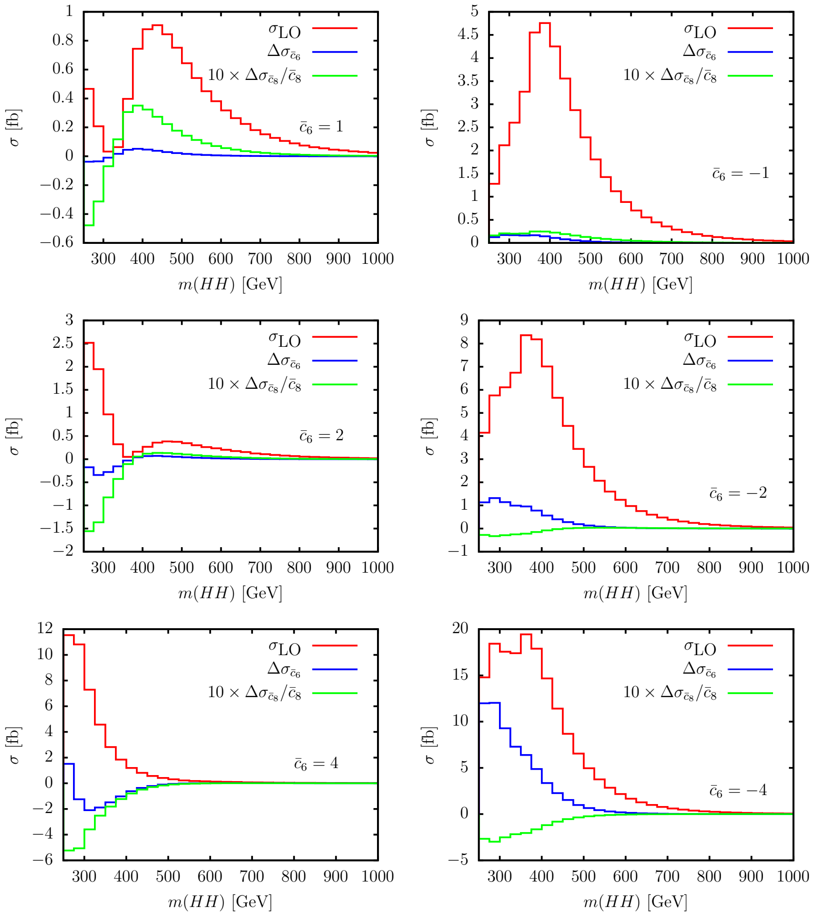

Figure 3.22: The $m(HH)$ distribution of different contributions (σ_{LO}, $\Delta\sigma_{\bar{c}_6}$, $\Delta\sigma_{\bar{c}_8}/\bar{c}_8$) at 14 TeV hadron collider for different $\bar{c}_6$ values.

in our analysis we assume that $\bar{c}_6$ and $\bar{c}_8$ effects factorise QCD corrections, and we compute the effects of selection cuts by adding the Higgs boson decays at the parton level. Therefore, we also assume that parton showering, hadronisation, and detector effects factorise the effect of selections cuts.

We perform a χ^2 fit on the $m(HH)$ distribution in the six bins, to set limits on $\bar{c}_6$ and $\bar{c}_8$. For simplicity, we only include statistical uncertainties. The impacts of theoretical uncertainties and experimental systematic uncertainties are expected to be much smaller than statistical uncertainties [22, 102], and thus they would not lead to significant differences in general; some caveats are present for the 100TeV case and we will discuss them afterwards. On the other hand, we have found that assuming $\bar{c}_6$ and $\bar{c}_8$ effects as flat within each of the six bins of the reconstructed $m(HH)$ distributions can strongly distort the results. Indeed in each $m(HH)$ bin, $\bar{c}_6$ and $\bar{c}_8$ effects are not flat, and selection cuts have an impact not only on the total number of events observed but also on the ratio $\sigma^{\rm pheno}_{\rm NLO}/\sigma^{\rm SM}_{\rm LO}$.

We consider two different scenarios for setting bounds on Higgs self-couplings:

1. Scenario 1: Well-behaved EFT ($\kappa_3 \neq 1, \kappa_4 \sim 6\kappa_3 - 1$). The contribution from $\bar{c}_8$ is suppressed comparing to the one from $\bar{c}_6$ under this scenario, hence we can safely set $\bar{c}_8 = 0$. We do not only assume $\bar{c}_6 \sim 0$, *i.e.* the SM-like configuration, but also allow for large BSM effects ($|\bar{c}_6| \neq 0$).
2. Scenario 2: Generation parametrisation allowing for $\kappa \neq 1$ and $\kappa_4 \neq 6\kappa_3 - 1$. In this scenario effects from $\bar{c}_8$ are not negligible and therefore we consider $\bar{c}_8 \neq 0$. Also in this case we consider both SM configuration and large BSM effects.

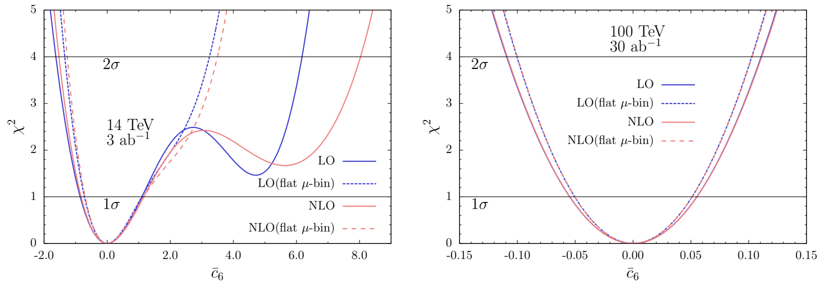

Figure 3.23: χ^2 as a function of $\bar{c}_6$ when $\bar{c}_8 = 0$ at 14 TeV(left) and 100 TeV(right).

In Fig. 3.23, we show the χ^2 as a function on $\bar{c}_6$ under scenario 1, where $\bar{c}_8 = 0$. The results using $\sigma^{\rm pheno}_{\rm NLO}$ or $\sigma_{\rm LO}$ in the fit. Furthermore, we also show the case that assumping for each $m(HH)$-bin the impact of $\bar{c}_6$ effects can be evaluated via the ratio $\sigma/\sigma^{\rm SM}_{\rm LO}$ without taking into account the selection cuts on the $b\bar{b}\gamma\gamma$ final state, where σ can be either $\sigma^{\rm pheno}_{\rm NLO}$ or $\sigma_{\rm LO}$. We remark that both in the “flat μ-bin” case and normal cases, selection cuts are taken into account for the SM signal; “flat μ-bin” concerns only the modelling of $\bar{c}_6$ and $\bar{c}_8$ effects for the $m(HH)$-binning in the fit. As we can see in Fig. 3.23, NLO effects are relevant only for large values of $\bar{c}_6$. By contrast, the “flat μ-bin” assumption strongly affects the χ^2 profile, especially in the region $\bar{c}_6 > 0$. In detail, we can see that under this assumption the 2σ bounds at 14 TeV would be artificially improved. This effect is due to the fact that for $\bar{c}_6 \gtrsim 2$ the bulk of events is in the first bin of the $m(HH)$ distribution, but the selection cuts yields very low efficiency in this region.

Taking into account the selection cuts in our analysis, we find the following 2σ constraints:

$$-0.5 < \kappa_3 = 1 + \bar{c}_6 < 8 \qquad \text{at 14 TeV with 3 ab}^{-1}\,, \tag{3.64}$$

$$0.9 < \kappa_3 = 1 + \bar{c}_6 < 1.1 \qquad \text{at 100 TeV with 30 ab}^{-1}\,. \tag{3.65}$$

We note that our results at 14 TeV are consistent with the ATLAS projections for the HL-LHC [103].

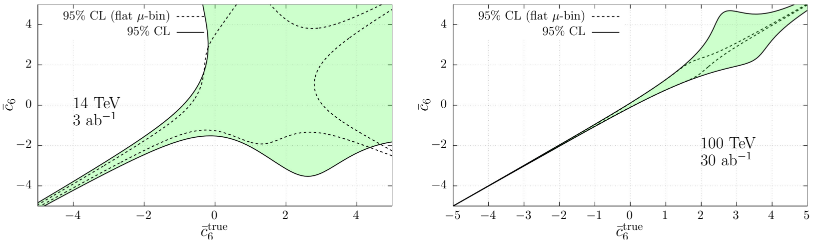

Figure 3.24: 2σ bounds on $\bar{c}_6$ as functions of $\bar{c}^{\text{true}}$ for 14 TeV(left) and 100 TeV(right) are shown.

Next we consider the case where $\bar{c}_6^{\text{true}}$ can be different from zero. In Fig. 3.24 we show 2σ bounds on $\bar{c}_6$ as functions of $\bar{c}_6^{\text{true}}$ at 14 TeV and 100 TeV. We found that if $\bar{c}_6^{\text{true}}$ is negative, bounds can sizeably stronger. At 100 TeV hadron collider, subpercent precision can be reached in the region $\bar{c}_6^{\text{true}} \lesssim -1$. This should be interpreted as indication that high precision may be reached in this scenario, but also theory and systematic uncertainties have to be taken into account. On the other hand, the bounds in the case that $\bar{c}_6^{\text{true}} > 0$ is much weaker, especially when $\bar{c}_6^{\rm true} \sim 3$. This is due to that the cross section reaches its minimum in that region.

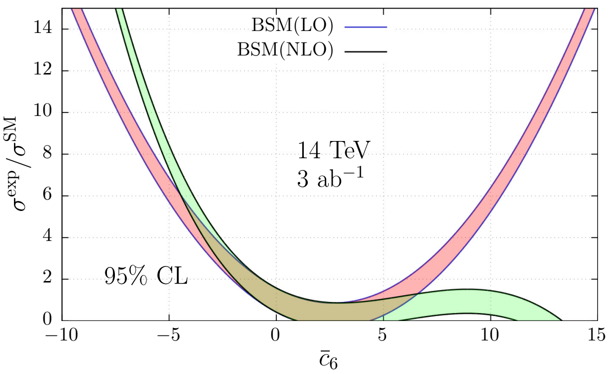

Figure 3.25

In this context we want also to stress an important point that has been somehow overlooked in both theory and experimental studies on κ_3-determination. In Fig. 3.25 we plot the 2σ constraints that can be obtained on $\bar{c}_6$ by varying of $\sigma^{\rm exp}/\sigma^{\rm SM}$, where $\sigma^{\rm exp}$ is the measured value and $\sigma^{\rm SM}$ is the SM prediction. We derive the constraints using two different approximations: $\sigma_{\rm NLO}^{\rm pheno}$ and $\sigma_{\rm LO}$. As can be seen, for $|\bar{c}_6| \gtrsim 5$, where perturbativity is violated, the constraints on $\bar{c}_6$ strongly depend on the choice between $\sigma_{\rm NLO}^{\rm pheno}$ and $\sigma_{\rm LO}$. When data are fitted with $\sigma_{\rm LO}$ predictions, $\bar{c}_6$ or equivalently κ_3 is a parameter of ignorance that only for $|\kappa_3 - 1| = |\bar{c}_6| \lesssim 5$ coincides to the quantity one is interested in. Outside this range, $\bar{c}_6$(or κ_3) is only suggesting how far from the SM predictions is the experimental result. The usage of $\sigma_{\rm NLO}^{\rm pheno}$ or any higher-order corrections in the place of $\sigma_{\rm LO}$ is not improving this situation, since the regime is not perturbative for $|\bar{c}_6| \gtrsim 5$. In conclusion, one can set bounds outside the $|\kappa_3 - 1| = |\bar{c}_6| \lesssim 5$ range, but only within this region they properly refer to the quantities we are interested in and defined via parameters in the Lagrangian.

Now we discuss scenario 2, to obtain the expected constraints on $\bar{c}_6$ and $\bar{c}_8$(κ_3 and κ_4) at HL-LHC and 100 TeV future collider. Assuming $\bar{c}_6^{\rm true} = \bar{c}_8^{\rm true} = 0$, in Fig. 3.26 we plot the expected 1σ and 2σ bounds in the $(\bar{c}_6, \bar{c}_8)$ plane at

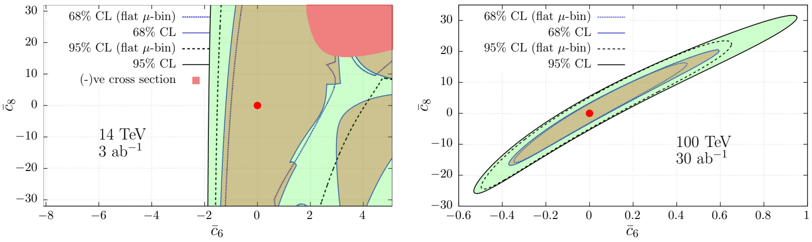

Figure 3.26: Expected 1σ and 2σ bounds in the $(\bar{c}_6, \bar{c}_8)$ plane at 14 TeV(left) and 100 TeV(right), assuming $\bar{c}_6^{\rm true} = \bar{c}_8^{\rm true} = 0$.

14 TeV and 100 TeV. The red area corresponds to the region where the cross section is negative. As already mentioned, no phenomenological study can be pefromed in this configuration. Similarly, for a given $(\bar{c}_6, \bar{c}_8)$, predictions for some bins can be negative, and we only use the bins where the cross section is positive in the χ^2 fit. In addition, for the 2σ results we also show the effect due to the “flat μ-bin” assumption. As can be seen in Fig. 3.26, at HL-LHC the presence of $\bar{c}_8$ contributions does not sizeably affect the constraints on $\bar{c}_6$. On the other hand, no sensible constraints on $\bar{c}_8$ can be obtained at the HL-LHC.

Results at a 100 TeV future collider are very different from at the HL-LHC. The bounds on $\bar{c}_6$ are affected by the presence of $\bar{c}_8$. In the right plot of Fig. 3.26, the bounds are $0.4 < \kappa_3 = 1 + \bar{c}_6 < 2$, which is much weaker than in Eq. (3.65). Although most of the perturbative region is not excluded, there is a clear direction in the contours of the constraints in the $(\bar{c}_6, \bar{c}_8)$ plane.

In Fig. 3.27 and 3.28, we show the expected 2σ bounds in the $(\bar{c}_6, \bar{c}_8)$ plane at 14 TeV HL-LHC and a 100 TeV hadron collider, assuming $\bar{c}_6^{\rm true} = \pm 1, \pm 2, \pm 4$ and $\bar{c}_8^{\rm true} = 0$. In general, at 14 TeV HL-LHC the limits on $\bar{c}_6$ are not sizeably affected by the presence of $\bar{c}_8$. On the other hand, sensible constraints on $\bar{c}_8$ cannot be obtained at the HL-LHC. At 100 TeV, as shown in Fig. 3.28, negative values of $\bar{c}_6^{\rm true}$ lead to strong constraints in the $(\bar{c}_6, \bar{c}_8$ plane. Furthermore, for large positive values of $\bar{c}_6^{\rm true}$, saying $\bar{c}_6^{\rm true} = 4$, the 1σ and 2σ regions are disconnected by the $(\bar{c}_6^{\rm true}, \bar{c}_8^{\rm true})$ point. Those regions are due to configurations where the first $m(HH)$ bin is predicted to be negative by $\sigma_{\rm NLO}^{\rm pheno}$. As

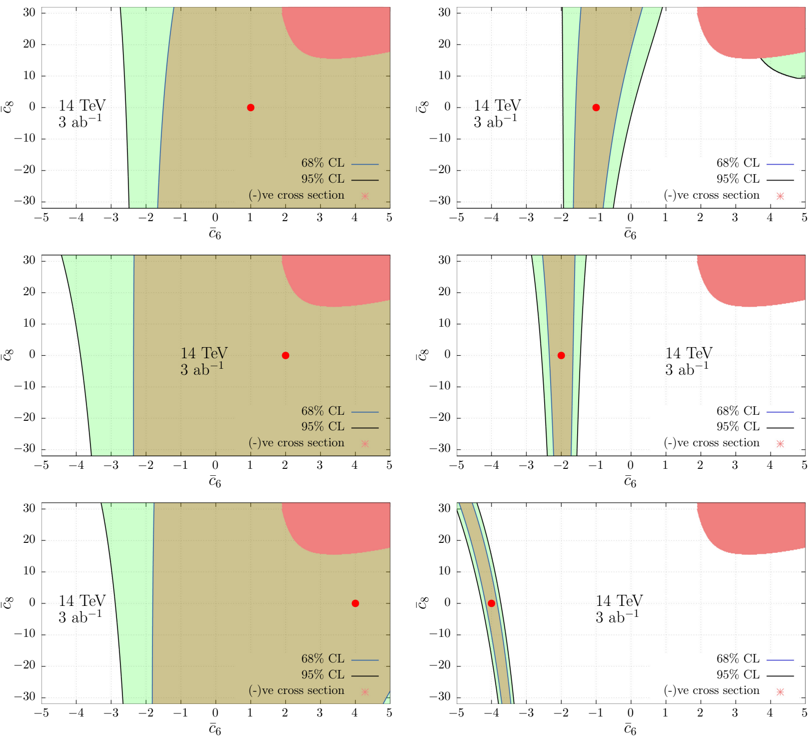

Figure 3.27: Expected 2σ constraints at 14 TeV HL-LHC are shown, assuming $\bar{c}_6^{\text{true}} = \pm 1, \pm 2, \pm 4$ and $\bar{c}_8^{\text{true}} = 0$(red dots).

explained, we remove its contribution to the χ^2, leading to a small χ^2, and thus such regions cannot be excluded. While we could eliminate these effects by artificially setting $\sigma_{\text{NLO}}^{\text{pheno}}$ to zero for negative values, we prefer to be conservative and exclude the contribution to χ^2 in these cases.

Last but least, in Fig. 3.29 we compare the constraints with the corresponding ones obtained from $b\bar{b}b\bar{b}\gamma\gamma$ signature in $pp \to HHH$ production [45, 79]. The bounds from triple Higgs production are derived under two different assumptions on b-tagging efficiency: optimistic (80%) and conservative (60%). We can see that the bounds from double Higgs are stronger than those from triple Higgs with the conservative assumption. Furthermore, they are complementary to those from triple Higgs with the optimistic assumption and their

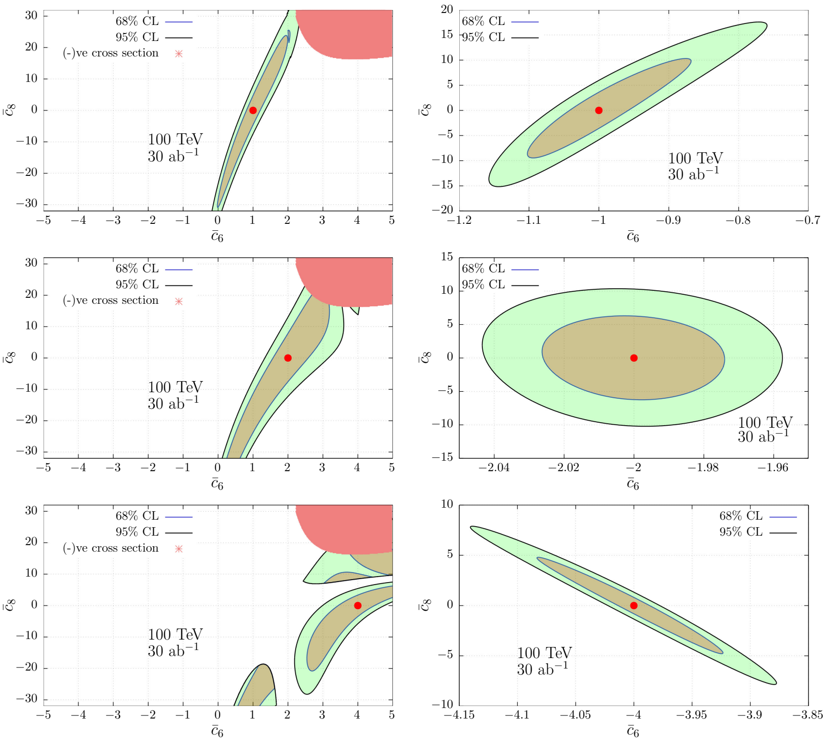

Figure 3.28: Expected 2σ constraints at a 100 TeV hadron collider are shown, assuming $\bar{c}_6^{\text{true}} = \pm 1, \pm 2, \pm 4$ and $\bar{c}_8^{\text{true}} = 0$(red dots).

combination can lead to stronger results. We also show the corresponding constraints in (κ_3, κ_4) plane, taking into account the perturbative bounds on $\bar{c}_6$ and $\bar{c}_8$.

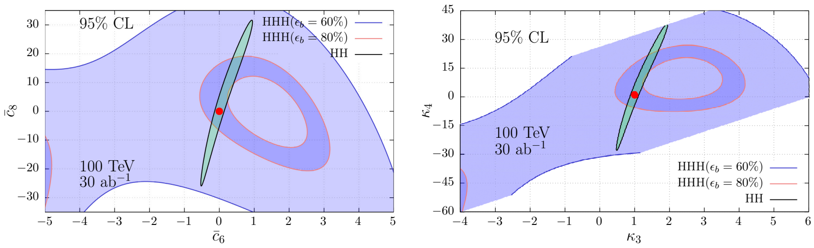

Figure 3.29: Comparison between expected 2σ-bounds between $HH(b\bar{b}\gamma\gamma)$ and $HHH(b\bar{b}b\bar{b}\gamma\gamma)$ at 100 TeV in the $(\bar{c}_6, \bar{c}_8)$ plane(left) and (κ_3, κ_4)(right) plane.

4 The Higgs boson self-couplings at future electron-positron colliders

In contrast to hadron collider, e^+e^- colliders provide clean environments for experimental measurements. Therefore, it is interesting to study the reach on constraining the Higgs boson self-couplings at future e^+e^- colliders.

Since the mass of electrons is tiny, the coupling between the Higgs boson and electrons is negligible. As a result, the dominating production modes of single and multi-Higgs boson are those obtained through the interaction with other heavy particles. In Fig. 4.1 we show the cross section for various production mechanism of single and double Higgs production as a function of center of mass energy. In the low energy region, Z boson associated production modes ($e^+e^- \to ZH^n$) dominate. As the energy increases, W boson fusion (WBF) production ($e^+e^- \to \nu_e\bar{\nu}_e H^n$) production increases, and surpass Z boson associated production. In addition, Higgs boson can also be produced accompany top quark pair ($e^+e^- \to t\bar{t}H^n$, through Z boson fusion (ZBF)($e^+e^- \to e^+e^-H^n$), through loop induced via photon fusion ($\gamma\gamma \to H^n$) [105], or through loop-induced production via e^+e^- annihilation ($e^+e^- \to H^n$).[1] However, these processes have much smaller cross sections than WBF or ZH^n production modes, and thus we do not consider them in our analysis. Indeed part of them have been considered in ref. [106] and their impact has been indeed found to be negligible.

As summarised in Tab. 4.1, for triple Higgs production both κ_3 and κ_4 enter at the Born level, and hence we only consider LO contributions. On the

---

[1] In the limit that electron is massless only multi-Higgs boson can be produced in this way.

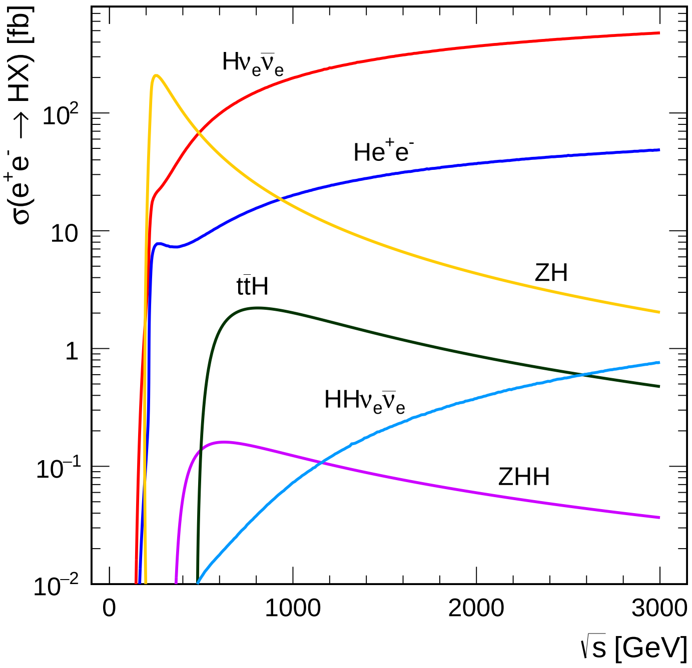

Figure 4.1: The cross section for single and double Higgs production at e^+e^- colliders are shown. Figure from Ref. [104]

Process	λ_3	λ_4
ZH, $\nu_e\bar{\nu}_eH$ (WBF)	one-loop	two-loop
ZHH, $\nu_e\bar{\nu}_eHH$ (WBF)	tree	one-loop
$ZHHH$, $\nu_e\bar{\nu}_eHHH$ (WBF)	tree	tree

Table 4.1: Processes considered and the order at which the λ_3 and λ_4 dependence appears. We do not calculate two-loop effects, but we do calculate one-loop effects for both single and double Higgs production.

other hand, for both single and double Higgs production we include also one-loop corrections. This enable us to constrain $\bar{c}_6$ ($\bar{c}_8$) indirectly through single (double) Higgs production, respectively. Furthermore, we expect complementary information from ZH^n and WBF, when the different collider energies of the possible future e^+e^- colliders are considered. While the cross section of

ZH^n is maximal for energies slightly larger than its production threshold, the WBF cross section grows with the energy. In addition, based on results in refs. [54, 56, 57, 106, 107], in ZH^n production we expect a strong dependence of the Higgs self-coupling effects from loop corrections, with larger effects at lower energies. On the contrary, in WBF this energy-dependence is expected to be much smaller.

It important to note that ZH^n and WBF cross sections, and in turn their sensitivity on $\bar{c}_6$ and $\bar{c}_8$, depend on beam polarisations, which can be tuned at linear colliders.[2] First of all, WBF contributes only via the LR polarisations(left-handed e^-, right-handed e^+), since W-boson couples only to the left-chirality fermions. By contrast, the ZH^n processes can also originate from RL polarisations (right-handed e^-, left-handed e^+)). In fact, results for RL polarisations can be easily obtained from those with LR via the relation

$$\sigma_{RL}(ZH^n) = \sigma_{LR}(ZH^n)\left(\frac{2\sin^2\theta_W}{1-2\sin^2\theta_W}\right)^2 \approx 0.65\sigma_{LR}\,, \tag{4.1}$$

In all our calculations we use following input parameters [109]

$$G_\mu = 1.166\,378\,7\times 10^{-5}\ \text{GeV}^{-2}\,, \quad m_W = \ 80.385\ \text{GeV}\,, \tag{4.2}$$
$$m_Z = 91.1876\ \text{GeV}, \quad m_H = 125\ \text{GeV}, \quad m_t = 173.21\ \text{GeV}\,. \tag{4.3}$$

We assume that both $\bar{c}_6$ and $\bar{c}_8$ are measured at the scale $\mu_{\text{EFT}} = 2m_H$, which we will also use as $\overline{\text{MS}}$ renormalisation scale for $\bar{c}_6$ in the double Higgs computation. We note that with $Z \to \nu_e\bar{\nu}_e$ decays the ZH^n production mode would yields the same final states as the WBF production modes. We do not consider the former as part of the WBF contribution in our calculation. The classification of WBF and ZH^n production modes can be achieved by exploiting lepton flavour universality. In detail, the process $e^+e^- \to \nu_e\bar{\nu}_e H^n$ receives two kinds of contribution at the amplitude level: one is identical to the process $e^+\mu^- \to \bar{\nu}_e\nu_\mu H^n$; the other is identical to the process $e^+e^- \to \bar{\nu}_\mu\nu_\mu H^n$. Only the former is considered to be the WBF contribution, and we only include such WBF contribution in our calculation. We note that due to the pres-

---

[2] Due to the Sokolov Ternov effect [108], the tuning of beam polarisations is much more difficult in circular colliders.

ence of an on-shell Z boson, ZH^n-type contribution has significantly different kinematics comparing to WBF contribution, and thus the interference between them are negligible.

4.1 Calculation

4.1.1 Single Higgs production

In this section we briefly (re)-describe the calculation of loop-induced effects from $\bar{c}_6(\kappa_3)$ in ZH and single-Higgs WBF production at e^+e^- colliders (representative diagrams are shown in Fig. 4.2). We introduce the notation that will be generalised to the case of double Higgs and triple Higgs production and we show how it is related to the previous calculations [54, 56, 106, 107].

For both WBF H and ZH production channels no Higgs self-coupling contributes at the tree level. On the other hand, one-loop corrections depends on the trilinear Higgs self-coupling, but not on the quartic. Thus, while the LO cross section $\sigma_{\rm LO}(H)$ is only of SM origin, NLO predictions includes also effects from $\bar{c}_6$:

$$\sigma_{\rm NLO}(H) = \sigma_{\rm LO}(H) + \sigma_{1-\rm loop}(H)\,, \tag{4.4}$$

$$\sigma_{\rm LO}(H) = \sigma_{\rm LO}^{\rm SM}(H)\,, \tag{4.5}$$

$$\sigma_{1-\rm loop}(H) = \sigma_0 + \sigma_1\bar{c}_6 + \sigma_2\bar{c}_6^2\,, \tag{4.6}$$

where $\sigma_{1-\rm loop}$ involves one-loop corrections of both SM origin and induced by c_6. The quantity σ_0 includes the NLO EW corrections from the SM, σ_1 represents the leading contribution in the EFT expansion (order $(v/\Lambda)^2$), while σ_2 is of order $(v/\Lambda)^4$, also arising from one-loop corrections.[3] Note that within our choice of operators there is no contribution proportional to $\bar{c}_8$ or any other c_{2n} coefficient in this expansion, meaning that eq. (4.6) is actually exact; no other terms can enter at all even for higher orders in the (v/Λ) expansion. Furthermore, we remind that, at variance with the case of double Higgs production, in single Higgs production at one-loop the anomalous coupling approach (κ_3) is fully equivalent to the calculation in the EFT ($\bar{c}_6$).

---

[3] Whenever we refer to NLO EW corrections of SM origin, those include also real emissions of photons. On the contrary, one-loop effects induced by c_{2n} are infrared safe and involve just virtual corrections. Needless to say, at one-loop, NLO QCD corrections are vanishing for the processes considered here.

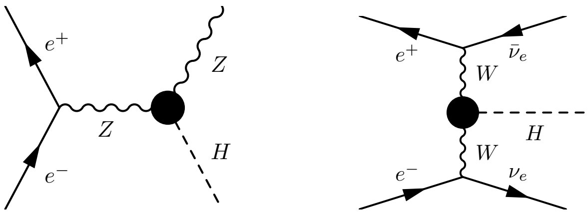

Figure 4.2: Feynman diagrams for single Higgs production. The black blob corresponds to the one-loop HVV form factors.

Since our main focus is not the precise determination of $\bar{c}_6$, but the study of its impact via its leading contributions. As discussed in detail in section 3.1, SM NLO EW corrections have a tiny impact on the extraction of the value of $\bar{c}_6$ and do not affect the accuracy of the determination of $\bar{c}_6$. Therefore we ignore the SM NLO EW corrections [110, 111], and consider $\bar{c}_6$ effects at one loop via the following approximation

$$\sigma_{\rm NLO}^{\rm pheno}(H) = \sigma_{\rm LO} + \sigma_1 \bar{c}_6 + \sigma_2 \bar{c}_6^2 \,. \tag{4.7}$$

With this approximation, the sensitivity to the trilinear coupling can be expressed via the ratio

$$\delta\sigma(H) \equiv \frac{\sigma_{\rm NLO}^{\rm pheno} - \sigma_{\rm LO}}{\sigma_{\rm LO}} = \frac{\sigma_1 \bar{c}_6 + \sigma_2 \bar{c}_6^2}{\sigma_{\rm LO}} = (\kappa_3 - 1) C_1 + (\kappa_3^2 - 1) C_2 \,, \tag{4.8}$$

$$C_2 = \delta Z_H^{\rm SM,\lambda} \,, \tag{4.9}$$

where we have expressed the $\sigma_i/\sigma_{\rm LO}$ ratios directly[4] using the symbols C_1 and C_2 introduced in ref. [56]. C_1 denotes the one-loop virtual contribution involving one triple Higgs vertex, while C_2 originates from the Higgs wave-function renormalisation constant (see eqs. (2.15),(2.27) and (2.31)), which is the only source of $\bar{c}_6^2$ and thus κ_3^2 dependence at one loop level. Both C_1 and C_2 are independently UV-finite and, for simplicity, we choose not to resum higher-orders contributions to the wave function, at variance with ref. [56] and

---

[4] Note that $\kappa_3^2 - 1 = (\kappa_3 - 1)^2 + 2(\kappa_3 - 1)$, so $\sigma_2 = C_2 \sigma_{\rm LO}$ and $\sigma_1 = (C_1 + 2C_2)\sigma_{\rm LO}$

section 3.1. Indeed, given the results already presented in ref. [54], we expect to bound κ_3 close to the SM ($\kappa_3 = 1$) and in this scenario such a resummation would not make a noticeable difference anyway. Moreover, even considering κ_3 in the range $|\kappa_3| < 6$ from ref. [92], the difference between the formula in eq. (4.8) and including the resummed higher-order contributions to Z_H is below 1% (see also ref. [107]). Considering C_2 in eq. (4.9), the difference w.r.t. the definition in ref. [56] is only due to this choice, however, in the limit $\bar{c}_6 \to 0$ ($\kappa_3 \to 1$) the two different definitions are equivalent as can be seen from the value of C_2:

$$C_2 = \delta Z_H^{\mathrm{SM},\lambda} \equiv -\frac{9}{16}\frac{G_\mu m_H^2}{\sqrt{2}\pi^2}\left(\frac{2\pi}{3\sqrt{3}} - 1\right) \approx -0.00154\,. \tag{4.10}$$

Moreover, in the limit $\bar{c}_6 \to 0$, a linear expansion of eq. (4.8) for ZH would lead to the result in ref. [54]. As explained in ref. [56] for hadronic processes, C_1 parametrises contributions that are process and kinematic dependent.

In Fig. 4.3, we show σ_{LO} (left plot) and C_1 (right plot) for ZH (red) and WBF (green) production as function of the energy of the collider $\sqrt{\hat{s}}$. As expected, while C_1 strongly depends on $\sqrt{\hat{s}}$ for ZH, it does very mildly for WBF H. In particular, for ZH, when increasing the energy, C_1 decreases at the beginning, then changes its sign around $\sqrt{\hat{s}} = 550$ GeV and remains small. On the other hand, the total cross section for ZH production peaks at around $\sqrt{\hat{s}} = 240$ GeV and decreases as $\sqrt{\hat{s}}$ increases, while the cross section for WBF H production increases with $\sqrt{\hat{s}}$. Thus, while for the range $200 - 500$ GeV the ZH production is expected to be more sensitive than WBF on $\bar{c}_6$ (κ_3), at higher energies the situation is reversed. The information from collisions at different energies, or even at different colliders, increases the sensitivity on κ_3, as it has been discussed in ref. [106]. We will show analogous results in sec. 4.2. We have also looked at the differential distribution for the transverse momentum of the Higgs boson, but we have not seen any strong dependence on C_1. Hence, for single Higgs production at e^+e^- colliders differential distribution cannot increase the sensitivity on κ_3, at variance with the case of hadron colliders [56–58, 107] and of double-Higgs production [112].

The range of validity of this calculation in κ_3 and in turn $\bar{c}_6$ is mainly dictated by the effects from δZ_H^{NP}, as discussed in ref. [56], from which the bound $|\kappa_3| < 20$ can be also straightforwardly applied here. A more cautious and

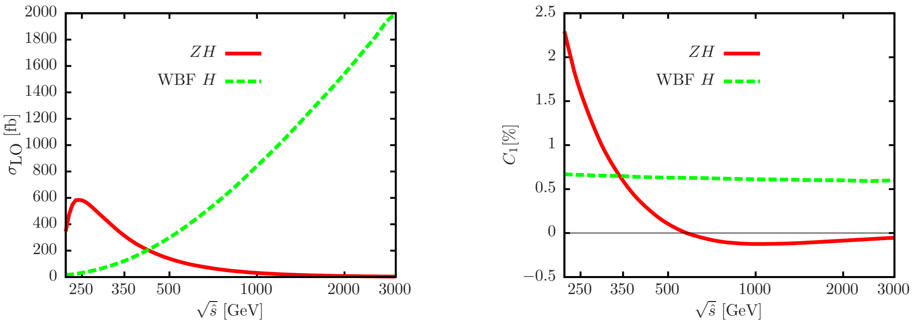

Figure 4.3: LO cross section (left) and C_1 (right) as function of the center of mass energy $\sqrt{\hat{s}}$ for $P(e^-, e^+) = (-1.0, 1.0)$.

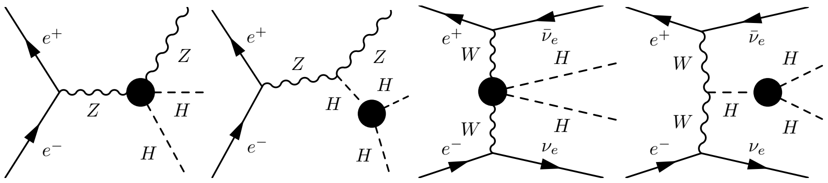

Figure 4.4: Representative Feynman diagrams for double Higgs production. The black blobs correspond to the one-loop $HHVV$ and HHH form factors given in App. A.

conservative condition can be derived by requiring perturbative unitarity for the $HH \to HH$ scattering amplitude and/or perturbativity for the loop corrections to the HHH vertex in any kinematic configuration. This bound has been derived in ref. [92] and leads to the requirement $|\kappa_3| < 6$, independently from the value of κ_4. However, the kinematic configuration leading to this bound are those involving two Higgses on-shell and the virtuality of the third Higgs close to $2m_H$, which is not relevant for the trilinear interaction entering in single-Higgs production. We independently re-investigated this bound on $\bar{c}_6$ (and analogous ones on $\bar{c}_8$) in Appendix B, where its derivation is discussed in detail.

4.1.2 Double Higgs production

We now consider double Higgs production. The cross sections for both the Z-associated production($e^+e^-{\to}ZHH$) and via WBF ($e^+e^-{\to}\nu_e\bar{\nu}_eHH$) depend on the cubic Higgs self-coupling at the tree level(see diagrams in Fig. 4.4). Starting from one-loop level, both processes depends on both the cubic and quartic Higgs self-couplings. Similar to $gg \to HH$ at hadron collider, at LO the amplitude depends on $\bar{c}_6$ linearly, *i.e.*

$$\mathcal{M}^{\text{tree}} = \mathcal{M}_0^{\text{tree}} + \mathcal{M}_1^{\text{tree}}\bar{c}_6\,, \tag{4.11}$$

at one-loop level, the amplitude receives contribution from $\bar{c}_6, \bar{c}_8$, and $\bar{c}_{10}$, which can be written as

$$\begin{aligned}\mathcal{M}^{1\text{L}} =& \mathcal{M}_{00}^{1\text{L}} + \mathcal{M}_{10}^{1\text{L}}\bar{c}_6 \\ &+ \mathcal{M}_{20}^{1\text{L}}\bar{c}_6^2 + \mathcal{M}_{30}^{1\text{L}}\bar{c}_6^3 \\ &+ \mathcal{M}_{01}^{1\text{L}}\bar{c}_8 + \mathcal{M}_{11}^{1\text{L}}\bar{c}_6\bar{c}_8 \\ &+ \mathcal{M}_{001}^{1\text{L}}\bar{c}_{10}\,.\end{aligned} \tag{4.12}$$

As discussed in Section 3.3, the contribution from $\bar{c}_{10}$ can be treated as a shift on $\bar{c}_6$, and hence we do not include it in our calculation. The terms $\mathcal{M}_{00}^{1\text{L}}$ and $\mathcal{M}_{10}^{1\text{L}}$ are corresponding to $\mathcal{O}(\alpha)$ corrections of $\mathcal{M}_0^{\text{tree}}$ and $\mathcal{M}_1^{\text{tree}}$, and thus they are IR-divergent, and corresponding real emission contribution should be added together at the cross section level, to obtain IR-finite results. As our target is to study feasibility of constraining $\bar{c}_6$ and $\bar{c}_8$ through those processes, rather than precise prediction of the processes nor determination of $\bar{c}_6$ and $\bar{c}_8$, we neglect both $\mathcal{M}_{00}^{1\text{L}}$ and $\mathcal{M}_{10}^{1\text{L}}$, similarly to the case of $gg \to HH$ in Section 3.3. Those terms are required for extracting $\bar{c}_6$ and $\bar{c}_8$ from experimental data, but they should have tiny impact on the sensitivity of $\bar{c}_6$ and $\bar{c}_8$. The other terms in Eq. (4.12) are IR-finite, and we use the following approximation for the amplitude

$$\mathcal{M}^{1\text{L,pheno}} = \mathcal{M}_{\bar{c}_6}^{1\text{L}} + \mathcal{M}_{\bar{c}_8}^{1\text{L}} \tag{4.13}$$

$$\mathcal{M}_{\bar{c}_6}^{1\text{L}} = \mathcal{M}_{20}^{1\text{L}}\bar{c}_6^2 + \mathcal{M}_{30}^{1\text{L}}\bar{c}_6^3 \tag{4.14}$$

$$\mathcal{M}_{\bar{c}_8}^{1\text{L}} = \mathcal{M}_{01}^{1\text{L}}\bar{c}_8 + \mathcal{M}_{11}^{1\text{L}}\bar{c}_6\bar{c}_8\,. \tag{4.15}$$

Using such approximation for the amplitude, we get the following approximation for the cross section at NLO

$$\sigma_{\rm NLO}^{\rm pheno} = \sigma_{\rm LO} + \Delta\sigma_{\bar{c}_6} + \Delta\sigma_{\bar{c}_8} \tag{4.16}$$
$$\Delta\sigma_{\bar{c}_6} = \bar{c}_6^3(\sigma_{30} + \sigma_{40}\bar{c}_6) \tag{4.17}$$
$$\Delta\sigma_{\bar{c}_8} = \bar{c}_8(\sigma_{01} + \sigma_{11}\bar{c}_6 + \sigma_{21}\bar{c}_6^2)\,, \tag{4.18}$$

where $\Delta\sigma_{\bar{c}_6}$ captures the leading corrections induced by $\bar{c}_6$ on top of $\bar{c}_6$, and $\Delta\sigma_{\bar{c}_8}$ includes all $\bar{c}_8$ dependent contributions. Different from in Section 3.3, we do not include the $\tilde{\sigma}_{20}$ term, since we found that its effects on sensitivity of $\bar{c}_6$ and $\bar{c}_8$ are tiny. The amplitudes enter in are calculated based on the form factor methods, which is similar to the implementation of single Higgs. In particular, we have

$$\mathcal{M}_{20}^{\rm 1L} = \mathcal{M}_{20}^{\rm 1L,\mathcal{F}} + \mathcal{M}_{20}^{\rm 1L,\mathcal{W}} \tag{4.19}$$
$$\mathcal{M}_{30}^{\rm 1L} = \mathcal{M}_{30}^{\rm 1L,\mathcal{F}} + \mathcal{M}_{20}^{\rm 1L,\mathcal{W}} \tag{4.20}$$
$$\mathcal{M}_{01}^{\rm 1L} = \mathcal{M}_{01}^{\rm 1L,\mathcal{F}} \tag{4.21}$$
$$\mathcal{M}_{11}^{\rm 1L} = \mathcal{M}_{11}^{\rm 1L,\mathcal{F}}\,, \tag{4.22}$$

where $\mathcal{F}$ denotes the contribution that can be calculated from the form factors given in Appendix A. $\mathcal{W}$ denotes the Higgs wave-function contribution, which can be written as

$$\mathcal{M}_{20}^{\rm 1L,\mathcal{W}} = \delta Z_H^{{\rm SM},\lambda}\mathcal{M}_0^{\rm tree} + 2\delta Z_H^{{\rm SM},\lambda}\mathcal{M}_1^{\rm tree} \tag{4.23}$$
$$\mathcal{M}_{30}^{\rm 1L,\mathcal{W}} = \delta Z_H^{{\rm SM},\lambda}\mathcal{M}_1^{\rm tree}\,. \tag{4.24}$$

Note that by separating the wave-function contribution, it can be resummed as done in ref. [56]. However, considering $|\bar{c}_6| < 5$, resummation is not necessary given that $\bar{c}_6^2\delta Z_H^{{\rm SM},\lambda} < 4\%$.

We include contributions up to the order $(v/\Lambda)^6$ and therefore one-loop amplitudes entering $\sigma_{\rm NLO}^{\rm pheno}(HH)$ can be obtained by substituting the vertexes in the corresponding tree-level amplitudes. Indeed, we implemented them in a UFO [61] model file and performed the calculation within the MADGRAPH5_AMC@NLO [62] framework, as also done in Section 3.1. We cross-checked the results via FEYNARTS 3.9 [113] and FORMCALC 9.4 [63]. Loops

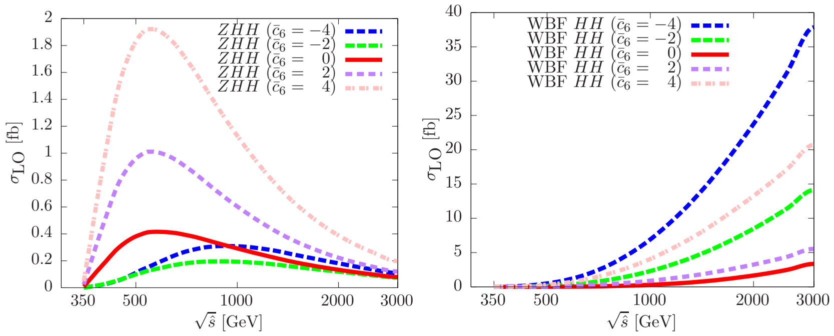

Figure 4.5: LO cross section of ZHH and WBF HH as function of $\sqrt{\hat{s}}$ for different values of $\bar{c}_6$. Results refer to $P(e^-, e^+) = (-1.0, 1.0)$.

integrals have been evaluated with LoopTools 2.13 [63] and QCDLoop 2.0.3 [114, 115].

First of all, in Fig. 4.5 we show the LO cross section $\sigma_{\rm LO}$ of ZHH (left) and WBF (right) production as function of $\sqrt{\hat{s}}$ for different values of $\bar{c}_6$. In ZHH production, the LO cross section peaks around $\sqrt{\hat{s}} = 500$ GeV, which is the optimal energy for measuring this processes, while WBF HH cross section grows with energy. As can be seen by comparing the left and right plot, the dependence on $\bar{c}_6$ is different in ZHH and WBF HH production. Especially, at variance with ZHH, WBF HH cross sections in general increase when $\bar{c}_6 \neq 0$. This feature is even more clear in the top-left plot of Fig. 4.6, where we show the dependence of $\sigma_{\rm LO}$ on $\bar{c}_6$ for the different phenomenologically relevant configurations that will be analysed in sec. 4.2, namely, ZHH at 500 GeV collisions and WBF HH at 1, 1.4 and 3 TeV collisions.

Using a similar layout, in Fig. 4.6 we display three other plots, which show the dependence of $\sigma_{\rm LO}$, $\Delta\sigma_{\bar{c}_6}(HH)$ and $\Delta\sigma_{\bar{c}_8}(HH)/\bar{c}_8$ on $\bar{c}_6$ for different processes and energies. Specifically, in the upper-right plot we show the case of ZHH at 500 GeV, while in the lower plots we show WBF HH at 1 TeV (left) and 3 TeV (right). In these three plots we display $\sigma_{\rm LO}$, which has also been shown in the top-left plot, as a black line and $\Delta\sigma_{\bar{c}_6}(HH)$ and $\Delta\sigma_{\bar{c}_8}(HH)/\bar{c}_8$

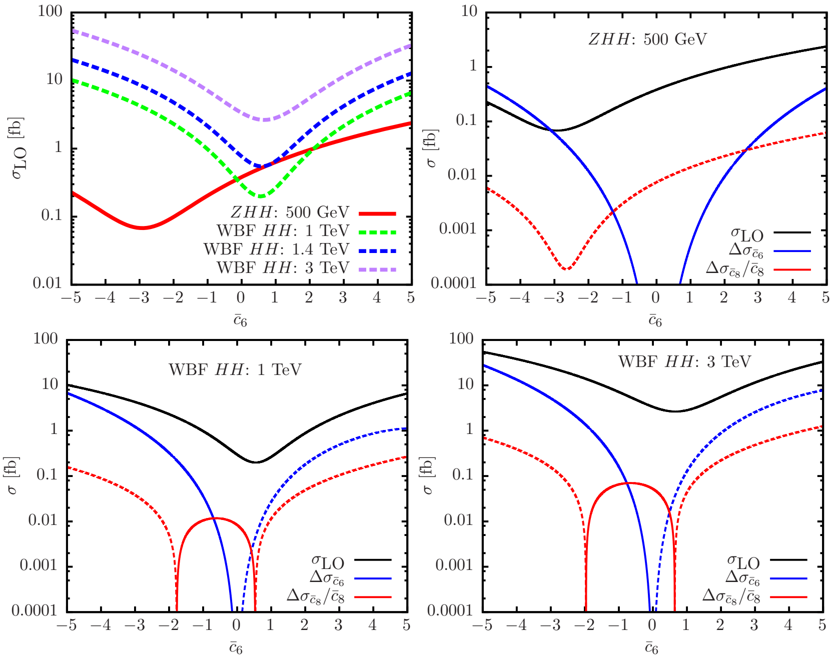

Figure 4.6: Top-left plot: $\bar{c}_6$ dependence of the LO cross section for ZHH and WBF HH at different energies. The three other plots show the $\bar{c}_6$ dependence of $\Delta\sigma_{\bar{c}_6}(HH)$, $\Delta\sigma_{\bar{c}_8}(HH)/\bar{c}_8$ and again $\sigma_{\rm LO}$ for ZHH production at 500 GeV (top-right), and WBF HH at 1000 GeV (bottom-left) and 1400 GeV (bottom-right).

as a blue and red line, respectively. Thus the blue line directly shows the $\bar{c}_8$-independent part of $\sigma_{\rm NLO}^{\rm pheno}$, while the red one corresponds to the coefficient in front of the $\bar{c}_8$-dependent part $\Delta\sigma_{\bar{c}_8}(HH)$, which in turn depends on $\bar{c}_6$. For both cases, a short-dashed line is used when $\Delta\sigma_{\bar{c}_6}(HH)$ or $\Delta\sigma_{\bar{c}_8}(HH)/\bar{c}_8$ are negative. From Fig. 4.6 we can see that not only for the LO prediction (top-left plot) but also for one-loop effects the $\bar{c}_6$ (as well $\bar{c}_8$) dependence is very different in ZHH (top-right plot) and WBF HH (lower plots) production. On the other hand, as can be seen in the lower plots, besides a global rescaling factor, WBF HH results are not strongly affected by the energy of e^+e^- collisions.[5]

---

[5] In the case of ZHH there are larger differences with the energy, but in our analysis we consider it only at 500 GeV.

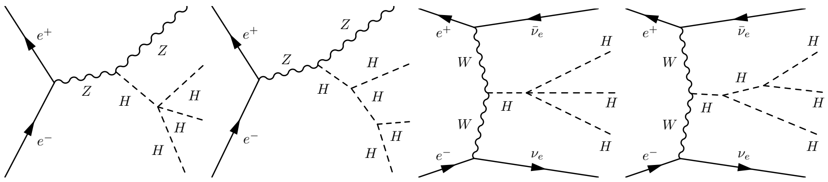

Figure 4.7: Representative tree-level Feynman diagrams for triple Higgs production.

In the case of ZHH production at 500 GeV, the minimum of the LO cross section is at $\bar{c}_6 \sim -3$, while for WBF HH it is at $\bar{c}_6 \sim 0.5$. This minimum is given by cancellations induced by the interference of diagrams featuring or not the HHH vertex. Such pattern of cancellations is different in the $\Delta\sigma_{\bar{c}_6}(HH)$ one-loop contribution, which in absolute value is instead minimal at $\bar{c}_6 = 0$ and very large at large values of $\bar{c}_6$. For this reason, *e.g.*, for $\bar{c}_6 < -3$ the $\Delta\sigma_{\bar{c}_6}(HH)$ one-loop contribution is larger than the LO cross section. This does not signal the breaking of the perturbative convergence, rather it is due to the large cancellations that are present in this region only in the LO cross section; as already said, the perturbative limits, which are derived in Appendix B, require $|\bar{c}_6| < 5$ and correspond to the range of the plot. In the case of WBF HH production $\Delta\sigma_{\bar{c}_6}(HH)$ is always smaller than σ_{LO}, being negative for $\bar{c}_6 > 0$ and positive for $\bar{c}_6 < 0$.

Regarding the $\Delta\sigma_{\bar{c}_8}(HH)$ contribution, which we display in the red lines normalised with $1/\bar{c}_8$, the effect is very different in ZHH and WBF HH production. In the case of ZHH production $\Delta\sigma_{\bar{c}_8}(HH)$ is always negative and the minimum in absolute value is very close to the minimum of the LO prediction. In the case of WBF HH production $\Delta\sigma_{\bar{c}_8}(HH)$ change sign at $\bar{c}_6 \sim -2$ and $\bar{c}_6 \sim 0.5$, being positive between these two values and negative outside them. In general, in absolute value, the ratio $\Delta\sigma_{\bar{c}_8}(HH)/\sigma_{\text{LO}}$ is always below $\bar{c}_8 \cdot 2\%$ value. Still, given the allowed perturbative range $|\bar{c}_8| < 31$ (see Appendix B), effects from large values of $\bar{c}_8$ can be in principle probed.

ratio over σ_{00}	σ_{10}	σ_{20}	σ_{30}	σ_{40}
500 GeV	$(2.2, -9.0)$	$(1.4, 8.5)$	$(0.3, 34)$	$(0.02, 19)$
1 TeV	$(2.2, -3.7)$	$(1.5, 16)$	$(0.2, 17)$	$(0.01, 6)$
1.4 TeV	$(2.2, -3.4)$	$(1.6, 16)$	$(0.2, 12)$	$(0.01, 3.8)$
3 TeV	$(2.2, -2.1)$	$(1.9, 7.6)$	$(0.2, 3.8)$	$(0.01, 1.0)$

ratio over σ_{00}	σ_{01}	σ_{11}	σ_{21}	σ_{02}
500 GeV	$(0.1, -4.0)$	$(0.1, -14)$	$(0.01, 16)$	$(0.002, 3.3)$
1 TeV	$(0.1, -1.5)$	$(0.2, 10)$	$(0.02, 7.1)$	$(0.006, 2.3)$
1.4 TeV	$(0.1, -1.0)$	$(0.2, 9.2)$	$(0.02, 5.2)$	$(0.009, 2.0)$
3 TeV	$(0.1, -0.3)$	$(0.3, 4.1)$	$(0.03, 1.6)$	$(0.02, 0.9)$

Table 4.2: σ_{ij}/σ_{00} ratios for ($ZHHH$, WBF HHH). σ_{ij} are defined in eq. (4.25).

4.1.3 Triple Higgs production

In triple Higgs production cubic and quartic self-couplings are present already at the tree level and therefore both the leading dependences on $\bar{c}_6$ and $\bar{c}_8$ are already present at LO (see diagrams in Fig. 4.7). Following the same notation used for double Higgs production, the cross section used for our phenomenological predictions can be written as

$$\sigma_{\rm LO}(HHH) = \sigma_{00} + \sum_{1\leq i+2j\leq 4} \sigma_{ij}\bar{c}_6^i\bar{c}_8^j\,, \tag{4.25}$$

where the σ_{00} term corresponds to the LO SM prediction. Similarly to the case of double Higgs production at one loop, terms up to the eighth power in the (v/Λ) expansion are present at the cross section level, although in this case only the fourth power is present at the amplitude level. The upper bounds on $\bar{c}_6$ and $\bar{c}_8$ mentioned in the previous section and discussed in Appendix B have to be considered also in this case. It is important to note that although for large values of $\bar{c}_6$ and $\bar{c}_8$ loop corrections may be sizeable, at variance with double Higgs production, $\bar{c}_6$ and $\bar{c}_8$ are both entering at LO. Thus, when limits on $\bar{c}_6$ and $\bar{c}_8$ are extracted, loop corrections may slightly affect them, but only for large $\bar{c}_6$ and $\bar{c}_8$ values. In Tab. 4.2 we give all the σ_{ij}/σ_{00} ratios, so that the size of all the relative effects from the different NP contributions can be easily

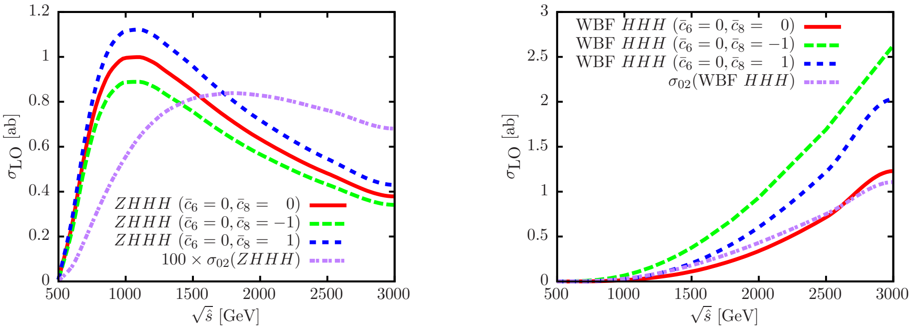

Figure 4.8: LO cross section of $ZHHH$ and WBF HHH as function of $\sqrt{\hat{s}}$ for representative values of $\bar{c}_6$ and $\bar{c}_8$. The σ_{02} component is also explicitly shown. Results refer to $P(e^-, e^+) = (-1.0, 1.0)$.

inferred.[6] In Fig. 4.8, we show $\sigma_{\rm LO}$ at different energies for representative values of $\bar{c}_6$ and $\bar{c}_8$, including the SM case ($\bar{c}_6 = 0, \bar{c}_8 = 0$) where $\sigma_{\rm LO} = \sigma_{00}$. There, we also explicitly show the value of the σ_{02} component, which factorises the $(\bar{c}_8)^2$ dependence. We can see that for $ZHHH$ production (left) the sensitivity to $\bar{c}_8$ is rather weak. The σ_{02} component is just around 1% of σ_{00}, which means that even for large values of $\bar{c}_8$ the total cross section would not be large enough to be measurable at the future colliders considered in this study (see discussion in sec. 4.2). On the other hand, the total cross section of WBF HHH increases with the energy, as for single and double Higgs production. Especially, the σ_{02} component is much larger; it is of the same order of the SM σ_{00} component. As an example, assuming $\bar{c}_8 = 1 (\bar{c}_8 = -1)$ and $\bar{c}_6 = 0$, $\sigma_{\rm LO}$ at 3 TeV is 1.7 (2.4) times larger than σ_{00}. For large $\bar{c}_8$ values, $\sigma_{\rm LO} \approx \bar{c}_8^2 \sigma_{02} \approx \bar{c}_8^2 \sigma_{00}$. As can be seen in Tab. 4.2, WBF is also very sensitive on $\bar{c}_6$; for large values of $\bar{c}_6$ indeed $\sigma_{\rm LO} \approx \bar{c}_6^4 \sigma_{40} \approx \bar{c}_6^4 \sigma_{00}$. All these effects are even larger at lower energies.

---

[6] There are large cancellations among the different contributions; more digits than those shown here have to be taken into account in order to obtain a reliable result.

	$\sqrt{\hat{s}}$ [GeV]	$P(e^-, e^+)$	Luminosity [ab^{-1}]	Relevant final states
CEPC	250	(0.0,0.0)	5.0	ZH, WBF H
FCC-ee	240	(0.0,0.0)	10.0	ZH, WBF H
	350	(0.0,0.0)	2.6	ZH, WBF H
ILC	250	(-0.8,0.3)	2.0	ZH, WBF H
	500	(-0.8,0.3)	4.0	ZHH, WBF H
	1000	(-0.8,0.2)	2.0	$ZHHH$, WBF $H(H(H))$
CLIC	350	(-0.8,0.0)	0.5	ZH, WBF H
	1400	(-0.8,0.0)	1.5	$ZHHH$, WBF $H(H(H))$
	3000	(-0.8,0.0)	2.0	WBF $H(H(H))$

Table 4.3: The different operation modes for e^+e^- colliders considered here.

4.2 Bounds on the Higgs self-couplings

In this section we study how the $\bar{c}_6$ and $\bar{c}_8$ parameters can be constrained at future lepton colliders via the analysis of single, double, and triple Higgs production. We consider four future e^+e^- colliders, CEPC [116], FCC-ee [117], ILC [118], and CLIC [104,119], with different operations modes[7] that are summarised in Tab. 4.3. In the following, we will refer to the different scenarios as "collider-$\sqrt{\hat{s}}$" like, *e.g.*, CLIC-3000. Although higher integrated luminosities can be attained at the CEPC and FCC-ee, energies as high as at the ILC and CLIC cannot be reached, since they are circular colliders. As a result, only single Higgs production can be measured at the CEPC and FCC-ee, and therefore only indirect constraints via loop corrections can be set on $\bar{c}_6$. Instead, at the ILC and CLIC double Higgs production can be measured. With this process, both $\bar{c}_6$ and $\bar{c}_8$ can be constrained, the former via the direct dependence at the Born level and the latter via the indirect dependence through loop corrections. Moreover, even triple Higgs production is kinematically allowed at the ILC and CLIC, allowing to set direct constraints on $\bar{c}_8$.

In our analysis we consider the following two scenarios[8]:

---

[7] At the ILC also an operation mode at $\sqrt{\hat{s}} \sim 350$ GeV is expected, but studies mainly focused on the scan of the $t\bar{t}$ production threshold, ignoring Higgs physics. At CLIC also a slightly different scenario at 380 GeV instead of 350 GeV may be possible.

[8] One may be tempted to explore the regime $\bar{c}_6 = 0$ and $\bar{c}_8 \neq 0$, too. However, this condition is neither motivated by an EFT expansion nor protected by any symmetry. As can be seen from eq. (2.30), a large $\bar{c}_8$ automatically generates a $\bar{c}_6$ component via loop corrections.

	$\sqrt{\hat{s}}$ [GeV]	process	ϵ [%]	C_1 [%]	$\bar{c}_6(\pm 1\sigma)$	$\bar{c}_6(\pm 2\sigma)$
CEPC	250	ZH	0.51	1.6	$(-0.38, 0.42)$ $\cup(8.0, 8.8)$	(-0.73,0.88) $\cup(7.5, 9.1)$
FCC-ee	240	ZH	0.4	1.8	$(-0.26, 0.28)$ $\cup(9.4, 9.9)$	$(-0.51.0.57)$ $\cup(9.1, 10.2)$
	240	WBF H	2.2	0.66	$(-2.81, 5.1)$	$(-4.3, 6.6)$
	350	WBF H	0.6	0.65	$(-1.15, 3.4)$	$(-1.89, 4.1)$
ILC	250	ZH	0.71	1.6	$(-0.52, 0.59)$ $\cup(7.8, 8.9)$	$(-0.98, 1.3)$ $\cup(7.1, 9.4)$
	500	WBF H	0.23	0.63	$(-0.56, 2.7)$	$(-0.97, 3.1)$
	1000	WBF H	0.33	0.61	$(-0.78, 2.7)$	$(-1.3, 3.3)$
CLIC	350	ZH	1.65	0.59	$(-2.48, 4.3)$	$(-3.80, 5.6)$
	1400	WBF H	0.4	0.61	$(-0.91, 2.9)$	$(-1.50, 3.5)$
	3000	WBF H	0.3	0.59	$(-0.75, 2.6)$	$(-1.26, 3.1)$

Table 4.4: Expected precision ϵ for the measurements of single Higgs production modes and the expected 1σ and 2σ constraints on $\bar{c}_6$, assuming an SM measurement, are listed. The value of ϵ for the CEPC has been taken from ref. [116], for the FCC-ee from ref. [117], for the ILC from ref. [118] and for the CLIC from ref. [104].

1. As expected from a well-behaving EFT expansion, the contribution from $\bar{c}_8$ is suppressed and we can safely set $\bar{c}_8 = 0$. We explore how well we can measure $\bar{c}_6$, not only assuming $\bar{c}_6 \sim 0$, *i.e.*, an SM-like configuration, but also allowing for large BSM effects via $\bar{c}_6 \neq 0$.
2. The value of $\bar{c}_8$ can be different from zero and leads to non-negligible effects. We explore how well we can constrain $\bar{c}_8$ and how much $\bar{c}_8$ can affect the measurement of $\bar{c}_6$.

First, we study the sensitivity of ZH^n and WBF processes at the various colliders considered. Then we show combined results for the ILC and CLIC. It is important to note, however, that single Higgs production depends on $\bar{c}_8$ only via two-loop effects, which we did not calculate (see Tab. 4.1). Thus, we cannot directly combine single Higgs with double Higgs and triple Higgs in the case of Scenario 2. Nevertheless, we discuss the limit that can be obtained in single Higgs production under the assumption that the $\bar{c}_8$-dependent two-loop effects are negligible.

4.2.1 Single Higgs production

In this section we discuss the constraints that can be obtained on $\bar{c}_6$ via the single-Higgs production modes. As said, since the effects of $\bar{c}_8$ are unknown, we restrict our study to the case where it can be ignored, *i.e.*, Scenario 1. We start by considering the case in which we assume that the Higgs potential is like in the SM ($\bar{c}_6 = 0$) and then we consider the BSM case with $\bar{c}_6 \neq 0$.

In Tab. 4.4 we show 1σ and 2σ constraints on $\bar{c}_6$ that can be obtained via ZH and WBF H at different energies and colliders, using eq. (4.8). We show also the value of C_1 and the accuracy ϵ that can be achieved in any experimental setup, as provided in [104, 116–118]. In general and unless differently specified, we assume Gaussian distributions for the errors and no correlations among them, and the errors are rescaled according to cross section in BSM cases. In the results of Tab. 4.4 we did not take into account effects due to $\bar{c}_6$ in the Higgs decay, since, at variance with the LHC case, they can be in principle neglected at e^+e^- colliders. Indeed, the total cross section of $e^+e^- \to ZH$ production can be measured via the recoiling mass method [118], without selecting a particular H decay channel. Using the same method, the branching ratio of any (visible) decay channel can be precisely measured and used as input in the WBF H analysis, so that also in this case effects due to $\bar{c}_6$ in the Higgs decay can be neglected. Nevertheless, we explicitly checked that taking into account $\bar{c}_6$ effects in the decay for the $H \to b\bar{b}$ channel, which will be the one most precisely measured, results in Tab. 4.4 are almost unchanged.

As can be seen in eq. (4.8), not only a linearly $\bar{c}_6$ dependent term is present, but also a $\bar{c}_6^2$ one. Since C_2 is negative and C_1 is positive for both ZH and WBF H, the SM cross section value is degenerate in $\bar{c}_6$; besides the SM case $\bar{c}_6 = 0$ also a second different $\bar{c}_6 \neq 0$ condition is giving the same value of the cross section. While for the WBF H this second solution is close to $\bar{c}_6 = 2$, in ZH at 240-250 GeV this is around $\bar{c}_6 = 9$, depending on the energy. As a result, the two solutions being close to each other, in WBF H the 1σ and 2σ intervals are always broad, while in ZH at 240-250 GeV we see two narrow intervals: one around $\bar{c}_6 = 0$ and one around $\bar{c}_6 = 9$. Note that for CLIC-350 also ZH is yielding a broad interval as a constraint, since ϵ is larger and C_1 is smaller. Via the combined measurement of ZH and WBF H processes, or including LHC results in a global fit, the $\bar{c}_6$ region around $\bar{c}_6 = 9$ can be

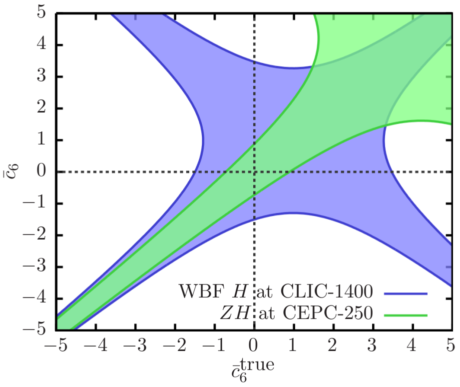

Figure 4.9: The 2σ bounds on $\bar{c}_6$ as a function of $\bar{c}_6^{\mathrm{true}}$ in single Higgs production in the Scenario 1 described in the text. Two representative cases are considered: ZH at CEPC-250 and WBF H at CLIC-1400.

excluded. In conclusion, assuming no other BSM effects, the best constraints on $\bar{c}_6$ via *single Higgs production* can be obtained at low energy and high luminosity.

We now consider the situation in which $\bar{c}_6$ has a value different from zero, which will denote as $\bar{c}_6^{\mathrm{true}}$, and we explore the constraints that can be set on $\bar{c}_6$, by varying the value of $\bar{c}_6^{\mathrm{true}}$. In Fig. 4.9 we consider ZH at CEPC-250 and WBF H at CLIC-1400 as examples. The bands in the plot show which constraints on $\bar{c}_6$ (y-axis) can be set, depending on the value of $\bar{c}_6^{\mathrm{true}}$ (x-axis). We considered only the $-5 < \bar{c}_6, \bar{c}_6^{\mathrm{true}} < 5$ range, so that results can be directly compared with the analogous analysis performed in the next section for double Higgs production, where this range cannot be extended without violating perturbativity (see Appendix B). The "X" shapes of the ZH and WBF H bands can be understood as follows. In the limit of zero uncertainties two solutions can be obtained from the equation $\sigma_{\mathrm{NLO}}^{\mathrm{pheno}}(\bar{c}_6) = \sigma_{\mathrm{NLO}}^{\mathrm{pheno}}(\bar{c}_6^{\mathrm{true}})$:

$$\bar{c}_6 = \bar{c}_6^{\mathrm{true}}, \tag{4.26}$$

$$\bar{c}_6 = -\frac{C_1}{\delta Z_H^{\mathrm{SM},\lambda}} - 2 - \bar{c}_6^{\mathrm{true}}, \tag{4.27}$$

which intersect each other at the point $P = \big(-\frac{C_1}{2\delta Z_H^{\mathrm{SM},\lambda}} - 1, -\frac{C_1}{2\delta Z_H^{\mathrm{SM},\lambda}} - 1\big)$. For ZH at CEPC-250 $P = (4.2, 4.2)$ and for WBF H at CLIC-1400 $P = (1.0, 1.0)$.[9] The uncertainties ϵ, however, are not negligible and determine the width of the branches, which are centred on the solutions in eqs. (4.26) and (4.27).

For ZH production, due to the large value of C_1, only one branch is present in the $-5 < \bar{c}_6, \bar{c}_6^{\mathrm{true}} < 5$ region. Instead, for WBF H, since C_1 is small, SM-like scenarios $\bar{c}_6^{\mathrm{true}} \sim 0$ lies in the intersection region of the branches. Thus, as already previously discussed, ZH provides stronger constraints for $\bar{c}_6^{\mathrm{true}} \sim 0$. On the contrary, for $\bar{c}_6^{\mathrm{true}} \sim 4$, WBF H constraints are stronger. We remind the reader that it is not obvious that the LHC, even after accumulating 3000 fb^{-1} of luminosity, will be able to exclude a value $\bar{c}_6 \sim 4$. Still, with a single measurement for $\bar{c}_6^{\mathrm{true}} \sim 4$ both the intervals around $\bar{c}_6 \sim 4$ and $\bar{c}_6 \sim -3$ are allowed, but the latter may be probed also at the LHC. As shown in Tab. 4.4, also for ZH and $\bar{c}_6^{\mathrm{true}} \sim 0$ there is a second interval in the constraints, but it is outside the range of the plot.

4.2.2 Double Higgs production

We now turn to the case of double Higgs production. The expected precisions ϵ for the measurements considered in our analysis[10] are listed in Tab. 4.5. Although double Higgs production cannot be measured as precise as single Higgs production, it depends on $\bar{c}_6$ at LO and therefore the sensitivity on this parameter is much higher.

We start our analysis considering Scenario 1, where we set $\bar{c}_8 = 0$. As can be seen in sec. 4.1.2, the WBF HH dependence on $\bar{c}_6$ is similar for different energies. For this reason, for Scenario 1, we show WBF HH only for CLIC-1400, together with ZHH at ILC-500. Similarly to Fig. 4.9, which concerns the case of single Higgs production, in Fig. 4.10 we plot the constraints that can be set on $\bar{c}_6$, by varying the value of $\bar{c}_6^{\mathrm{true}}$. Also in $\sigma_{\mathrm{LO}}(HH)$ both a linear and

---

[9] If we consider ZH at FCC-ee-240 we obtain $P = (4.9, 4.9)$.

[10] Note that the value of ϵ listed in ref. [104, 120] are for a different luminosities than those considered in Tab. 4.3. Since the statistical uncertainty is the dominant one, the values of ϵ in Tab. 4.5 have been obtained by rescaling those of ref. [104, 120] proportionally to the square root of the luminosity.

	$\sqrt{\hat{s}}$ [GeV]	process	ϵ
ILC [120]	500	ZHH	19%
	1000	WBF HH	23%
CLIC [104]	1400	WBF HH	33%
	3000	WBF HH	15%

Table 4.5: Expected precision ϵ for the measurements of double Higgs production processes. For the ILC the values of ϵ have been obtained rescaling the values in [120] to the luminosity of Tab. 4.4.

quadratic dependence on $\bar{c}_6$ are present, leading to “X”-shape bands. The “X”-shape is slightly asymmetric due to the one-loop σ_{30} and σ_{40} contributions that are present in $\sigma_{\rm NLO}^{\rm pheno}(HH)$, see eq. (3.30), which we always use in our study. The central points of the “X” bands are around $(\bar{c}_6^{\rm true}, \bar{c}_6) = (-2.5, -2.5)$ for ZHH at ILC-500, and around $(\bar{c}_6^{\rm true}, \bar{c}_6) = (0.5, 0.5)$ for WBF HH at CLIC-1400. For this reason, although the WBF HH band is narrower due to a larger $\bar{c}_6$ dependence, for values $\bar{c}_6^{\rm true} \sim 0$, ZHH at ILC-500 is giving better constraints. On the other hand, for values $\bar{c}_6^{\rm true} \neq 0$ and especially $\bar{c}_6^{\rm true} \sim -2.5$, WBF HH at CLIC-1400 is leading to better constraints. It interesting to note that the central points of the “X” bands in WBF H and WBF HH are very close, while for ZH and ZHH they are different. This implies that the combination of the information from WBF single and double Higgs production would not exclude any of the branches of the “X” shape. Thus, the information from ZH or ZHH is necessary for this purpose. We will comment again this point in sec. 4.2.4.

We now consider Scenario 2. Specifically, we assume that the true value for $\bar{c}_6$ is $\bar{c}_6^{\rm true}$ and that the measured cross section for double Higgs production is $\sigma^{\rm measured} = \sigma_{\rm NLO}^{\rm pheno}(\bar{c}_6 = \bar{c}_6^{\rm true}, \bar{c}_8 = 0)$ and we show which value of $(\bar{c}_6, \bar{c}_8)$ can be constrained via the prediction of $\sigma_{\rm NLO}^{\rm pheno}(\bar{c}_6, \bar{c}_8)$. Starting with the SM case, we show results for $\sigma^{\rm measured} = \sigma_{\rm NLO}^{\rm pheno}(\bar{c}_6 = 0, \bar{c}_8 = 0)$ in Fig. 4.11. We consider the range $|\bar{c}_6| < 5$ and $|\bar{c}_8| < 31$, because as explained in Appendix B for larger values the perturbative calculations cannot be trusted. The plot on the left shows the constraints for ZHH and WBF HH at the ILC-500, while the one on the right those for WBF HH at CLIC-1400 and CLIC-3000. First of all we can notice that the constraints on $\bar{c}_6$ are weaker than in Scenario 1.

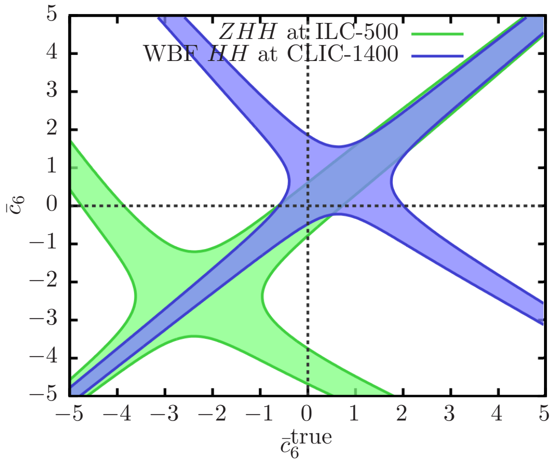

Figure 4.10: The 2σ bounds on $\bar{c}_6$ as a function of $\bar{c}_6^{\rm true}$ in double Higgs production in the Scenario 1 described in the text. Two representative cases are considered: ZHH at ILC-500 and WBF HH at CLIC-1400.

Also, no constraints on $\bar{c}_8$ independently from $\bar{c}_6$ can be set. On the other hand, the largest part of the $(\bar{c}_6, \bar{c}_8)$ plane can be excluded and the shape of the band depends on the process. It is important to note that this results depend on the choice of the renormalisation scale μ_r and therefore the scale at which $\bar{c}_6(\mu_r)$ and $\bar{c}_8(\mu_r)$ are measured. Our results refers to $\mu_r = 2m_H$, which corresponds to the production threshold for the HH pair. While the region close to the SM $(\bar{c}_6 \sim 0, \bar{c}_8 \sim 0)$ is very mildly affected by this choice, we warn the reader that the border of the plane $|\bar{c}_6| \sim 5$ and $|\bar{c}_8| \sim 31$ can be strongly affected.

We then consider how the constraints in the $(\bar{c}_6, \bar{c}_8)$ plane depend on the value of $\sigma^{\rm measured}$. We consider BSM configurations $\sigma^{\rm measured} = \sigma_{\rm NLO}^{\rm pheno}(\bar{c}_6 = \bar{c}_6^{\rm true}, \bar{c}_8 = 0)$ with $\bar{c}_6^{\rm true} \neq 0$.[11] In Fig. 4.12 we show the plots for the values of $\bar{c}_6^{\rm true} = -4, -2, -1, 1, 2, 4$; in each plot the point $(\bar{c}_6^{\rm true}, \bar{c}_8^{\rm true} = 0)$ is displayed with a cross and the value of $\bar{c}_6^{\rm true}$ is given. For these plots, only results for ZHH at ILC-500 and WBF HH at ILC-1000 are displayed. Similarly to the SM case, given a value of $\bar{c}_6^{\rm true}$, the constraints on $\bar{c}_6$ independent from $\bar{c}_8$ are weaker than those in Scenario 1. However, also in these cases, the

---

[11] As the total cross section depends on $\bar{c}_8$ mildly, we do not expect that the constraints depend on $\bar{c}_8^{\rm true}$

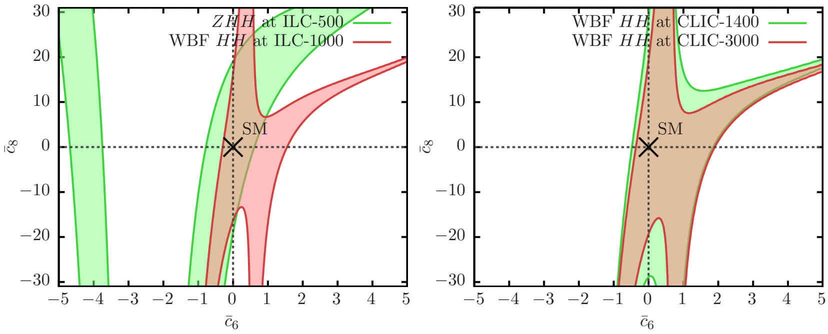

Figure 4.11: 2σ bounds in the $(\bar{c}_6, \bar{c}_8)$ plane assuming SM cross sections for double Higgs production in the Scenario 2 described in the text. Left: ZHH at ILC-500 and WBF HH at ILC-1000. Right: WBF HH at CLIC-1400 and CLIC-3000.

largest part of the $(\bar{c}_6, \bar{c}_8)$ plane can be excluded and the shapes of the bands strongly depend both on the process and the value of $\bar{c}_6^{\text{true}}$. In all cases, ZHH and WBF HH sensitivities are complementary; as we will see in sec. 4.2.4, their combination improves the constraints in the $(\bar{c}_6, \bar{c}_8)$ plane. This is a clear advantage for the ILC, where both ZHH and WBF HH can be precisely measured.

4.2.3 Triple Higgs production

We now consider the case of triple Higgs production. In the SM $ZHHH$ and WBF HHH production processes have a too small cross section for being observed. As an example, if we consider LR-polarised beams at 1 TeV and the dominant decay into a $b\bar{b}$ pair for the three Higgs bosons and into jets for the Z boson, about 6 ab^{-1} of integrated luminosity would be necessary for one signal event in the SM. As can be seen in Fig. 4.8, with WBF HHH the cross section is even smaller in the SM, on the other hand this process has a strong sensitivity on $\bar{c}_8$, due to the large value of σ_{02} factorising the $\bar{c}_8^2$ dependence. Thus, limits on $\bar{c}_6$ and $\bar{c}_8$ can be set, but only considering Scenario 2 where $\bar{c}_8$ can be different from zero.

At variance with double Higgs production, given the very small number of events, we cannot set limits on the $(\bar{c}_6, \bar{c}_8)$ plane by assuming $\sigma^{\text{measured}}(HHH) = \sigma_{\text{LO}}(\bar{c}_6 = \bar{c}_6^{\text{true}}, \bar{c}_8 = 0)$. Indeed, the number of events expected is close to zero and a Gaussian fit cannot be performed. Rather, we have to assume events are zero and compare them with the expected value of events for a given $(\bar{c}_6^{\text{true}}, \bar{c}_8^{\text{true}})$ performing a Poissonian analysis.[12] We assume that the other SM backgrounds are giving zero events and we estimate the signal efficiency ε_{HHH} by rescaling the one known for WBF HH production ε_{HH}. In practice, for both WBF HHH and $ZHHH$ production we estimate the signal efficiency to be $\varepsilon_{HHH} = \varepsilon_{HH}^{\frac{3}{2}} = 4.7\%$, where ε_{HH} has been taken from ref. [112].

In Fig. 4.13, we show the 2σ bounds in the $(\bar{c}_6, \bar{c}_8)$ plane. The plot on the left shows the constraints for $ZHHH$ and WBF HHH at ILC-1000, while the one on the right those for WBF HHH at CLIC-1400 and CLIC-3000. As can be seen, at ILC-1000 almost all the $(\bar{c}_6, \bar{c}_8)$ plane is compatible with a zero event condition, both for $ZHHH$ and WBF HHH production. On the other hand, at CLIC-1400 and especially at CLIC-3000 a vast area of the plane can be excluded via the study of WBF HHH production. In particular, at CLIC-3000, the constraint on $\bar{c}_8$ are comparable to those obtainable at a future 100 TeV hadron collider [48, 49]. The constraints on $\bar{c}_6$ are instead worse than in the double Higgs production case.

4.2.4 Combined bounds

We now investigate the constraints that can be obtained via the combination of the information from single, double and triple Higgs production. We consider both Scenarios 1 and 2 and, as already mentioned, in the case of Scenario 2 we combine only results from double and triple Higgs production. We show in parallel the limits on $\bar{c}_6$ from single Higgs production by assuming that the $\bar{c}_8$-dependent two-loop effects are small.

We start discussing the Scenario-1 analysis, separately considering the ILC and CLIC. For both colliders we progressively include results at higher energies in three stages. In the case of the ILC, we start with ZH at ILC-250, in a second

---

[12] In fact, for the case of CLIC-3000, large $\bar{c}_6$ values would lead to ~ 5 expected events. We will consider this effect in the combined analysis in sec. 4.2.4.

step we include ZHH and WBF H results from ILC-500 and finally $ZHHH$ and WBF $H(H(H))$ from ILC-1000. Instead, in the case of the CLIC, we start with ZH at CLIC-350, in a second step we include WBF $H(H(H))$ and $ZHHH$ results from CLIC-1400 and finally WBF $H(H(H))$ results from CLIC-3000. In the case of triple Higgs production we assume that we observe as many events as predicted by $\sigma_{\rm LO}(HHH)$ in eq. (4.25), with $\bar{c}_8 = 0$.

In Fig. 4.14, we show the combined results for the ILC (left) and CLIC (right) assuming Scenario 1. In the first stage, both ILC-250 and CLIC-350 constraints are worse than those of CEPC-250 shown in Fig. 4.9. This is due to a lower precision in the measurements (ϵ) and for CLIC-350 also a smaller value of C_1. However, in the second stage, including results at higher energies, for both colliders constraints are much stronger, since double Higgs production becomes available. Especially, combining single and double Higgs production the "X" shape disappears and only the band around the line $\bar{c}_6 = \bar{c}_6^{\rm true}$ remains.[13] In the case of the CLIC, bumps are still present at $\bar{c}_6 \sim 1$, which originate from the centre of the "X"-shape band for WBF $H(H)$ at CLIC-1400, see Fig. 4.9 and Fig. 4.10. For the same reason, also for the ILC the band is slightly larger around $\bar{c}_6 \sim 1$. In the third stage, constraints are improved both for the ILC and CLIC. Still, the weaker bounds can be set for $\sim 0 < \bar{c}_6^{\rm true} < 1$, where the center of the "X"-shape band for WBF HH is located. In this region, constraints are better at the ILC thanks to the ZHH contribution at 500 GeV, which helps to resolve this region.

We now consider Scenario 2. As done in the case of double Higgs production we assume that the true value for $\bar{c}_6$ is $\bar{c}_6^{\rm true}$ and that $\sigma^{\rm measured} = \sigma^{\rm pheno}_{\rm NLO}(\bar{c}_6 = \bar{c}_6^{\rm true}, \bar{c}_8^{\rm true} = 0)$ while that for triple Higgs production we observe as many events as predicted by $\sigma_{\rm LO}(HHH)$ in eq. (4.25), with $\bar{c}_8 = 0$. In the case of the ILC, we consider ZHH at ILC-500 and its combination with ILC-1000 results from $ZHHH$ and WBF $HH(H)$ production. In the case of CLIC, we consider $ZHHH$ and WBF $HH(H)$ production at CLIC-1400 and its combination with WBF $HH(H)$ at CLIC-3000. Thus, while ILC-500 is not a combined result, being simply obtained for ZHH production, all the others include information from both double and triple Higgs production. As already

---

[13] In the case of CLIC, where the ZHH information is not entering the combination, also the information from triple Higgs production is necessary for this purpose.

said, single Higgs production cannot be directly included in the combination, since its $\bar{c}_8$ dependence starts at two-loop level.

In Fig. 4.15 we show results for the SM case ($\bar{c}_6^{\text{true}} = 0, \bar{c}_8^{\text{true}} = 0$) as green bands. There we also show as red bands the limits on $\bar{c}_6$ extracted from single Higgs measurements at the ILC and CLIC[14], assuming that the two-loop $\bar{c}_8$ dependence is negligible. Due to the available higher energies, combined double and triple Higgs constraints at the CLIC are better than at the ILC. Indeed the WBF $HH(H)$ production cross section increases with the energy. On the other hand, single Higgs production can be better measured at the ILC and therefore the corresponding constraints on $\bar{c}_6$ are better than at the CLIC. We notice that the only case where single Higgs results may be relevant in a further combination with those from double and triple Higgs production is the case of ILC-500, which is actually coming from only ZHH production. Indeed, the combination of ZH at ILC-250 and WBF H at ILC-500 would help in removing the band around $\bar{c}_6 = -4$, and shrinking the possible region for the band around SM value. On the contrary, at higher energies the WBF HH production is more relevant in constraining $\bar{c}_6$. Thus, with the exception of ILC-500, single Higgs production could be helpful in constraining the $(\bar{c}_6, \bar{c}_8)$ plane only if the dependence on $\bar{c}_8$ at two-loop is larger than what we assumed or if low-energy runs at higher luminosity, such as those at circular colliders, are considered.

In Fig. 4.16 we show the constraints from the combination of double and triple Higgs for BSM cases $\bar{c}_6^{\text{true}} = -4, -2, -1, 1, 2, 4$. As already discussed for the SM case, constraints from single Higgs production are negligible for high energy e^+e^- colliders in this scenario under our assumptions and for this reason they are not shown. We display in each plot both CLIC and ILC bounds. As we can see, both in the SM and in all BSM cases considered, the combination of results from double and triple Higgs production is always strongly improving the bounds. Also, with higher energies, stronger constraints can be set; the best results can be obtained combining results at CLIC-1400 with those at CLIC-3000, especially for $\bar{c}_6^{\text{true}} \neq 0$ since a non-zero number of events can

---

[14] More specifically, for the ILC, the single Higgs limit are combined results from ZH at ILC-250, WBF H at ILC-500, and WBF H at ILC-1000, while for the CLIC, the single Higgs limit are combined results from ZH at CLIC-350, WBF H at CLIC-1400, and WBF H at CLIC-3000.

be observed. It is interesting to note that CLIC bounds around $(\bar{c}_6^{\rm true}, \bar{c}_8^{\rm true})$ are less sensitive than at the ILC on the value of $\bar{c}_6^{\rm true}$, featuring vertical elongated contours in the $(\bar{c}_6, \bar{c}_8)$ plane. The reason is that at CLIC bounds mainly comes from WBF HHH, while at the ILC mainly from double Higgs production, both ZHH and WBF HH.

In conclusion we observed that low- and high-energy runs are useful for constraining the shape of the Higgs potential. Under the assumption of Scenario 1, we have shown the complementarity of ZH production at low energy with WBF HH information at higher energies. Under the Scenario 2, we have shown that the combination of the information from double and triple Higgs production, which is possible only at high energy, improves the constraints in the $(\bar{c}_6, \bar{c}_8)$ plane (*cf.* fig. 4.12 with fig. 4.16).

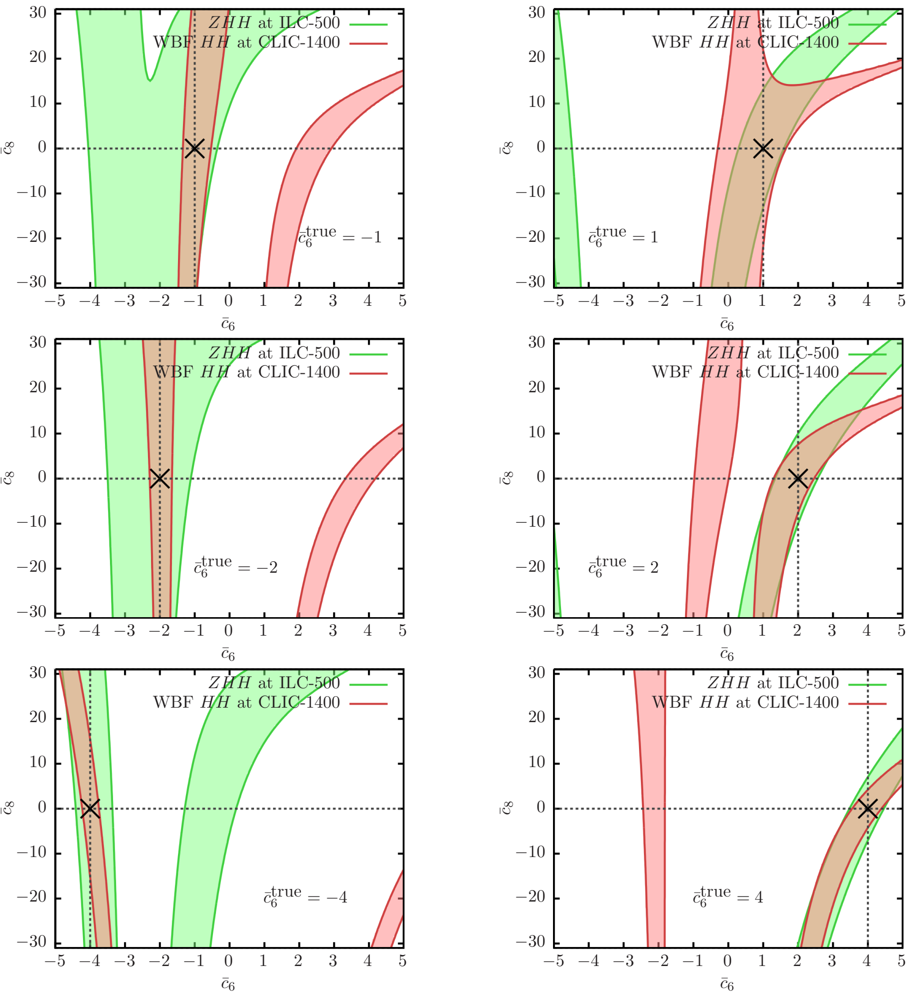

Figure 4.12: 2σ bounds in the $(\bar{c}_6, \bar{c}_8)$ plane assuming BSM cross sections in double Higgs production corresponding to $(\bar{c}_6^{\rm true}, \bar{c}_8^{\rm true} = 0)$ in the Scenario 2 described in the text, with $\bar{c}_6^{\rm true} = -4, -2, -1, 1, 2, 4$ marked in the plots with a cross. All plots show results for ZHH at ILC-500 and WBF HH and CLIC-1400.

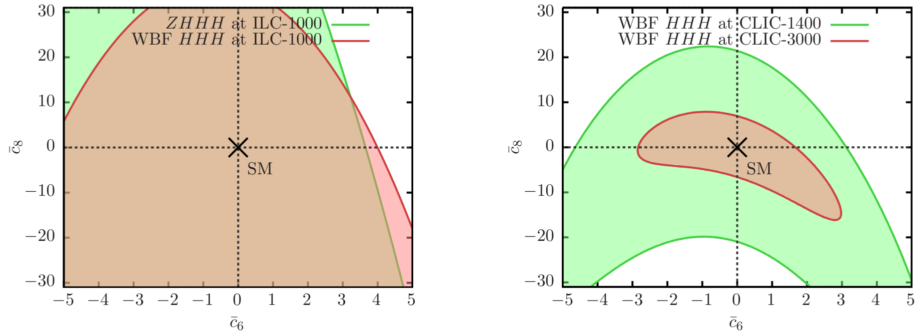

Figure 4.13: 2σ bounds in the $(\bar{c}_6, \bar{c}_8)$ plane assuming SM cross sections in triple Higgs production in the Scenario 2 described in the text. Left: $ZHHH$ and WBF HHH at ILC-1000. Right: WBF HHH at CLIC-1000 and CLIC-1400.

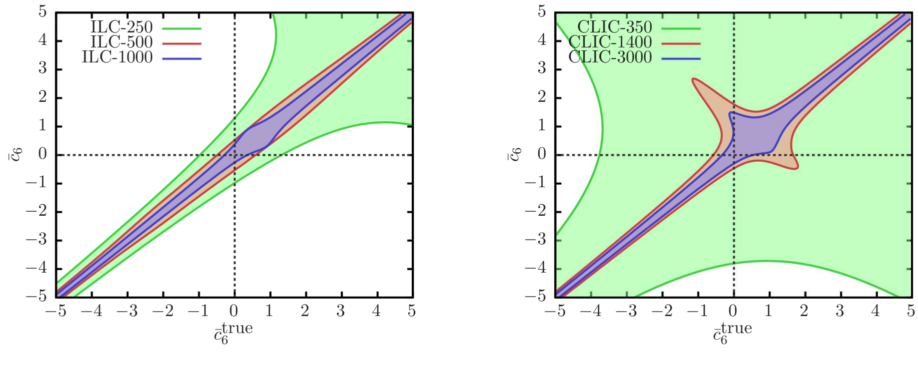

Figure 4.14: Combined 2σ constraints on $\bar{c}_6$ as a function of $\bar{c}_6^{\text{true}}$ for the ILC (left) and the CLIC (right) in the Scenario 1 described in the text.

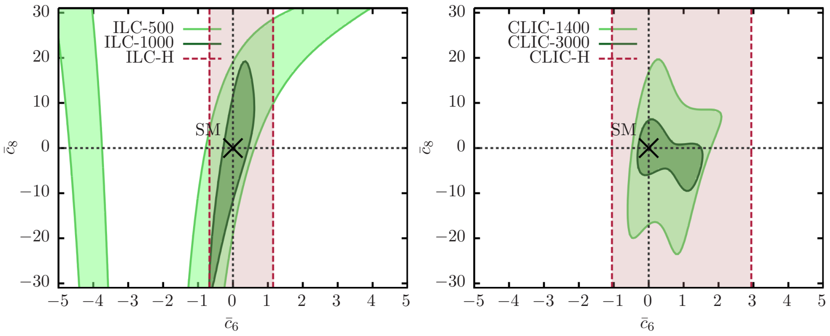

Figure 4.15: Combined 2σ constraints in the $(\bar{c}_6, \bar{c}_8)$ assuming SM cross sections, at the ILC (left) and CLIC (right), in the Scenario 2 described in the text. ILC-H and CLIC-H refer to a combination of all single Higgs measurements at all energy stages for each collider under study.

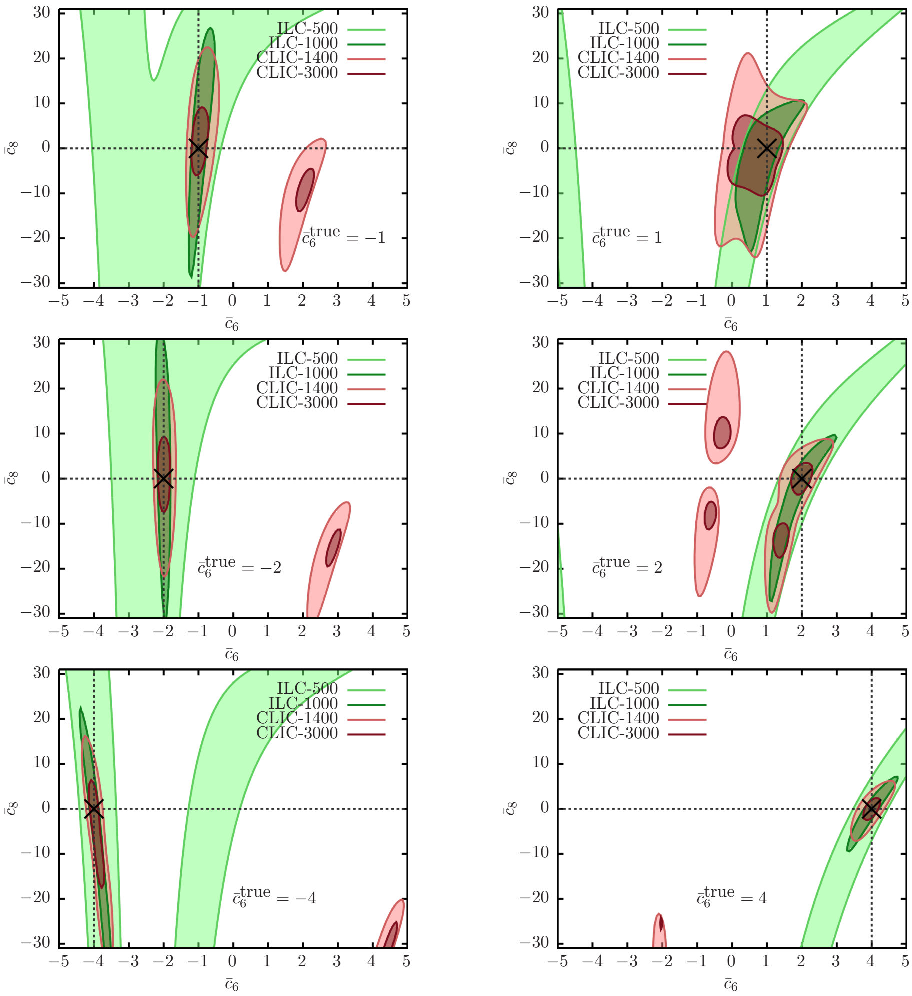

Figure 4.16: Combined 2σ bounds in the $(\bar{c}_6, \bar{c}_8)$ plane assuming BSM cross sections corresponding to $(\bar{c}_6^{\rm true}, \bar{c}_8^{\rm true} = 0)$ in the Scenario 2 described in the text, with $\bar{c}_6^{\rm true} = -4, -2, -1, 1, 2, 4$ marked in the plots with a cross.

5 Higgs boson self-couplings at future muon colliders

Due to its heavier mass comparing to electrons, muon colliders can reach much higher energy. Since vector boson fusion cross section increases as energy grows, it provides a good opportunity to study constraints on Higgs boson self-couplings at future muon collider.

In this chapter we consider WBF production mode only. As discussed in the previous chapter, Other production modes such as $t\bar{t}$-associated production are suppressed comparing to WBF at such high energy. In Fig. 5.1 we show the cross section of single-, double- and triple Higgs production via Z boson associated production and WBF. While $ZHHH$ is comparable or even larger than WBF around $\sqrt{s} = 1$ TeV, in the preivous chapter we found that the sensitivity on the Higgs quartic self-coupling is much weaker than WBF.

$\sqrt{s}$ (TeV)	1.5	3	6	10	14	30
$\mathcal{L}$ ($10^{34}\,\mathrm{cm}^{-2}\mathrm{s}^{-1}$)	1.2	4.4	12	20	33	100
L_{10y} (ab^{-1})	1.2	4.4	12	20	33	100

Table 5.1: Reference muon collision energies $\sqrt{s}$, and instantaneous luminosities $\mathcal{L}$, with corresponding integrated luminosities L for a 10 years run (one year of $\sim 10^7$s). The luminosity values assumed for $\sqrt{s} \simeq (1.5, 3, 6, 14)$ TeV are as from [121, 122].

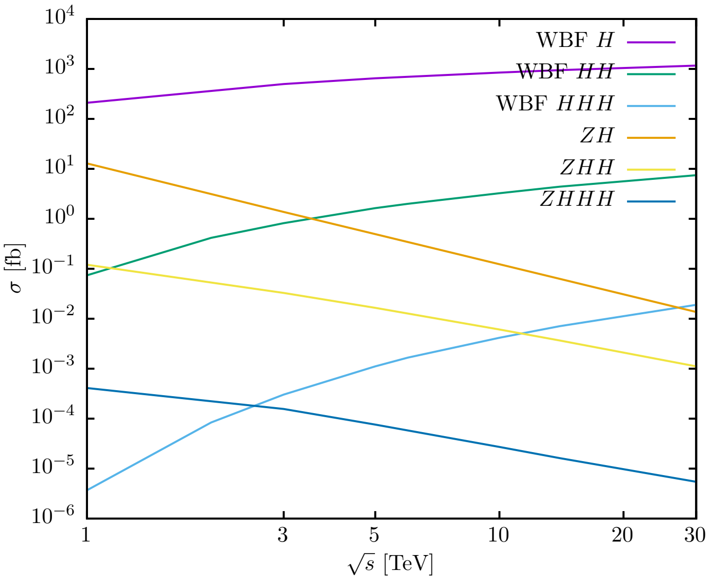

Figure 5.1: The cross section for single-, double- and triple Higgs production at muon collider are shown.

5.1 Triple Higgs production in the standard model

In this section, we present the cross sections and a few kinematical distributions for the process

$$\mu^+\mu^- \to HHH\,\nu\overline{\nu}, \tag{5.1}$$

in the SM and in scenarios where the Higgs self-couplings are modified, at muon collider energies given in Table 5.1.

In figure 5.2, we show a few representative Feynman diagrams of the process. By inspection, one can quickly conclude that at the tree level, each diagram can be at most linearly dependent on the quartic self-coupling λ_4, and linearly or quadratically dependent on λ_3. In fact, the majority of diagrams are independent from Higgs self-couplings. This observation leads to the expectation that on the one hand, the cross section sensitivity to self-couplings in general and to the quartic coupling in particular, will be quite mild and on the other hand, a very precise knowledge of the WWH and $WWHH$ couplings will be needed in order to pin down the Higgs potential.

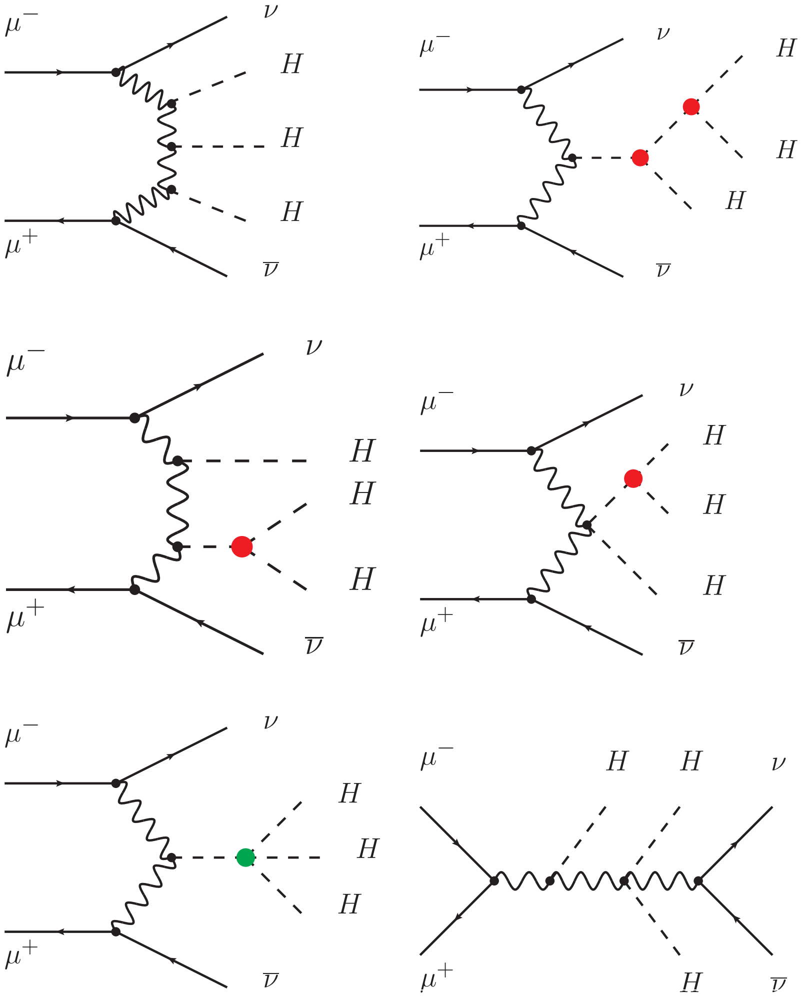

Figure 5.2: Representative Feynman diagrams contributing to the process $\mu^+\mu^- \to HHH\nu\overline{\nu}$ that do not involve self-couplings (top-left and bottom-right), involve the trilinear twice (top-right) and once (central), and the quartic (bottom-left) couplings. s-channel diagrams (bottom-right) contribute but become negligible at high energy (note that in this case $\nu = \nu_e, \nu_\mu, \nu_\tau$).

Triple Higgs production proceeds through two main classes of diagrams: the WBF channel [1]

$$\mu^+\mu^- \to W^*W^*\nu_\mu\overline{\nu}_\mu \to HHH\,\nu_\mu\overline{\nu}_\mu, \tag{5.2}$$

and the s-channel

$$\mu^+\mu^- \to HHH\;Z^* \to HHH\,\nu_{e,\mu,\tau}\overline{\nu}_{e,\mu,\tau}\;. \tag{5.3}$$

Both sets contribute at the amplitude level to $\mu^+\mu^- \to HHH\nu\overline{\nu}$ yet, as we will discuss in the following, mostly in different phase space regions.

In order to compute the $\mu^+\mu^- \to HHH\nu\overline{\nu}$ cross sections and distributions, including the complete self-coupling dependence, we have used two Monte Carlo event generators: one is WHIZARD [123, 124] (version 2.6.4), and the other is MADGRAPH5_AMC@NLO [62]. Even though the SM implementation in both codes does not allow the user to change λ_3 and λ_4 from the from the input cards, it is sufficiently easy to do that directly accessing the source codes. [2] The Higgs and gauge boson widths as well as the muon mass (and Yukawa) are set to zero, in order to avoid issues with gauge cancellations at very high energy.

For all the results discussed in the following, we impose a technical generation cut $M_{\nu\overline{\nu}} > 150$ GeV on the neutrino pair invariant mass $M_{\nu\overline{\nu}}$, to prevent the singularity arising from a vanishing Z-boson width in the s-channel. The latter cut effectively takes away most of the s-channel contribution. The s-channel effects tend anyhow to be strongly suppressed at multi-TeV collision energies. After removing the Z-resonance contributions by the $M_{\nu\overline{\nu}} > 150$ GeV cut, we find that the relative off-shell contribution of the $\mu^+\mu^-\to HHHZ^*\to HHH\,\nu\overline{\nu}$ to the total cross section is about 2.5% at $\sqrt{s}\simeq$1.5 TeV, $1.4{\cdot}10^{-3}$ at 3 TeV, and 10^{-4} at 6 TeV. With the present LO accuracy, our complete results for $\mu^+\mu^- \to HHH\,\nu\overline{\nu}$ will then match the ones for the WBF process

---

[1] The corresponding cross sections for Z boson fusion, $\mu^+\mu^- \to Z^*Z^*\mu^+\mu^- \to HHH\,\mu^+\mu^-$ amount to 15–20% of the ones for W boson fusion, and therefore relevant. We leave their inclusion to future work.

[2] In MADGRAPH5_AMC@NLO is also possible to use the SMEFT@NLO model.

$\mu^+\mu^- \to W^*W^*\nu_\mu\overline{\nu}_\mu \to HHH\nu_\mu\overline{\nu}_\mu$ with excellent accuracy in the energy range considered. [3]

In figure 5.3, we plot the $\mu^+\mu^- \to HHH\nu\overline{\nu}$ cross section versus $\sqrt{s}$ in the SM. On the right axis we include the expected number of triple Higgs final states produced for an integrated luminosity L=100 ab^{-1}. The left-hand plot corresponds to the cross-sections results in a linear scale for two anomalous scenarios as obtained in WHIZARD, while on the right-hand side the MADGRAPH5_AMC@NLO results for the yield are plotted in a log-scale, also for two additional scenarios. We have carefully verified that the results from the two MC's agree within uncertainties for SM as well as in presence of anomalous interactions. We define $\delta_{3,4}$ and $\kappa_{3,4}$, through the following relations

$$\lambda_3 = \lambda_{SM}(1+\delta_3) = \kappa_3\lambda_{SM}\,, \tag{5.4}$$

$$\lambda_4 = \lambda_{SM}(1+\delta_4) = \kappa_4\lambda_{SM}\,, \tag{5.5}$$

which imply that the SM values for the couplings are recovered for $\delta_{3,4} = 0$, or equivalently for $\kappa_{3,4} = 1$. We point out that, for the sake of both simplicity and generality, we phrase our results in terms of the anomalous couplings above. At the perturbative level of our predictions, *i.e.*, at the tree level, one can easily link the deformations of the λ's to the coefficients of higher dimensional operators, see for instance [125]. The simplest instance is that of adding just one operator of dimension six, $c_6(\Phi^\dagger\Phi)^3/\Lambda^2$. In this case, one finds that the shifts in the trilinear and quartic couplings are related, *i.e.*,

$$\delta_4 = 6\,\delta_3, \qquad (\text{SMEFT at dim} = 6). \tag{5.6}$$

This constraint can be lifted by further adding operators of higher dimension, *i.e.*, $c_8(\Phi^\dagger\Phi)^4/\Lambda^4$. As special case of the latter situation, one can fix the couplings of the six and eight dimensional operators, to only have the quartic coupling modified, $\delta_3 = 0$ and $\delta_4 \neq 0$. However, it is important to remind that this is not what is generically expected from the SMEFT and it implies a fine tuning, which is valid only at a given scale.

---

[3] Note that interference effects between the WBF and s-channel diagrams are negligible due to the non-overlapping typical kinematics of the two configurations. For the reasons above, in MADGRAPH5_AMC@NLO we find it easier to directly exclude the s-channel contributions by actually simulating $e^+\mu^- \to HHH\nu_\mu\overline{\nu}_e$. We have explicitly checked that this approximation is excellent and make the simulations faster.

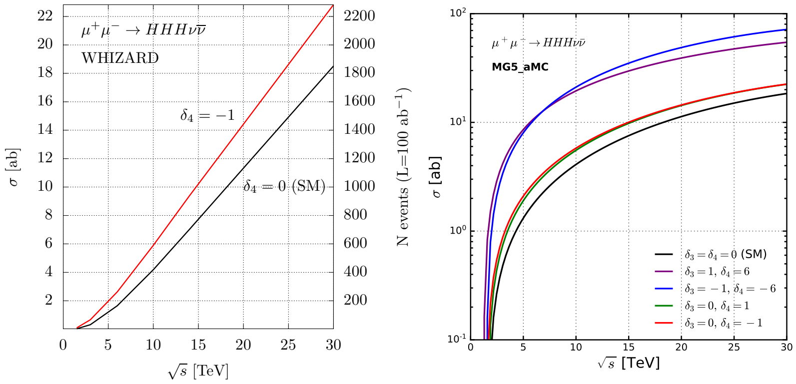

Figure 5.3: Expected cross sections (left) and signal event numbers for a reference integrated luminosity of 100 ab^{-1} (right) for $\mu^+\mu^- \to HHH\nu\bar{\nu}$ versus the c.m. collision energy, for $M_{\bar{\nu}\nu} \gtrsim 150$GeV. Cross sections for different assumptions of the trilinear and quartic couplings are presented, as well as for the SM case, obtained by WHIZARD (left-hand side) and MADGRAPH5_AMC@NLO (right-hand side). Details on the scenarios are given in the text.

In order to get a first feeling of the cross section sensitivity to variations of the Higgs quartic coupling, in figures 5.3 we also show the cross section obtained by keeping the SM value for λ_3 and switching off λ_4 ($\delta_3 = 0, \delta_4 = -1$ or $\kappa_3 = 1, \kappa_4 = 0$). The effect is an increase, as expected from general arguments on unitarity cancellation, of production rates of about $20\%-30\%$ in the $\sqrt{s}$ range considered here. On the right-hand plot, we show the corresponding results as obtained from MG5AMC also including two scenarios of interest: the $\delta_3 = \pm 1, \delta_4 = \pm 6$ cases, corresponding to relative shift between δ_3 and δ_4 consistent with an EFT approach, and a scenario $\delta_3 = 0, \delta_4 = +1$ with no change in λ_3, yet a 100% increase of λ_4. It is interesting to note that, as far as total rates are concerned, the latter case turns out to be hardly distinguishable from the scenario where $\lambda_3 = \lambda_{SM}$ and $\lambda_4 = 0$.

$\sqrt{s}$ [TeV]	1.5	3	6	10	14	30
Lumi [ab^{-1}]	1.2	4.4	12	20	33	100
σ_{SM} (ab) [$N_{\rm ev}$]						
total	0.03 [0]	0.31 [1]	1.65 [20]	4.18 [84]	7.02 [232]	18.51 [1851]
$m_{HHH} <$ 3TeV	0.03 [0]	0.31 [1]	1.47 [18]	2.89 [58]	3.98 [131]	6.69 [669]
$m_{HHH} <$ 1TeV	0.02 [0]	0.12 [1]	0.26 [3]	0.37 [7]	0.45 [15]	0.64 [64]

Table 5.2: Cross sections and (in squared brackets) event numbers for triple Higgs production via the process $\mu^+\mu^- \to HHH\nu\overline{\nu}$, at collision energies and integrated luminosities as from table 5.1. A cut $M_{\bar{\nu}\nu} \gtrsim 150$GeV is applied. The effect of imposing an upper cut on the HHH invariant mass is also detailed. Cross sections and corresponding event numbers refer to the SM case.

A second set of relevant information is provided in table 5.2, where we report the $\mu^+\mu^- \to HHH\nu\overline{\nu}$ total cross sections and event numbers [4] for the reference set of collision energies and integrated luminosities of table 5.1. In addition to total cross sections, also the number of events close to threshold, *i.e.*, with a requirement on the HHH-invariant-mass (M_{HHH}) to be less than 1 and 3 TeV is given. As we will discuss in the following, the sensitivity to the quartic coupling depends rather strongly on the phase space region occupied by the Higgs bosons in the final state, being the strongest close to threshold.

In figures 5.4, 5.5, 5.6 we plot the inclusive Higgs transverse momentum, the Higgs rapidity and the Higgs-pair ΔR distributions, with and without an upper cut of 1 TeV on the HHH invariant mass, respectively. We note that peak value of the transverse momentum is around 100 GeV, a value that turns out to be rather independent on the collider energy. The invariant mass cut at 1 TeV has a mild effect and only on the shapes of the distributions at higher energy collisions. On the other hand, the rapidity distributions are found to have a rather strong dependence on the collision energy and also on being at threshold. At high collision energy the rapidity range become quite large reaching more than five units in rapidity. To be detected, such Higgs bosons would need a very wide rapidity coverage of the detector. Finally, figure 5.6

---

[4] A cut $M_{\bar{\nu}\nu} \gtrsim 150$ GeV will be implicit from now on.

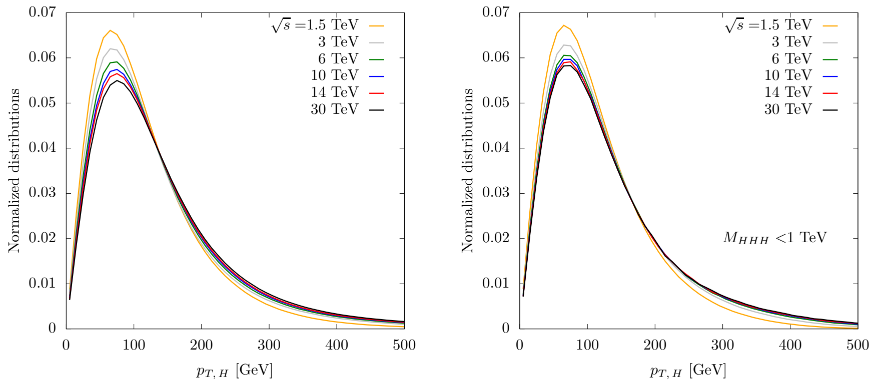

Figure 5.4: Inclusive Higgs transverse momentum distributions (normalized) for the $\mu^+\mu^- \to HHH\nu\overline{\nu}$ process, in the SM, at different collision energies. A technical cut of $M_{\bar{\nu}\nu} \gtrsim 150$ GeV is included. The plot on the right includes an upper cut of 1 TeV on the HHH invariant mass.

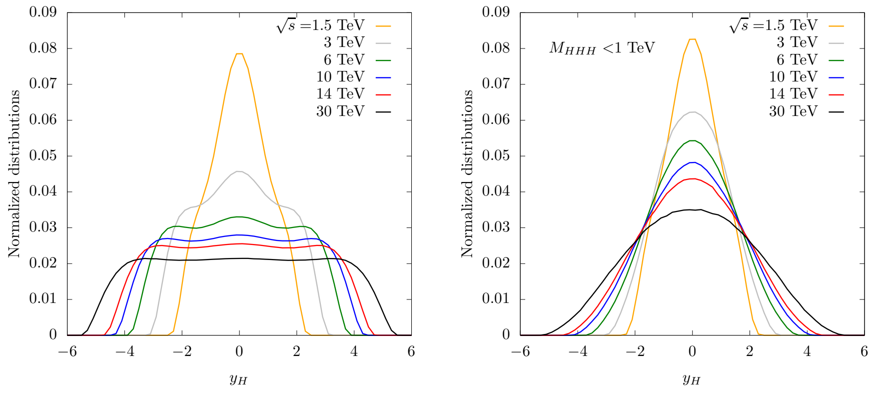

Figure 5.5: Inclusive Higgs rapidity distributions (normalized) for the $\mu^+\mu^- \to HHH\nu\overline{\nu}$ process, in the SM, at different collision energies. A technical cut of $M_{\bar{\nu}\nu} \gtrsim 150$ GeV is included. The plot on the right includes an upper cut of 1 TeV on the HHH invariant mass.

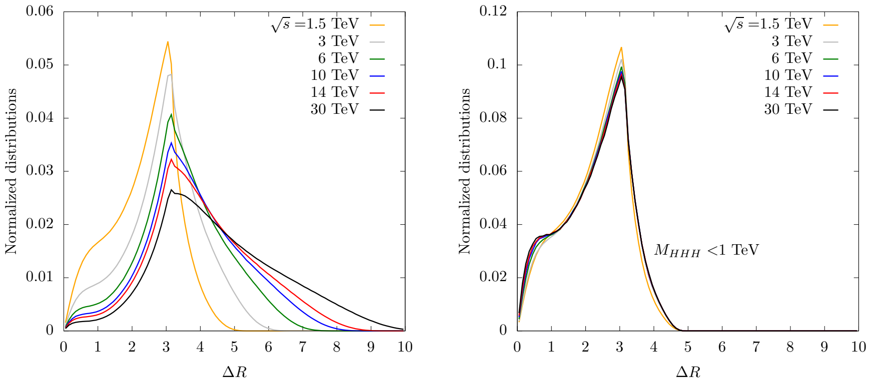

Figure 5.6: Inclusive ΔR distributions (normalized) for the $\mu^+\mu^- \to HHH\nu\overline{\nu}$ process, in the SM, at different collision energies. A technical cut of $M_{\bar{\nu}\nu} \gtrsim 150$ GeV is included. The plot on the right includes an upper cut of 1 TeV on the HHH invariant mass.

shows that the most probable distance between two Higgs bosons is around π, extending to larger values at high energy, due to forward-backward Higgs production. At threshold, there is a very mild dependence on the collision energy.

In order to have a more complete understanding of the dynamics of a HHH event, in figure 5.7 we present the rapidity and ΔR distributions of each of the Higgs bosons ordered in p_T. The solid curves represent the inclusive sample with no lower or upper cut of 1 TeV on the M_{HHH}. By inspecting the two plots one concludes that at threshold the ordering of the Higgs in p_T has mild effect as the Higgs have comparable momenta. On the other hand, in far from threshold configurations, which dominate inclusive cross sections, two Higgs bosons are typically rather central and back-to-back, while the softest one is forward.

5.2 Triple Higgs production with anomalous self-couplings

We can now pass to consider in detail how modifications of the trilinear and quartic couplings can modify cross sections and distributions. As already mentioned, the Feynman diagrams contributing to the process $\mu^+\mu^- \to HHH\nu\overline{\nu}$

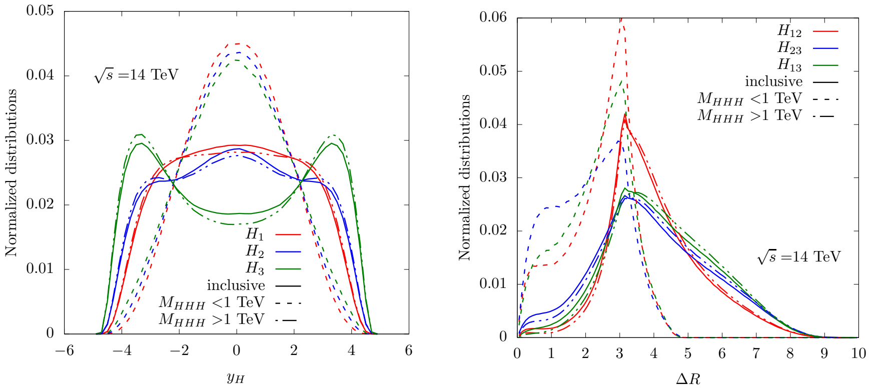

Figure 5.7: Higgs rapidity (left) and Higgs-pair ΔR (right) distributions in $\mu^+\mu^- \to HHH\nu\overline{\nu}$, in the SM, at $\sqrt{s}$ $\simeq$14 TeV, for $M_{\bar{\nu}\nu} \gtrsim$ 150 GeV. The index 1 refers to the highest-p_T Higgs, while the index 3 refers to the lowest-p_T Higgs. The solid lines stand for the inclusive distributions, the dashed (dotdashed) lines correspond to applying a further cut $M_{HHH} < (>)$1 TeV.

can involve one quartic Higgs vertex or up to two Higgs trilinear vertices, see figure 5.2.

As a result, the most general expression for the cross section as a function of the deviations from the SM cubic and quartic Higgs couplings can be expressed in terms of a polynomial which is quartic in δ_3 and quadratic in δ_4:

$$\sigma = c_1 + c_2\delta_3 + c_3\delta_4 + c_4\delta_3\delta_4 + c_5\delta_3^2 + c_6\delta_4^2 + c_7\delta_3^3 + c_8\delta_3^2\delta_4 + c_9\delta_3^4 \, , \quad (5.7)$$

where the coefficients c_i can be obtained once for all from a MC simulation and they are collected in table 5.3, for the total cross sections with and without an upper cut on the HHH invariant mass of 1 TeV. This parametrization is useful for at least two reasons. The first is that it can be used to extract sensitivities to different scenarios without the need to rerun MC simulations for each benchmark point. The second advantage is that it is possible to directly gauge the sensitivity to new physics effects by comparing the value of the SM coefficient (c_1), with the linear terms c_2, c_3, which are dominant for $\delta_{3,4} \ll 1$, and the quadratic (mixed or diagonal) terms ($c_{4,5,6}$), the cubic ($c_{7,8}$) and finally the quartic terms (c_9). First, the SM coefficient, as we had already seen in figure 5.3, grows faster than linearly, yet tends to flatten at high energy. As also seen before, the increase of the cross section is clearly provided by configurations which are far from threshold, and where at least one Higgs boson is soft and can be very forward. In fact, once an upper cut on the HHH invariant mass of 1 TeV is set, the increase on the cross sections is less than linear and very mild. Second, at the linear level and for total cross sections, the sensitivity to δ_4 is from 2 to 100 smaller than that of δ_3. On the other hand, if one focuses on events at threshold, there is a rather uniform difference of only a factor of two, the sign being opposite. This generically implies that positively correlated changes of the δ_4 and δ_3, will be more difficult to constrain than variations in opposite directions. For example, in the SMEFT case where $\delta_4 = 6\,\delta_3$, there will be a cancellation, yet with the δ_4 contribution being dominating. More in general, the difference between the sensitivity at the inclusive level and at threshold, entails the possibility for flat directions in the parameter space to be lifted. Third, in presence of larger deviations, the higher-order terms in the polynomial could become the dominant effects. In this case, one notices that c_6, corresponding to the δ_4^2 term, is always smaller than c_4, the coefficient of the $\delta_3\delta_4$ term. This means that a joint departure of the trilinear and quartic term will be in general easier to detect, than that of the quartic alone.

Finally, we investigate the discriminating power of differential distributions, focusing our attention on the HHH invariant mass. In figure 5.8 we plot the ratio between the M_{HHH} distribution in a scenario where $\delta_3 = 0$, for $\delta_4 = -0.5, -0.2, -0.05$ (left plot) and for $\delta_4 = 0.5, 0.2, 0.05$ (right plot) for different c.m. energies. The first observation is the size as well as the dependence of the corrections on the M_{HHH} are very different between positive and negative values of δ_4. The main reason can be traced back to the fact that even at the total integrated level the linear coefficient c_3 is negative while the quadratic coefficient c_6 is positive. For negative values of δ_4 the contributions sum and the final result is always larger than the SM, the larger effects being at threshold. For positive values of δ_4, cancellations take place between the differential version of c_3 and c_6, leading to a final non trivial pattern shown on the right plot: corrections start negative very close to threshold, and then become positive above about 600-800 GeV. In figure 5.9 we show the results of an analogous study, assuming $\delta_3 = -0.5, -0.2, -0.05$ (left plot) and $\delta_3 = 0.5, 0.2, 0.05$ with $\delta_4 = 6\,\delta_3$, *i.e.*, in the SMEFT scenario. Also in

$\sigma = c_1 + c_2\delta_3 + c_3\delta_4 + c_4\delta_3\delta_4 + c_5\delta_3^2 + c_6\delta_4^2 + c_7\delta_3^3 + c_8\delta_3^2\delta_4 + c_9\delta_3^4$					
$\sqrt{s}$ (TeV)	3	6	10	14	30
c_i (ab)					
c_1	0.3127	1.6477	4.1820	7.0200	18.5124
c_2	-0.1533	-1.7261	-4.4566	-7.1000	-15.9445
c_3	-0.0753	-0.1159	-0.1166	-0.1147	-0.1117
c_4	-2.0566	-6.3052	-11.4981	-15.9807	-29.2794
c_5	4.7950	14.9060	27.1081	37.4658	67.7539
c_6	0.2772	0.8637	1.5992	2.2455	4.2038
c_7	-1.8353	-4.3210	-6.6091	-8.3962	-13.0964
c_8	0.5032	1.1861	1.8173	2.2967	3.5217
c_9	0.2943	0.5954	0.8946	1.1611	1.9349
$\bar{c}_i \equiv c_i(M_{HHH} < 1$ TeV) (ab)					
$\bar{c}_1$	0.1165	0.2567	0.3743	0.4541	0.6404
$\bar{c}_2$	0.1667	0.3003	0.4046	0.3545	0.6972
$\bar{c}_3$	-0.0768	-0.1510	-0.2105	-0.2285	-0.3519
$\bar{c}_4$	-1.3604	-2.8996	-4.1522	-5.0582	-6.9538
$\bar{c}_5$	3.1017	6.6033	9.4721	11.4547	15.9505
$\bar{c}_6$	0.1842	0.3954	0.5679	0.6931	0.9543
$\bar{c}_7$	-1.5210	-3.0591	-4.3186	-4.8598	-7.3196
$\bar{c}_8$	0.4222	0.8550	1.2103	1.3906	2.0398
$\bar{c}_9$	0.2691	0.5482	0.7720	0.9702	1.2482

Table 5.3: Coefficients c_i, ruling the $\mu^+\mu^- \to HHH\nu_\mu\overline{\nu}_\mu$ cross-section dependence on the Higgs anomalous self-couplings δ_3 and δ_4 (as defined in the first row of the table), at different c.m. energies. The coefficients $\bar{c}_i$, entering the residual cross sections after applying a 1-TeV upper cut on the HHH invariant mass, are also detailed.

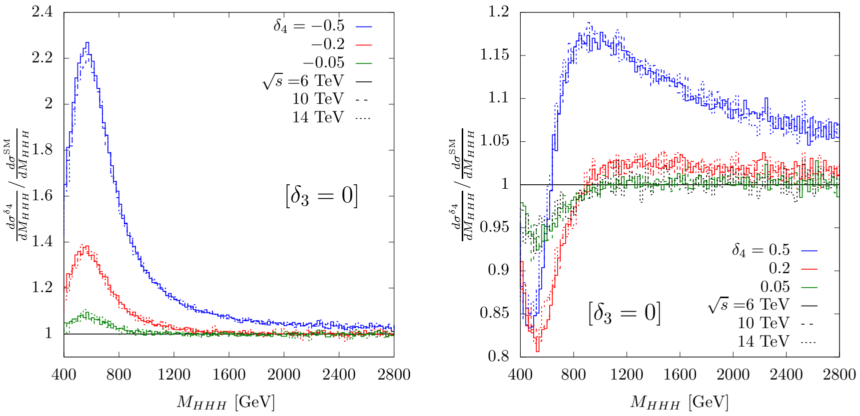

Figure 5.8: Dependence of the M_{HHH} distributions on a variation of the quartic Higgs coupling, for three energy setups, assuming $\delta_3 = 0$ (*i.e.*, a SM trilinear self-coupling).

this case the shape changes are larger at threshold and deviations with respect to SM predictions can be quite significant.

5.3 Sensitivity to the Higgs self-coupling deviations

We are now ready to perform the first exploration of the sensitivity of a future muon collider to deviations of the Higgs self-couplings.

For the sake of simplicity, we restrict the presentation to two possibly relevant scenarios:

A) $\delta_3 = 0$, $\delta_4 \neq 0$, *i.e.*, deviations only in the quartic Higgs coupling;

B) $\delta_4 = 6\,\delta_3$, *i.e.*, the pattern of deviations as expected from the SMEFT at dim=6.

Scenario A assumes that no deviations on the trilinear coupling have been detected (and/or exist) and explores the possibility that new physics effects appear for the first time in the quartic self-coupling. Scenario B, on the other hand, assumes the SMEFT scaling between the two couplings. This scenario would fit the case where a deviation in the trilinear coupling is observed in

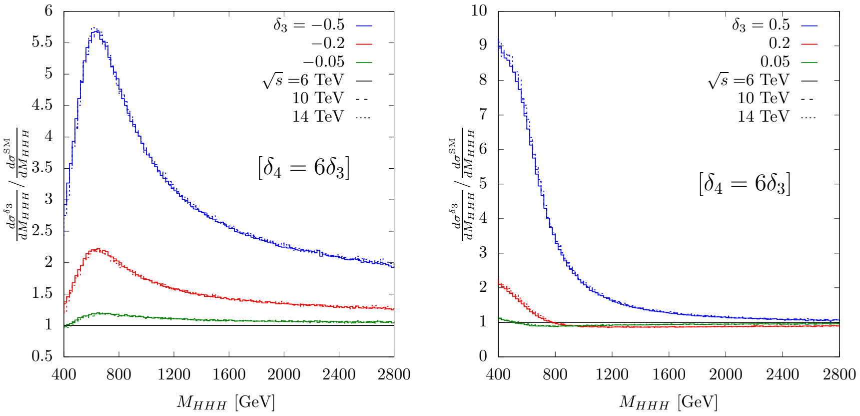

Figure 5.9: Dependence of the M_{HHH} distributions on a variation of the trilinear Higgs coupling, for three energy setups, assuming $\delta_4 = 6\,\delta_3$.

other observables, such as in HH production. In this situation, an interesting question would be whether the deviation in δ_4 would follow the linear SMEFT pattern or not.

To provide a first estimation of the sensitivity, we focus on the signal process $\mu^+\mu^- \to HHH\nu\bar{\nu}$ and disregard possible backgrounds. In so doing, we are clearly setting an optimal target for more detailed future phenomenological and experimental investigations. We define the sensitivity to the non-SM Higgs couplings as:

$$\frac{|N - N_{\rm SM}|}{\sqrt{N_{\rm SM}}}, \tag{5.8}$$

where $N_{\rm SM}$ is the number of events assuming $\delta_3 = \delta_4 = 0$, while N is the number of events obtained for the values of δ_3 and δ_4 under consideration.

In figure 5.10 we show the dependence on δ_4 and δ_3 of the total cross section in two different bins, inclusive and for $M_{HHH} < 1$ TeV, and for the A (left) and B (right) scenarios (under the SM hypothesis), respectively. In both scenarios, one finds that the highest sensitivity comes from the threshold region

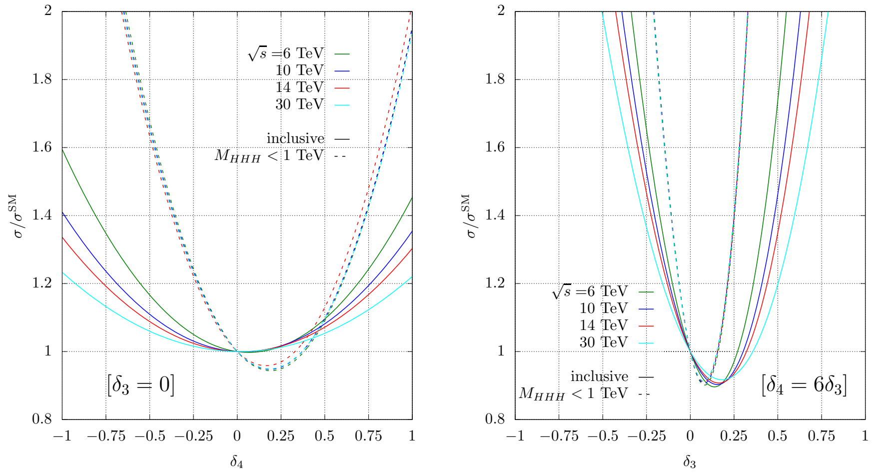

Figure 5.10: Dependence of the $\mu^+\mu^- \to HHH\nu\overline{\nu}$ cross section on the anomalous Higgs self-couplings in two different scenarios: A ($\delta_3 = 0$) on the left and B ($\delta_4 = 6\,\delta_3$) on the right. In the latter case the ratio of the cross sections is expressed in terms of δ_3.

$\sqrt{s}$ (TeV)	Lumi (ab^{-1})	Constraints on δ_4 (with $\delta_3 = 0$) x-sec only 1 σ	 x-sec only 2 σ	 threshold + $M_{HHH} > 1$ TeV 1 σ
6	12	$[-0.60, 0.75]$	$[-0.90, 1.00]$	$[-0.55, 0.85]$
10	20	$[-0.50, 0.55]$	$[-0.70, 0.80]$	$[-0.45, 0.70]$
14	33	$[-0.45, 0.50]$	$[-0.60, 0.65]$	$[-0.35, 0.55]$
30	100	$[-0.30, 0.35]$	$[-0.45, 0.45]$	$[-0.20, 0.40]$
3	100	$[-0.35, 0.60]$	$[-0.50, 0.80]$	$[-0.45, 0.65]$

Table 5.4: Summary of the constraints on the quartic deviations δ_4, assuming $\delta_3 = 0$, for various muon collider energy/luminosity options, as obtained from the total expected cross sections (1σ and 2σ CL). The third column shows the bounds obtained from the combination of the constraints corresponding to the setups $M_{HHH} < 1$ TeV and $M_{HHH} > 1$ TeV.

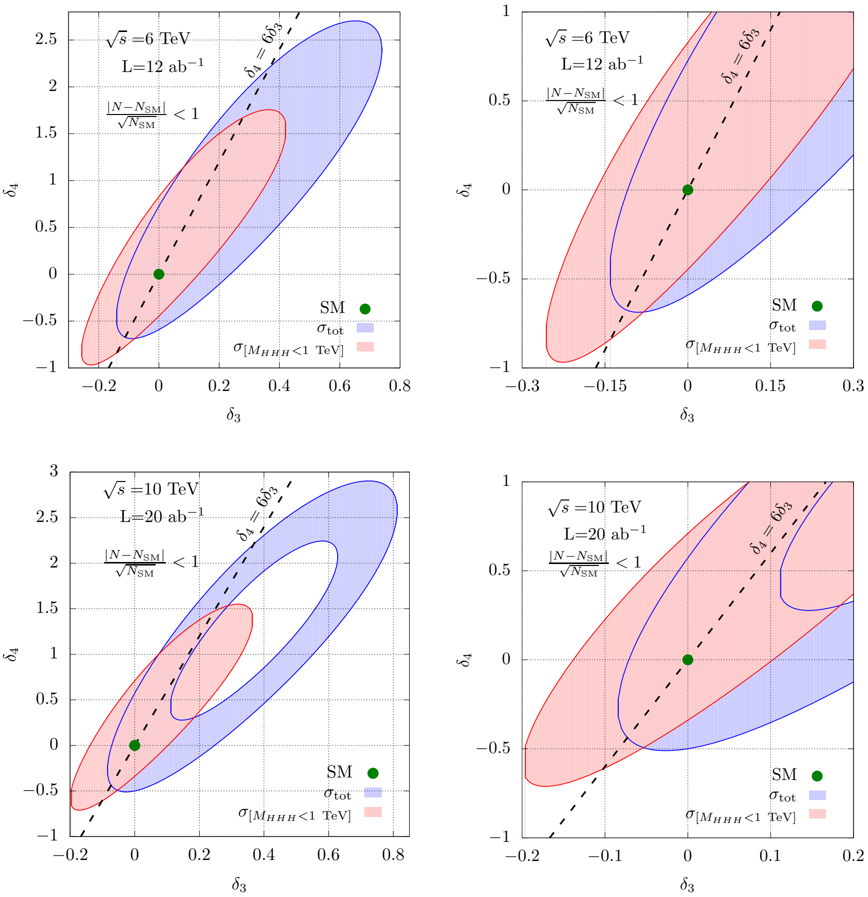

Figure 5.11: Left: 1-σ exclusion plots for the anomalous Higgs self-couplings in terms of the standard deviations $|N - N_{\rm SM}|/\sqrt{N_{\rm SM}}$ from the SM (green dot), where the event numbers N refer either to $\sigma(\mu^+\mu^- \to HHH\nu\bar{\nu})$, for $M_{\bar{\nu}\nu} \gtrsim 150$GeV (blue area), or to the same cross section with an upper cut of 1 TeV on the HHH invariant mass (red area). Right: same plots zoomed around the SM configuration.

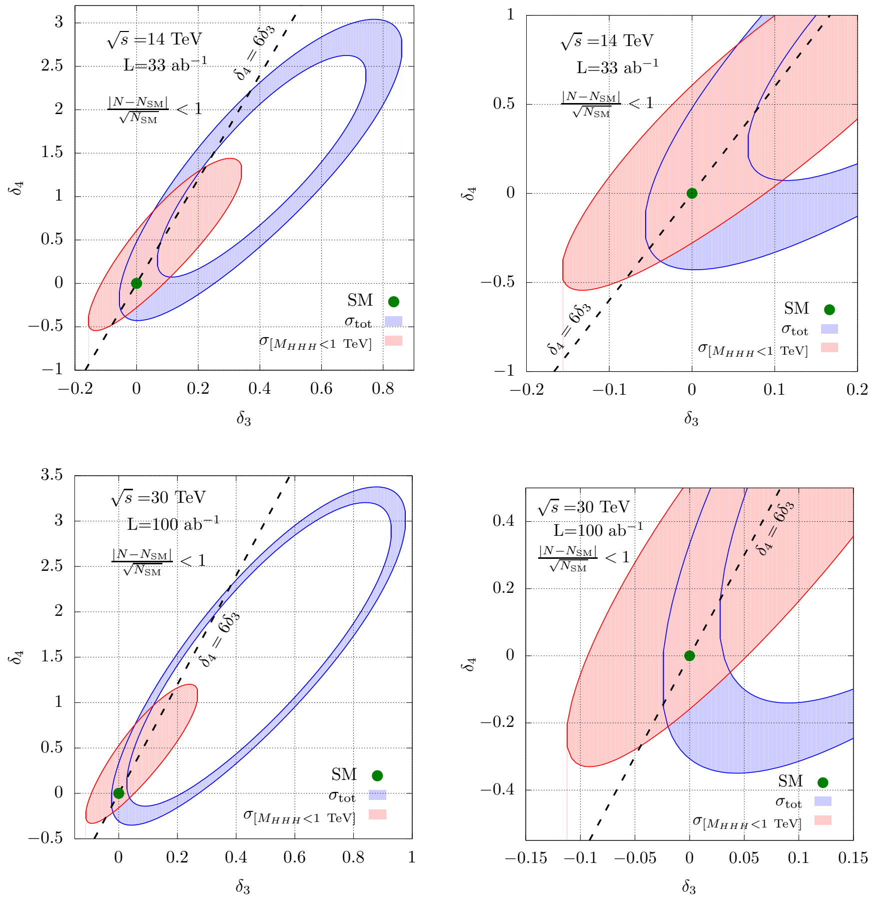

Figure 5.12: Left: 1-σ exclusion plots for the anomalous Higgs self-couplings in terms of the standard deviations $|N - N_{\rm SM}|/\sqrt{N_{\rm SM}}$ from the SM (green dot), where the event numbers N refer either to $\sigma(\mu^+\mu^- \to HHH\nu\overline{\nu})$, for $M_{\bar{\nu}\nu} \gtrsim 150$GeV (blue area), or to the same cross section with an upper cut of 1 TeV on the HHH invariant mass (red area). Right: same plots zoomed around the SM configuration.

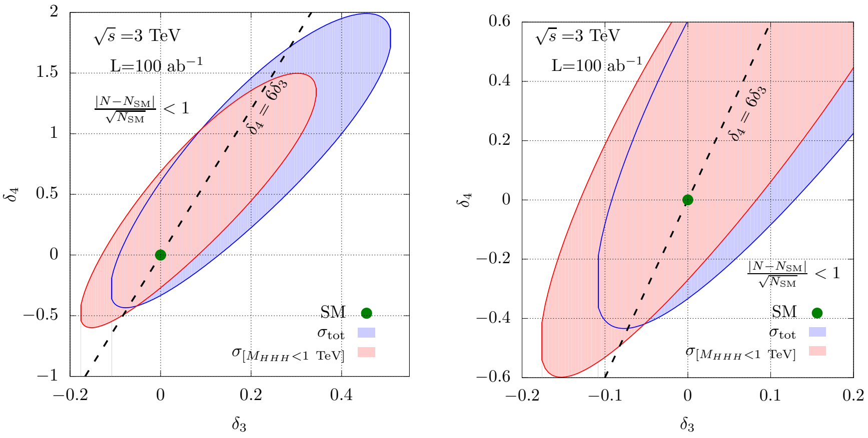

Figure 5.13: Left: 1-σ exclusion plot for the anomalous Higgs self-couplings in terms of the standard deviations $|N - N_{\rm SM}|/\sqrt{N_{\rm SM}}$ from the SM (green dot), where the event numbers N refer either to $\sigma(\mu^+\mu^- \to HHH\nu\overline{\nu})$, for $M_{\bar{\nu}\nu} \gtrsim$ 150GeV (blue area), or to the same cross section with an upper cut of 1 TeV on the HHH invariant mass (red area). Right: same plot zoomed around the SM configuration. The integrated luminosity assumed is about 20 times larger than the reference luminosity in table 5.1.

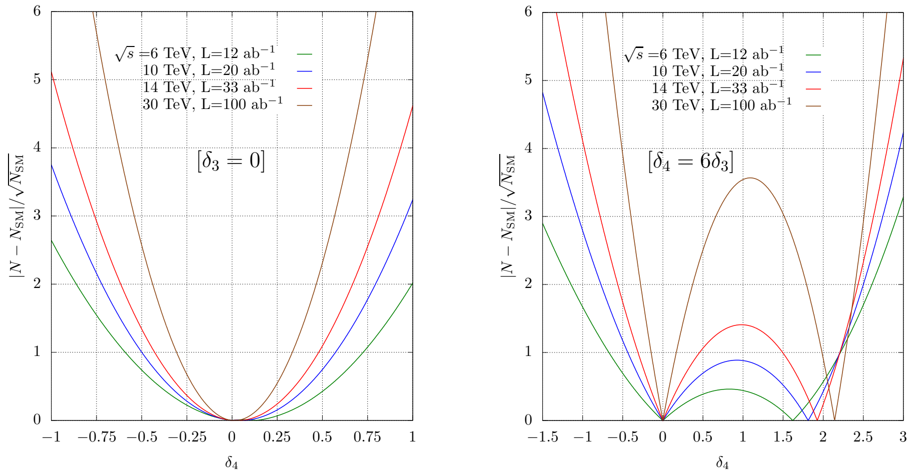

Figure 5.14: Sensitivity to the quartic Higgs self-coupling in terms of standard deviations $|N - N_{\rm SM}|/\sqrt{N_{\rm SM}}$ with respect to the SM configuration, where the event numbers N refer to $\sigma(\mu^+\mu^- \to HHH\nu\overline{\nu})$, for $M_{\bar{\nu}\nu} \gtrsim$ 150GeV, for $\delta_3 = 0$ (left), and $\delta_4 = 6\delta_3$ (right). Results are obtained considering deviations from the inclusive cross sections only.

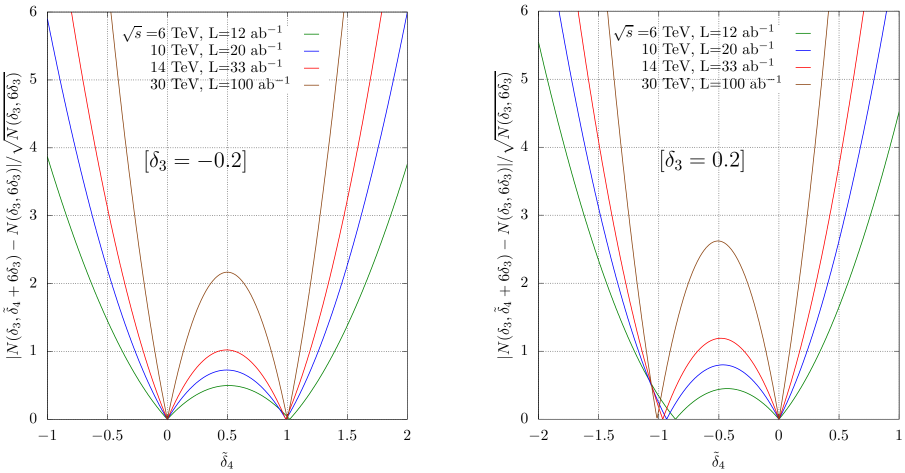

Figure 5.15: Sensitivity to $\tilde{\delta}_4 = \delta_4 - 6\delta_3$ in terms of standard deviations $|N(\delta_3, \tilde{\delta}_4 + 6\delta_3) - N(\delta_3, 6\delta_3)|/\sqrt{N(\delta_3, 6\delta_3)}$ with respect to the SMEFT configuration, where the event numbers N refer to $\sigma(\mu^+\mu^- \to HHH\nu\overline{\nu})$, for $M_{\bar{\nu}\nu} \gtrsim$ 150GeV, for $\delta_3 = -0.2$ (left), and $\delta_3 = 0.2$ (right). Results are obtained considering deviations from the inclusive cross sections only.

and that the energy dependence is actually rather weak on the sensitivity. That means that increasing the energy brings only an advantage in the statistics. The results corresponding to independent variations of δ_3 and δ_4 are shown in figures 5.11, 5.12 and 5.13, where the red shaded areas correspond to the constraints obtained from threshold region, while the blue shaded areas correspond to the full sample. The plots on the right are blowups of the region close to the SM point $(0, 0)$. First, we note that as the energy increases, the blue areas tend to the shape of a ring in the plot range, showing the relevance of the quadratic terms and the fact that bounds are obtained from upper as well as lower limit in the number of events with respect to the SM expectations. As expected from the arguments given above, the constrains improve as the energy/luminosity increase mostly for the blue areas. In addition, the linear flat direction in the case of same sign variations of δ_3 and δ_4 are resolved by using two different regions and the higher terms in the c_i expansion. Figure 5.13 indicates that low energy runs, around 3 TeV, yet with a luminosity of 100 ab^{-1} could provide a determination in the range $-0.3 < \delta_4 < 0.6$ (with $\delta_3 = 0$). Finally, figure 5.14 presents the sensitivity in terms of number of standard deviations.

The constraints that can be obtained from the various energy/luminosity scenarios by using only information on the total cross section at 1σ and 2σ and by combining events in the regions $M_{HHH} < 1$ TeV and $M_{HHH} > 1$ TeV (1σ) are summarized in table 5.4.

The underlying assumption for the setup $\delta_3 = 0$ is that no deviations are measured from the SM triple Higgs self-coupling. However, if the study of HH production at the muon collider or at other machines would discover deviations from $\delta_3 = 0$, it would be interesting to search for possible deviations of δ_4 from its expectation value in the SMEFT ($\tilde{\delta}_4 = \delta_4 - 6\delta_3$). As an example, plots in figure 5.15 show the sensitivity to $\tilde{\delta}_4$ under the assumptions $\delta_3 = \mp 0.2$.

6 Conclusions

In this thesis, we have explored the feasibility of constraining the Higgs potential at present and future colliders. In this concluding chapter, we summarize the main results achieved and make some comments on further avenues of research.

Firstly, we have considered the potential of hadron colliders. Many studies exist on the perspectives to measure the cubic Higgs self-coupling at LHC and future hadron colliders, and it is expected that a precision at a few percent level could be reached at the FCC running at 100 TeV. However, the final precision of the LHC on κ_3 is still to be assessed. Going beyond the common approach of extracting the trilinear from the measurement of the HH final state, we have considered the possibility of setting constraints on κ_3 through one-loop corrections to single Higgs processes at the LHC. We have provided an MC tool to simulate such effects at differential level, and we have also examined the effects of the SM NLO EW corrections. By performing a fit for κ_3 based on a future projection at 14 TeV LHC, we examined the impact of different information on the constraints of κ_3. We have also examined the feasibility of measuring the Higgs quartic self-coupling directly via gluon fusion into triple Higgs boson. We have performed a detailed analysis, including detector effects and backgrounds. Our findings are in line with the current lore, *i.e.* that the backgrounds are so huge that even at a future 100 TeV hadron collider such a measurement would be extremely challenging. Because of this, we have explored the potential of constraining the quartic using indirect constraints, by considering higher order correction to gluon fusion into Higgs boson pair. The corrections of Higgs quartic self-coupling start from the two-loop level and it is a very challenging computation. We have evaluated the relevant two-loop Feynman integrals with numerical methods. By considering the constraints based on $b\bar{b}\gamma\gamma$ decay channel, we have shown that the constraints are complementary and competitive to direct measurement of triple Higgs processes.

Next, we have moved on to future electron-positron colliders. We have considered single-, double-, and triple-Higgs processes, and including one-loop corrections induced by the Higgs self-couplings to single- and double-Higgs production. The potential of future circular as well as linear e^+e^- colliders has been investigated. We have concluded that for the trilinear Higgs self-coupling, the best constraints can be obtained from the combination of ZH results at low-energy high-luminosity runs and double Higgs processes at high energy runs. For the quartic Higgs self-coupling, we identified the indirect constraints from double Higgs production and direct constraints from triple Higgs production as the most promising avenues. We have also found that although WBF HH constraints are in general stronger than those for ZHH, the two production processes are complementary and lead to improved results when they are combined. While triple Higgs production is not measurable in the SM, its cross section strongly depends on the Higgs quartic self-couplings, and at CLIC 3TeV, the constraints via WBF HHH are comparable to those at a future 100 TeV hadron collider.

Finally, we have considered a futuristic multi-TeV muon collider. At such high energy, the cross section of WBF HHH increases significantly, and becomes measurable even in the SM. We have considered WBF HHH in detail, studying the sensitivity of total rates as well as distributions on the Higgs boson self-couplings. We have found the most sensitive region to be at threshold, while the high-energy tail provides more statistics. Under very simplifying assumptions, we determined the limits on the cubic and quartic couplings under various possible energy/luminosiy configurations. We found that with several TeV of center of mass energy and several tens of attobarns integrated luminosity, the quartic Higgs self-coupling can be determined with an accuracy in the tens of percent. For example, at 14 TeV with $33\,\mathrm{ab}^{-1}$ integrated luminosity, one could constraint κ_4 with a 50% uncertainty at 1σ, which is significantly better than a hadron collider or an e^+e^- collider.

A Form factors

In this section we provide all the form factors that are necessary for the calculations of one-loop amplitudes for ZHH and WBF HH production entering $\sigma_{\rm NLO}^{\rm pheno}$ in eq. (4.16). Those form factors are also used in calculating the one-loop correction to single Higgs production in Sec. 3.1, and the factorisable contribution to two-loop amplitude of $gg \to HH$ in Sec. 3.3. These are the form factors for the

- HVV vertex $V[HVV]$,
- HHH vertex $V[HHH]$,
- $HHVV$ vertex $V[HHVV]$,
- H propagator $P[HH]$.

We include contributions up to the order $(v/\Lambda)^6$ and therefore one-loop amplitudes entering $\sigma_{\rm NLO}^{\rm pheno}(HH)$ can be obtained by substituting the vertexes in the corresponding tree-level amplitudes with the aforementioned form factors. Indeed, we implemented them in a UFO [61] model file and performed the calculation within the MADGRAPH5_AMC@NLO [62] framework, as also done in ref. [107]. We cross-checked the results via FEYNARTS 3.9 [113] and FORMCALC 9.4 [63]. Loops integrals have been evaluated with LOOPTOOLS 2.13 [63] and QCDLOOP 2.0.3 [114, 115].

The HVV form factor is the only one that is also relevant for the calculation of one-loop amplitudes entering $\sigma_{\rm NLO}^{\rm pheno}(H)$ for single Higgs production. For this kind of processes the $(\bar{c}_6)^2$ dependence originates completely from $\delta Z_H^{\rm NP}$ in eq. (2.27), while the linear term in $\bar{c}_6$ comes from both $\delta Z_H^{\rm NP}$ and the HVV

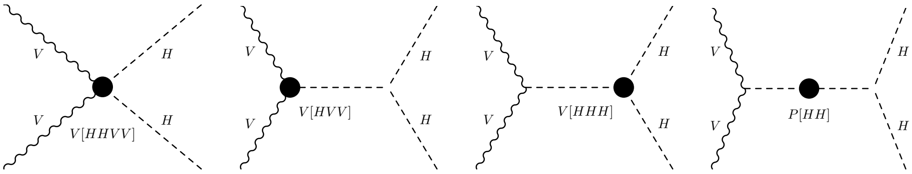

Figure A.1: The structure of one-loop effects in the $HHVV$ amplitude expressed via form factors.

form factor, which has already been calculated in ref. [57] and induces the C_1 dependence on the kinematics. We repeated the calculation explicitly checking the gauge invariance, both for a generic R_ξ gauge and also in unitary gauge.

Before providing the expressions for the different form factors we want to briefly show how the calculation of the σ_{30}, σ_{40}, σ_{01}, σ_{11} and σ_{21} terms, which are part of $\sigma_{\rm NLO}^{\rm pheno}(HH)$, can be organised. As said, the form factors provided in the following can be plugged into the tree-level diagrams in order to get the necessary one-loop amplitudes for ZHH and WBF HH giving $\sigma_{\rm NLO}^{\rm pheno}(HH)$. This is schematically depicted in Fig. A.1, where the relevant part of the ZHH and WBF HH amplitudes, respectively $W^*W^* \to HH$ or $Z^* \to HHZ$, is shown. Via the interference of tree-level amplitudes and such one-loop amplitudes obtained via form factors, we would get a cross section that we denote as $\sigma^{\rm FF}$, where FF stands for form-factors. It is important to note that $\sigma^{\rm FF}$ contains also $\bar{c}_6$- and $(\bar{c}_6)^2$-dependent spurious terms, which have to be discarded. One can easily expand in powers of $\bar{c}_6^i \bar{c}_8^j$ the $\sigma^{\rm FF}$ result and identify the different $\sigma_{ij}^{\rm FF}$ component.

We should note that for consistency we provide the form factor of HVV matching the same convention used in ref. [57], *i.e.*, without including the contribution of the Higgs wave-function counterterm $\delta Z_H^{\rm NP}$. The same convention is used also for all the other form-factors. Note that in the case of the H propagator and HHH vertex, UV divergences are present in the terms relevant for our calculation and thus the other UV counterterms have to be included in the definition of the form-factors.

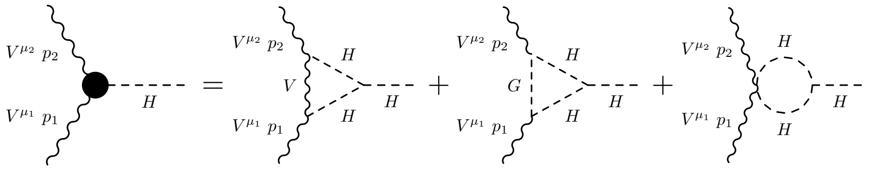

(A.3)

Figure A.2: Feynman diagrams contributing to the $V[HVV]$ form factor at one loop.

HVV-vertex

The HVV form factor, which will denote as $V[HVV]$, enters both the single and double Higgs production calculation and can be written as

$$V^{\mu_1\mu_2}[HVV] = V_0^{\mu_1\mu_2}[HVV] + V_1^{\mu_1\mu_2}[HVV]\bar{c}_6\,. \qquad \text{(A.1)}$$

For our calculation the $\bar{c}_6$-independent part can be ignored, while in a generic gauge $V_1[HVV]$ is given by the three diagrams [1] in Fig. A.2. Using the convention that the corresponding Feynman rule is $iV^{\mu_1\mu_2}[HVV]$, as we will do also for the other form factors, we can write $V_1^{\mu_1\mu_2}[HVV]$ as

$$V_1^{\mu_1\mu_2}[HVV] = \frac{\lambda m_V^2}{16\pi^2 v} T^{\mu_1\mu_2}(p_1, p_2, m_V, m_H)\,. \qquad \text{(A.2)}$$

In particular

$$T^{\mu_1\mu_2}(p_1, p_2, m_V, m_H) = (-6B_0 - 24m_V^2 C_0 + 24C_{00})g^{\mu_1\mu_2} - 24p_1^{\mu_2}p_2^{\mu_1}C_{12}\,, \qquad \text{(A.4)}$$

where p_1, p_2 are the (incoming) momenta of the two vector bosons, μ_1, μ_2 are the corresponding Lorentz indices, m_V with $V = W, Z$ is mass of the vector bosons, and B_0, C_0, C_{00}, C_{12} are one-loop scalar/tensor integrals defined according to the notation used, *e.g.*, in ref. [2] and where the following variables

---

[1] In the unitary gauge the second diagram does not appear

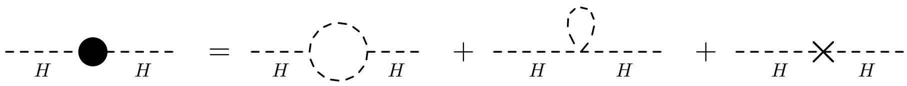

(A.9)

Figure A.3: Feynman diagrams contributing to $P[HH]$.

are understood:

$$B_0 = B_0((p_1+p_2)^2, m_H^2, m_H^2)\,, \tag{A.5}$$

$$C_{0,00,12} = C_{0,00,12}(p_1^2, (p_1+p_2)^2, p_2^2, m_V^2, m_H^2, m_H^2)\,. \tag{A.6}$$

We remind the reader that the $\frac{1}{2}\delta Z_H^{\rm NP}$ contribution from the external H has been removed from $V[HVV]$.

H propagator

The form factors for the HH two point function, which we denote as $P[HH]$, receives one-loop contributions from the diagrams in Fig. A.3, where the contribution of counterterm diagram is given in eq. (2.25). At one loop $P[HH]$ can be written as

$$P[HH] = P_{00}[HH] + P_{10}[HH]\bar{c}_6 + P_{20}[HH]\bar{c}_6^2\,. \tag{A.7}$$

In our calculation we do not include $P_{00}[HH]$ contributions, which we set to zero, while $P_{10}[HH]$ and $P_{20}[HH]$ read

$$P_{10}[HH] = 2P_{20}[HH] = \frac{1}{16\pi^2}(6\lambda v)^2\left[B_0(p^2, m_H^2, m_H^2) - B_0(m_H^2, m_H^2, m_H^2)\right]\,, \tag{A.8}$$

It is important to note that $P(HH)$ does not depend on $\bar{c}_8$. Indeed, although the second diagram, the seagull, depends on $\bar{c}_8$ due to the $HHHH$ vertex, it is exactly cancelled by the Higgs-mass counter term. We remind the reader that the $-\delta Z_H^{\rm NP}$ component in the counterterm has been removed from $P[HH]$.

HHH-vertex form factor

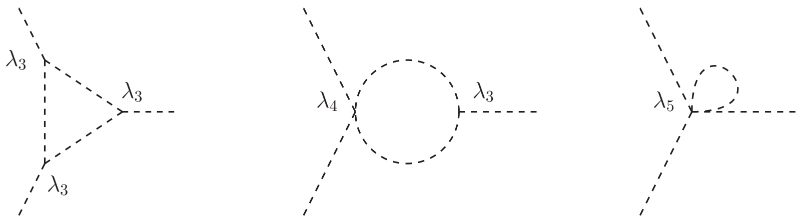

Figure A.4: Feynman Diagrams contributing to the HHH form factors at one loop.

The form-factor for the HHH vertex, $V[HHH]$, receives contributions from the diagrams shown in the main text in Fig. A.4 and the counter term of Fig. 2.1. At variance with $V[HVV]$ and $P[HH]$, $V[HHH]$ depends on both $\bar{c}_6$ and $\bar{c}_8$:

$$V[HHH] = \sum_{i+2j\leq 3} V_{ij}[HHH]\bar{c}_6^i\bar{c}_8^j \, . \tag{A.10}$$

For our calculation $V_{00}[HHH]$ and $V_{10}[HHH]$ can be set equal to zero, while

$$V_{30}[HHH] = \frac{1}{16\pi^2}(6\lambda v)^3 C_0(p_1^2, p_2^2, p_3^2, m_H^2, m_H^2, m_H^2)\,, \tag{A.11}$$

$$V_{20}[HHH] = \frac{1}{16\pi^2}(6\lambda v)^3 3C_0(p_1^2, p_2^2, p_3^2, m_H^2, m_H^2, m_H^2),\,, \tag{A.12}$$

$$+ \frac{1}{16\pi^2} 108\lambda^2 v \left\{ -\frac{1}{2}[B_0(m_H^2, m_H^2, m_H^2) - \Delta] \right. \tag{A.13}$$

$$\left. + \sum_{i=1}^{3} [B_0(p_i^2, m_H^2, m_H^2) - \Delta] \right\}\,,$$

$$V_{01}[HHH] = \frac{\lambda v}{16\pi^2} \left\{ 18\lambda \left[\sum_{i=1}^{3} [B_0(p_i^2, m_H^2, m_H^2) - \Delta] \right] \right. \tag{A.14}$$

$$- 6 \left[\frac{N_c m_t^2}{v^2} \Delta + 16\pi^2 \frac{\delta v}{v} \right] + 21 \frac{A_0(m_H^2) - m_H^2 \Delta}{v^2} \tag{A.15}$$

$$\left. + 3 \frac{A_0(\xi_Z m_Z^2) + 3m_Z^2 \Delta}{v^2} + 6 \frac{A_0(\xi_W m_W^2) + 3m_W^2 \Delta}{v^2} \right\},$$

$$V_{11}[HHH] = \frac{\lambda v}{16\pi^2} 18\lambda \left[\sum_{i=1}^{3} [B_0(p_i^2, m_H^2, m_H^2) - \Delta] \right]\,, \tag{A.16}$$

where the B_0 and C_0 are the loop scalar integrals, with the dependence on external momenta and internal masses expressed with the convention in ref. [2]. The term Δ is the UV divergence as defined in Section 2.1. The $V_{30}[HHH]$ component is equivalent to the result of ref. [92], where it is assumed $V[HHH] \sim (1 + \bar{c}_6)^3 V_{30}[HHH]$. It should be noticed that the contribution of δv, which as discussed in Section 2.1 is completely of SM origin, is necessary in order to obtain UV finiteness and gauge-invariance for the finite results. We kept the explicit dependence on the ξ gauge parameters outside δv precisely to make this point manifest. In order to help the reader we report in the following the UV divergent part of δv and the ξ-dependent part, which includes both finite and divergent contributions

$$(\delta v)^{\text{UV}} = (\delta v^{\text{SM}})^{\text{UV}} = \frac{\Delta}{16\pi^2} \left[\frac{1}{2} \frac{(3 + \xi_Z) m_Z^2 + 2(3 + \xi_W) m_W^2}{v} - \frac{N_c m_t^2}{v} \right], \tag{A.17}$$

$$(\delta v)_\xi = (\delta v^{\text{SM}})_\xi = \frac{1}{16\pi^2} \frac{1}{2v} \left[A_0(m_Z^2 \xi_Z) + 2A_0(m_W^2 \xi_W) \right]\,. \tag{A.18}$$

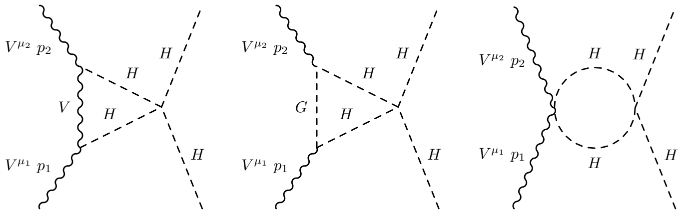

Figure A.5: Feynman diagrams contributing to the $V_{01}[HHVV]$ form factor.

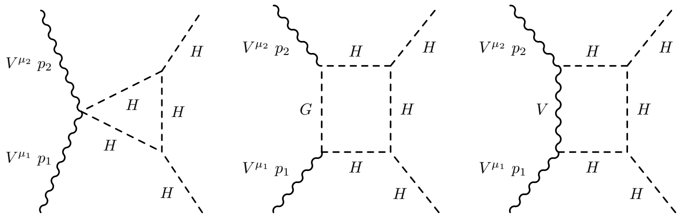

Figure A.6: Representative Feynman diagrams contributing to the $V_{20}[HHVV]$ form factor.

We remind the reader that the $\frac{3}{2}\delta Z_H^{\mathrm{NP}}$ component in the counterterm, which originates from the three H external legs, has been removed from $V[HHH]$.

HHVV-vertex form factor

Similarly to the case of $V[HHH]$, the form factor for the $HHVV$ vertex, $V[HHVV]$, can be written as

$$V[HHVV] = \sum_{i+2j\leq 2} V_{ij}[HHVV]\bar{c}_6^i \bar{c}_8^j \,. \tag{A.19}$$

For our calculation only $V_{20}[HHVV]$ and $V_{01}[HHVV]$ are relevant and we set the other contributions to zero. The $V_{01}[HHVV]$ component originates from the diagrams in Fig. A.5 and its structure is very similar to the one of $V_1[HVV]$,

$$V_{01}^{\mu_1\mu_2}[HHVV] = \frac{\lambda m_V^2}{16\pi^2 v^2} T^{\mu_1\mu_2}(p_1, p_2, m_V, m_H)\,, \tag{A.20}$$

where all momentum are incoming and $T^{\mu_1\mu_2}$ is given in eq. (A.4). The $V_{20}[HHVV]$ term instead originates from the diagrams in Fig. A.6, which include boxes and thus they involve a much more complex kinematic dependence,

$$\begin{aligned} V_{20}^{\mu_1\mu_2}[HHVV] =& 9\frac{\lambda^2 m_V^2}{\pi^2}[F^{\mu_1\mu_2}(p_1,p_2,p_3,p_4,m_V,m_H) \\ &+ F^{\mu_1\mu_2}(p_1,p_2,p_4,p_3,m_V,m_H)]\,, \end{aligned} \tag{A.21}$$

where $F^{\mu_1\mu_2}$ is given by

$$\begin{aligned} F^{\mu_1\mu_2}(p_1,p_2,p_3,p_4,m_V,m_H) =& (-\frac{1}{4}C_0 - m_V^2 D_0 + D_{00})g^{\mu_1\mu_2} + p_4^{\mu_1}p_1^{\mu_2}D_{12} \\ &+ p_4^{\mu_1}(p_1+p_4)^{\mu_2}D_{22} - p_2^{\mu_1}p_1^{\mu_2}D_{13} \\ &- p_2^{\mu_1}(p_1+p_4)^{\mu_2}D_{23}\,, \end{aligned} \tag{A.22}$$

with the dependence on external momenta and internal masses of C and D functions as

$$C_0 = C_0((p_3+p_4)^2, p_3^2, p_4^2, m_H^2, m_H^2, m_H^2)\,, \tag{A.23}$$

$$D_{i(j)} = D_{i(j)}(p_1^2, p_4^2, p_3^2, p_2^2, (p_1+p_4)^2, (p_4+p_3)^2, m_V^2, m_H^2, m_H^2, m_H^2)\,, \tag{A.24}$$

according to the convention of ref. [2]. Both $V_{01}[HHVV]$ and $V_{20}[HHVV]$ are UV finite and gauge-invariant. We remind the reader that the δZ_H^{NP} component in the counterterm, which originates from the two H external legs, has been removed from $V[HHVV]$.

B Perturbative limits

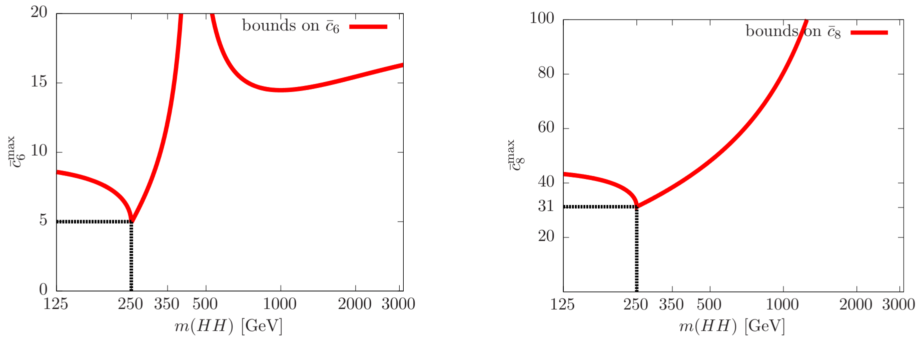

Figure B.1: Maximum value of $\bar{c}_6$ (left) and $\bar{c}_8$ (right) such that the one-loop corrections to the HHH amplitude are smaller than its tree-level value. We consider two Higgs bosons on-shell and the third with virtuality equal to $m(HH)$, showing the dependence on $m(HH)$.

In this section we describe how we derived the range of validity of our calculation,

$$|\bar{c}_6| < 5 \;\text{ and }\; |\bar{c}_8| < 31\,, \tag{B.1}$$

which has already mentioned several times in the text.

First of all, we analyse the one-loop $H^* \to HH$ amplitude, the analytical expression of which can be obtained via δZ_H^{NP} and the form factors $P[HH]$ and the $V[HHH]$ that have been provided in the previous section. We define as $\bar{c}_6^{\max}(\bar{c}_8^{\max})$ the value of $\bar{c}_6(\bar{c}_8)$ such that the one-loop amplitude is as large as the tree-level one, *i.e.* the value of of $\bar{c}_6(\bar{c}_8)$ from where perturbative convergence cannot be trusted anymore. For the estimation of $\bar{c}_6^{\max}$ we take into

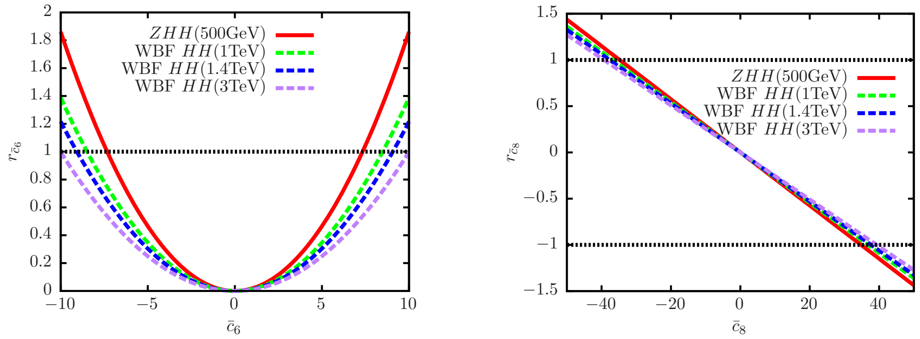

Figure B.2: $\bar{c}_6$-dependence of $r_{\bar{c}_6}$ (left) and $\bar{c}_8$-dependence of $r_{\bar{c}_8}$ (right) for ZHH and WBF HH at different energies.

account the leading contribution from V_{30} and P_{20}, both yielding $\bar{c}_6^3$ terms. For $\bar{c}_8^{\max}$ we instead consider as first step the contribution from V_{11}, which is the dominant term when $\bar{c}_6$ is large, and we compare it with the linearly $\bar{c}_6$ dependent part of the tree-level vertex. In such a way the value of $\bar{c}_8^{\max}$ is independent on $\bar{c}_6$.

The value of $\bar{c}_6^{\max}(\bar{c}_8^{\max})$ has a kinematic dependence. In the left plot of Fig. B.1 we display the dependence of $\bar{c}_6^{\max}$ on $m(HH)$, ranging from 125 GeV to 3 TeV. The equivalent plot for $\bar{c}_8^{\max}$, taking leading term in $\bar{c}_6$, is shown on the right. Thus, we explore $m(HH)$ values both below the production threshold and in the tail of the $m(HH)$ distributions. As can be seen in both cases, the most stringent constraints, $|\bar{c}_6| < 5$ and $|\bar{c}_8| < 31$, arise from the threshold condition $m(HH) = 2m_H$, while for different values of $m(HH)$ the bound is weaker.

In the case of $\bar{c}_6^{\max}$ the constraint is independent on the value of the renormalisation scale μ_r and compatible with the result obtained in ref. [92], where the subdominant contribution of P_{20} was not taken into account. Conversely, in the case of $\bar{c}_8^{\max}$ the constraint does depend on the value of the renormalisation scale μ_r. However, we verified for $\mu_r = m_H, 4m_H$, that the most stringent $\bar{c}_8^{\max}$ value is anyway arising from the kinematic condition $m(HH) = 2m_H$.

The constraints of eq. (B.1) have been derived via the analysis of the $H^* \to HH$ amplitude. On the other hand, for ZHH and WBF HH we also have the HVV and $HHVV$ vertexes contribute via loop corrections to the quantity $\sigma_{\rm NLO}^{\rm pheno}$, eq. (4.16), Thus, it is important to check if they can affect the results of eq. (B.1). To this purpose we directly considered the quantities

$$\begin{aligned} r_{\bar{c}_6} &\equiv \frac{\bar{c}_6^4\sigma_{40}}{\bar{c}_6^2\sigma_2} = \frac{\sigma_{40}}{\sigma_2}\bar{c}_6^2\,, \\ r_{\bar{c}_8} &\equiv \frac{\sigma_{21}\bar{c}_6^2\bar{c}_8}{\sigma_2\bar{c}_6^2} = \frac{\sigma_{21}}{\sigma_2}\bar{c}_8\,, \end{aligned} \tag{B.2}$$

for $ZHHH$ and WBF HH at different energies. The quantity $r_{\bar{c}_6}$ is the ratio between the term with the highest power in $\bar{c}_6$ from $\Delta\sigma_{\bar{c}_6}$ and the one with the highest power in $\bar{c}_6$ from $\sigma_{\rm LO}$, *i.e.*, the ratio of the dominant contributions at tree and one-loop level for large $\bar{c}_6$ values. Similarly, the quantity $r_{\bar{c}_8}$ is the ratio between the term with the highest power in $\bar{c}_6$ from $\Delta\sigma_{\bar{c}_8}$ and $\sigma_{\rm LO}$. Thus, both of them can be considered as a generalisation of the first step; both HVV and $HHVV$ vertices are taken into account and phase-space integration is performed.

In the left plot of Fig. B.2, we show $r_{\bar{c}_6}$ for the case of ZHH at 500 GeV and of WBF at $1, 1.4$ and 3 TeV, which are the phenomenologically relevant scenarios analysed in sec. 4.2. Requiring $|r_{\bar{c}_6}| < 1$, we can get $|\bar{c}_6| < 8$ for ZHH at 500 GeV, and $|\bar{c}_6| < 9, 10, 11$ for WBF HH at 1000, 1400 and 3000 GeV, respectively. Thus, as one would expected from Fig. B.1 for the $H^* \to HH$ vertex, at higher energies, far from the production threshold, limits are weaker. In the right plot we show $r_{\bar{c}_8}$ for the same energies an process. Also in this case the obtained limits are weaker than in eq. (B.1), $|\bar{c}_8| <\sim 35 - 40$.

C Cut efficiency

In this section we explicitly write the cuts used in our analysis of $gg \to HH \to b\bar{b}\gamma\gamma$(Section 3.3). The cuts are the same of Ref. [22], on which our analysis is based. Specifically, at 14 TeV, they correspond to

$$p_T(b_1) > 50 \text{ GeV}, \qquad p_T(b_2) > 30 \text{ GeV}\,, \tag{C.1}$$

$$p_T(\gamma_1) > 50 \text{ GeV}, \qquad p_T(\gamma_2) > 30 \text{ GeV}\,, \tag{C.2}$$

$$|\eta(b)| < 2.5, \qquad |\eta(\gamma)| < 2.5\,, \tag{C.3}$$

$$0.5 < \Delta R(b,b) < 2, \qquad \Delta R(\gamma,\gamma) < 2\,, \tag{C.4}$$

$$\Delta R(b,\gamma) > 1.5\,, \tag{C.5}$$

while at 100 TeV, the p_T cuts are replaced by:

$$p_T(b_1) > 60 \text{ GeV}, \qquad p_T(b_2) > 40 \text{ GeV}\,, \tag{C.6}$$

$$p_T(\gamma_1) > 60 \text{ GeV}, \qquad p_T(\gamma_2) > 40 \text{ GeV}\,. \tag{C.7}$$

In fig. C.1, we show the differential cut efficiency for the signal, assuming SM double Higgs production and narrow-width approximation. In other words, we plot the ratio between the number of events predicted in the SM with and without the cuts as function of $m(HH)$. Since spin-0 contributions dominate for both SM and BSM cases, cut efficiencies for BSM cases are very similar.

The zero efficiency in the 250 GeV $< m(HH) <$ 300 GeV phase-space region is not a surprise; when Higgs boson pairs are produced at the threshold, both the $b\bar{b}$ and $\gamma\gamma$ pairs from the Higgs decays are back-to-back and therefore rejected by the cuts $\Delta R(b,b) < 2$ and $\Delta R(\gamma,\gamma) < 2$. Increasing the energy, both Higgs bosons can have non-vanishing transverse momentum and therefore their decay products can be not back-to-back. For very high ener-

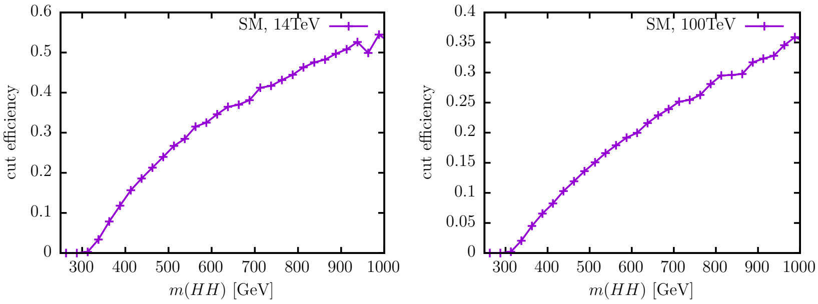

Figure C.1: Differential cut efficiency for SM double-Higgs signal from the $b\bar{b}\gamma\gamma$ signature, at parton level.

gies, their decay products tend to be collimated and lead to much higher cut efficiency.

Bibliography

[1] C.-Y. Chen, S. Dawson and I. M. Lewis, *Exploring resonant di-Higgs boson production in the Higgs singlet model*, *Phys. Rev.* **D91** (2015) 035015 [`1410.5488`].

[2] A. Denner, *Techniques for calculation of electroweak radiative corrections at the one loop level and results for W physics at LEP-200*, *Fortsch. Phys.* **41** (1993) 307 [`0709.1075`].

[3] A. Sirlin and R. Zucchini, *Dependence of the Quartic Coupling H(m) on M(H) and the Possible Onset of New Physics in the Higgs Sector of the Standard Model*, *Nucl. Phys.* **B266** (1986) 389.

[4] J. Alison et al., *Higgs Boson Pair Production at Colliders: Status and Perspectives*, in *Double Higgs Production at Colliders Batavia, IL, USA, September 4, 2018-9, 2019*, B. Di Micco, M. Gouzevitch, J. Mazzitelli and C. Vernieri, eds., 2019, `1910.00012`, https://lss.fnal.gov/archive/2019/conf/fermilab-conf-19-468-e-t.pdf.

[5] E. W. N. Glover and J. J. van der Bij, *HIGGS BOSON PAIR PRODUCTION VIA GLUON FUSION*, *Nucl. Phys.* **B309** (1988) 282.

[6] T. Plehn, M. Spira and P. M. Zerwas, *Pair production of neutral Higgs particles in gluon-gluon collisions*, *Nucl. Phys.* **B479** (1996) 46 [`hep-ph/9603205`].

[7] S. Borowka, N. Greiner, G. Heinrich, S. P. Jones, M. Kerner, J. Schlenk et al., *Higgs Boson Pair Production in Gluon Fusion at Next-to-Leading Order with Full Top-Quark Mass Dependence*, *Phys. Rev. Lett.* **117** (2016) 012001 [`1604.06447`].

[8] S. Borowka, N. Greiner, G. Heinrich, S. P. Jones, M. Kerner, J. Schlenk et al., *Full top quark mass dependence in Higgs boson pair production at NLO*, *JHEP* **10** (2016) 107 [`1608.04798`].

[9] J. Baglio, F. Campanario, S. Glaus, M. Mühlleitner, M. Spira and J. Streicher, *Gluon fusion into Higgs pairs at NLO QCD and the top mass scheme*, *Eur. Phys. J.* **C79** (2019) 459 [1811.05692].

[10] R. Frederix, S. Frixione, V. Hirschi, F. Maltoni, O. Mattelaer, P. Torrielli et al., *Higgs pair production at the LHC with NLO and parton-shower effects*, *Phys. Lett.* **B732** (2014) 142 [1401.7340].

[11] G. Heinrich, S. P. Jones, M. Kerner, G. Luisoni and E. Vryonidou, *NLO predictions for Higgs boson pair production with full top quark mass dependence matched to parton showers*, *JHEP* **08** (2017) 088 [1703.09252].

[12] S. Jones and S. Kuttimalai, *Parton Shower and NLO-Matching uncertainties in Higgs Boson Pair Production*, *JHEP* **02** (2018) 176 [1711.03319].

[13] D. de Florian and J. Mazzitelli, *Higgs Boson Pair Production at Next-to-Next-to-Leading Order in QCD*, *Phys. Rev. Lett.* **111** (2013) 201801 [1309.6594].

[14] J. Grigo, K. Melnikov and M. Steinhauser, *Virtual corrections to Higgs boson pair production in the large top quark mass limit*, *Nucl. Phys.* **B888** (2014) 17 [1408.2422].

[15] J. Grigo, J. Hoff and M. Steinhauser, *Higgs boson pair production: top quark mass effects at NLO and NNLO*, *Nucl. Phys.* **B900** (2015) 412 [1508.00909].

[16] D. de Florian, M. Grazzini, C. Hanga, S. Kallweit, J. M. Lindert, P. Maierhöfer et al., *Differential Higgs Boson Pair Production at Next-to-Next-to-Leading Order in QCD*, *JHEP* **09** (2016) 151 [1606.09519].

[17] M. Grazzini, G. Heinrich, S. Jones, S. Kallweit, M. Kerner, J. M. Lindert et al., *Higgs boson pair production at NNLO with top quark mass effects*, *JHEP* **05** (2018) 059 [1803.02463].

[18] U. Baur, T. Plehn and D. L. Rainwater, *Probing the Higgs selfcoupling at hadron colliders using rare decays*, *Phys. Rev.* **D69** (2004) 053004 [hep-ph/0310056].

[19] J. Baglio, A. Djouadi, R. Gröber, M. M. Mühlleitner, J. Quevillon and M. Spira, *The measurement of the Higgs self-coupling at the LHC: theoretical status*, *JHEP* **04** (2013) 151 [1212.5581].

[20] W. Yao, *Studies of measuring Higgs self-coupling with* $HH \to b\bar{b}\gamma\gamma$ *at the future hadron colliders*, in *Proceedings, 2013 Community Summer Study on the Future of U.S. Particle Physics: Snowmass on the Mississippi (CSS2013):*

Minneapolis, MN, USA, July 29-August 6, 2013, 2013, `1308.6302`, http://www.slac.stanford.edu/econf/C1307292/docs/submittedArxivFiles/1308.6302.pdf.

[21] V. Barger, L. L. Everett, C. B. Jackson and G. Shaughnessy, *Higgs-Pair Production and Measurement of the Triscalar Coupling at LHC(8,14)*, *Phys. Lett.* **B728** (2014) 433 [`1311.2931`].

[22] A. Azatov, R. Contino, G. Panico and M. Son, *Effective field theory analysis of double Higgs boson production via gluon fusion*, *Phys. Rev.* **D92** (2015) 035001 [`1502.00539`].

[23] C.-T. Lu, J. Chang, K. Cheung and J. S. Lee, *An exploratory study of Higgs-boson pair production*, *JHEP* **08** (2015) 133 [`1505.00957`].

[24] M. J. Dolan, C. Englert and M. Spannowsky, *Higgs self-coupling measurements at the LHC*, *JHEP* **10** (2012) 112 [`1206.5001`].

[25] A. Papaefstathiou, L. L. Yang and J. Zurita, *Higgs boson pair production at the LHC in the $b\bar{b}W^+W^-$ channel*, *Phys. Rev.* **D87** (2013) 011301 [`1209.1489`].

[26] D. E. Ferreira de Lima, A. Papaefstathiou and M. Spannowsky, *Standard model Higgs boson pair production in the $(b\bar{b})(b\bar{b})$ final state*, *JHEP* **08** (2014) 030 [`1404.7139`].

[27] D. Wardrope, E. Jansen, N. Konstantinidis, B. Cooper, R. Falla and N. Norjoharuddeen, *Non-resonant Higgs-pair production in the $b\bar{b}\,b\bar{b}$ final state at the LHC*, *Eur. Phys. J.* **C75** (2015) 219 [`1410.2794`].

[28] J. K. Behr, D. Bortoletto, J. A. Frost, N. P. Hartland, C. Issever and J. Rojo, *Boosting Higgs pair production in the $b\bar{b}b\bar{b}$ final state with multivariate techniques*, *Eur. Phys. J.* **C76** (2016) 386 [`1512.08928`].

[29] C. Englert, R. Kogler, H. Schulz and M. Spannowsky, *Higgs coupling measurements at the LHC*, *Eur. Phys. J.* **C76** (2016) 393 [`1511.05170`].

[30] F. Bishara, R. Contino and J. Rojo, *Higgs pair production in vector-boson fusion at the LHC and beyond*, *Eur. Phys. J.* **C77** (2017) 481 [`1611.03860`].

[31] Q.-H. Cao, G. Li, B. Yan, D.-M. Zhang and H. Zhang, *Double Higgs production at the 14 TeV LHC and a 100 TeV pp collider*, *Phys. Rev.* **D96** (2017) 095031 [`1611.09336`].

[32] T. Huang, J. M. No, L. Pernié, M. Ramsey-Musolf, A. Safonov, M. Spannowsky et al., *Resonant di-Higgs boson production in the $b\bar{b}WW$ channel: Probing the electroweak phase transition at the LHC*, *Phys. Rev.* **D96** (2017) 035007 [`1701.04442`].

[33] A. Adhikary, S. Banerjee, R. K. Barman, B. Bhattacherjee and S. Niyogi, *Revisiting the non-resonant Higgs pair production at the HL-LHC*, *JHEP* **07** (2018) 116 [1712.05346].

[34] D. Gonçalves, T. Han, F. Kling, T. Plehn and M. Takeuchi, *Higgs boson pair production at future hadron colliders: From kinematics to dynamics*, *Phys. Rev.* **D97** (2018) 113004 [1802.04319].

[35] J. Chang, K. Cheung, J. S. Lee, C.-T. Lu and J. Park, *Higgs-boson-pair production $H(\to b\bar{b})H(\to \gamma\gamma)$ from gluon fusion at the HL-LHC and HL-100 TeV hadron collider*, *Phys. Rev.* **D100** (2019) 096001 [1804.07130].

[36] E. Arganda, C. Garcia-Garcia and M. J. Herrero, *Probing the Higgs self-coupling through double Higgs production in vector boson scattering at the LHC*, *Nucl. Phys.* **B945** (2019) 114687 [1807.09736].

[37] S. Homiller and P. Meade, *Measurement of the Triple Higgs Coupling at a HE-LHC*, *JHEP* **03** (2019) 055 [1811.02572].

[38] ATLAS collaboration, *Combination of searches for Higgs boson pairs in pp collisions at $\sqrt{s}$ =13 TeV with the ATLAS detector*, *Phys. Lett.* **B800** (2020) 135103 [1906.02025].

[39] V. D. Barger, T. Han and R. J. N. Phillips, *Double Higgs Boson Bremsstrahlung From W and Z Bosons at Supercolliders*, *Phys. Rev.* **D38** (1988) 2766.

[40] C. Englert, F. Krauss, M. Spannowsky and J. Thompson, *Di-Higgs phenomenology in $t\bar{t}hh$: The forgotten channel*, *Phys. Lett.* **B743** (2015) 93 [1409.8074].

[41] T. Liu and H. Zhang, *Measuring Di-Higgs Physics via the $t\bar{t}hh \to t\bar{t}b\bar{b}b\bar{b}$ Channel*, 1410.1855.

[42] Q.-H. Cao, Y. Liu and B. Yan, *Measuring trilinear Higgs coupling in WHH and ZHH productions at the high-luminosity LHC*, *Phys. Rev.* **D95** (2017) 073006 [1511.03311].

[43] H. T. Li and J. Wang, *Fully Differential Higgs Pair Production in Association With a W Boson at Next-to-Next-to-Leading Order in QCD*, *Phys. Lett.* **B765** (2017) 265 [1607.06382].

[44] K. Nordström and A. Papaefstathiou, *VHH production at the High-Luminosity LHC*, *Eur. Phys. J. Plus* **134** (2019) 288 [1807.01571].

[45] R. Contino et al., *Physics at a 100 TeV pp collider: Higgs and EW symmetry breaking studies*, *CERN Yellow Rep.* (2017) 255 [1606.09408].

[46] T. Plehn and M. Rauch, *The quartic higgs coupling at hadron colliders*, *Phys. Rev.* **D72** (2005) 053008 [hep-ph/0507321].

[47] T. Binoth, S. Karg, N. Kauer and R. Ruckl, *Multi-Higgs boson production in the Standard Model and beyond*, *Phys. Rev.* **D74** (2006) 113008 [`hep-ph/0608057`].

[48] C.-Y. Chen, Q.-S. Yan, X. Zhao, Y.-M. Zhong and Z. Zhao, *Probing triple-Higgs productions via $4b2\gamma$ decay channel at a 100 TeV hadron collider*, *Phys. Rev.* **D93** (2016) 013007 [`1510.04013`].

[49] W. Kilian, S. Sun, Q.-S. Yan, X. Zhao and Z. Zhao, *New Physics in multi-Higgs boson final states*, *JHEP* **06** (2017) 145 [`1702.03554`].

[50] B. Fuks, J. H. Kim and S. J. Lee, *Scrutinizing the Higgs quartic coupling at a future 100 TeV proton-proton collider with taus and b-jets*, *Phys. Lett.* **B771** (2017) 354 [`1704.04298`].

[51] F. Maltoni, E. Vryonidou and M. Zaro, *Top-quark mass effects in double and triple Higgs production in gluon-gluon fusion at NLO*, *JHEP* **11** (2014) 079 [`1408.6542`].

[52] M. Spira, *Effective Multi-Higgs Couplings to Gluons*, *JHEP* **10** (2016) 026 [`1607.05548`].

[53] D. de Florian and J. Mazzitelli, *Two-loop corrections to the triple Higgs boson production cross section*, *JHEP* **02** (2017) 107 [`1610.05012`].

[54] M. McCullough, *An Indirect Model-Dependent Probe of the Higgs Self-Coupling*, *Phys. Rev.* **D90** (2014) 015001 [`1312.3322`].

[55] M. Gorbahn and U. Haisch, *Indirect probes of the trilinear Higgs coupling: $gg \to h$ and $h \to \gamma\gamma$*, *JHEP* **10** (2016) 094 [`1607.03773`].

[56] G. Degrassi, P. P. Giardino, F. Maltoni and D. Pagani, *Probing the Higgs self coupling via single Higgs production at the LHC*, *JHEP* **12** (2016) 080 [`1607.04251`].

[57] W. Bizon, M. Gorbahn, U. Haisch and G. Zanderighi, *Constraints on the trilinear Higgs coupling from vector boson fusion and associated Higgs production at the LHC*, *JHEP* **07** (2017) 083 [`1610.05771`].

[58] S. Di Vita, C. Grojean, G. Panico, M. Riembau and T. Vantalon, *A global view on the Higgs self-coupling*, *JHEP* **09** (2017) 069 [`1704.01953`].

[59] G. Degrassi, M. Fedele and P. P. Giardino, *Constraints on the trilinear Higgs self coupling from precision observables*, *JHEP* **04** (2017) 155 [`1702.01737`].

[60] G. D. Kribs, A. Maier, H. Rzehak, M. Spannowsky and P. Waite, *Electroweak oblique parameters as a probe of the trilinear Higgs boson self-interaction*, *Phys. Rev.* **D95** (2017) 093004 [`1702.07678`].

[61] C. Degrande, C. Duhr, B. Fuks, D. Grellscheid, O. Mattelaer and T. Reiter, *UFO - The Universal FeynRules Output*, *Comput. Phys. Commun.* **183** (2012) 1201 [`1108.2040`].

[62] J. Alwall, R. Frederix, S. Frixione, V. Hirschi, F. Maltoni, O. Mattelaer et al., *The automated computation of tree-level and next-to-leading order differential cross sections, and their matching to parton shower simulations*, *JHEP* **07** (2014) 079 [`1405.0301`].

[63] T. Hahn and M. Perez-Victoria, *Automatized one loop calculations in four-dimensions and D-dimensions*, *Comput. Phys. Commun.* **118** (1999) 153 [`hep-ph/9807565`].

[64] LHC HIGGS CROSS SECTION WORKING GROUP collaboration, *Handbook of LHC Higgs Cross Sections: 4. Deciphering the Nature of the Higgs Sector*, `1610.07922`.

[65] F. Maltoni, K. Paul, T. Stelzer and S. Willenbrock, *Associated production of Higgs and single top at hadron colliders*, *Phys. Rev.* **D64** (2001) 094023 [`hep-ph/0106293`].

[66] S. Biswas, E. Gabrielli and B. Mele, *Single top and Higgs associated production as a probe of the Htt coupling sign at the LHC*, *JHEP* **01** (2013) 088 [`1211.0499`].

[67] M. Farina, C. Grojean, F. Maltoni, E. Salvioni and A. Thamm, *Lifting degeneracies in Higgs couplings using single top production in association with a Higgs boson*, *JHEP* **05** (2013) 022 [`1211.3736`].

[68] F. Demartin, F. Maltoni, K. Mawatari and M. Zaro, *Higgs production in association with a single top quark at the LHC*, *Eur. Phys. J.* **C75** (2015) 267 [`1504.00611`].

[69] S. Frixione, V. Hirschi, D. Pagani, H. S. Shao and M. Zaro, *Weak corrections to Higgs hadroproduction in association with a top-quark pair*, *JHEP* **09** (2014) 065 [`1407.0823`].

[70] S. Frixione, V. Hirschi, D. Pagani, H. S. Shao and M. Zaro, *Electroweak and QCD corrections to top-pair hadroproduction in association with heavy bosons*, *JHEP* **06** (2015) 184 [`1504.03446`].

[71] J. R. Andersen et al., *Les Houches 2015: Physics at TeV Colliders Standard Model Working Group Report*, in *9th Les Houches Workshop on Physics at TeV Colliders (PhysTeV 2015) Les Houches, France, June 1-19, 2015*, 2016, `1605.04692`, http://lss.fnal.gov/archive/2016/conf/fermilab-conf-16-175-ppd-t.pdf.

[72] D. Pagani, I. Tsinikos and M. Zaro, *The impact of the photon PDF and electroweak corrections on $t\bar{t}$ distributions*, *Eur. Phys. J.* **C76** (2016) 479 [`1606.01915`].

[73] R. Frederix, S. Frixione, V. Hirschi, D. Pagani, H.-S. Shao and M. Zaro, *The complete NLO corrections to dijet hadroproduction*, *JHEP* **04** (2017) 076 [`1612.06548`].

[74] M. Czakon, D. Heymes, A. Mitov, D. Pagani, I. Tsinikos and M. Zaro, *Top-pair production at the LHC through NNLO QCD and NLO EW*, *JHEP* **10** (2017) 186 [`1705.04105`].

[75] V. Hirschi and O. Mattelaer, *Automated event generation for loop-induced processes*, *JHEP* **10** (2015) 146 [`1507.00020`].

[76] K. Arnold et al., *VBFNLO: A Parton level Monte Carlo for processes with electroweak bosons*, *Comput. Phys. Commun.* **180** (2009) 1661 [`0811.4559`].

[77] J. Baglio et al., *VBFNLO: A Parton Level Monte Carlo for Processes with Electroweak Bosons – Manual for Version 2.7.0*, `1107.4038`.

[78] J. Baglio et al., *Release Note - VBFNLO 2.7.0*, `1404.3940`.

[79] A. Papaefstathiou and K. Sakurai, *Triple Higgs boson production at a 100 TeV proton-proton collider*, *JHEP* **02** (2016) 006 [`1508.06524`].

[80] S. Dawson, C. Jackson, L. H. Orr, L. Reina and D. Wackeroth, *Associated Higgs production with top quarks at the large hadron collider: NLO QCD corrections*, *Phys. Rev.* **D68** (2003) 034022 [`hep-ph/0305087`].

[81] X. Zhao, Q. Li, Z. Li and Q.-S. Yan, *Discovery potential of Higgs boson pair production through $4\ell+\not{E}$ final states at a 100 TeV collider*, *Chin. Phys.* **C41** (2017) 023105 [`1604.04329`].

[82] C. G. Lester and D. J. Summers, *Measuring masses of semiinvisibly decaying particles pair produced at hadron colliders*, *Phys. Lett.* **B463** (1999) 99 [`hep-ph/9906349`].

[83] A. Barr, C. Lester and P. Stephens, *m(T2): The Truth behind the glamour*, *J. Phys.* **G29** (2003) 2343 [`hep-ph/0304226`].

[84] A. J. Barr and C. G. Lester, *A Review of the Mass Measurement Techniques proposed for the Large Hadron Collider*, *J. Phys.* **G37** (2010) 123001 [`1004.2732`].

[85] A. J. Barr, T. J. Khoo, P. Konar, K. Kong, C. G. Lester, K. T. Matchev et al., *Guide to transverse projections and mass-constraining variables*, *Phys. Rev.* **D84** (2011) 095031 [`1105.2977`].

[86] W. S. Cho, J. S. Gainer, D. Kim, K. T. Matchev, F. Moortgat, L. Pape et al., *On-shell constrained M_2 variables with applications to mass measurements and topology disambiguation*, *JHEP* **08** (2014) 070 [`1401.1449`].

[87] T. Sjostrand, S. Mrenna and P. Z. Skands, *PYTHIA 6.4 Physics and Manual*, *JHEP* **05** (2006) 026 [`hep-ph/0603175`].

[88] S. Ovyn, X. Rouby and V. Lemaitre, *DELPHES, a framework for fast simulation of a generic collider experiment*, `0903.2225`.

[89] DELPHES 3 collaboration, *DELPHES 3, A modular framework for fast simulation of a generic collider experiment*, *JHEP* **02** (2014) 057 [`1307.6346`].

[90] M. Cacciari, G. P. Salam and G. Soyez, *The anti-k_t jet clustering algorithm*, *JHEP* **04** (2008) 063 [`0802.1189`].

[91] M. Cacciari, G. P. Salam and G. Soyez, *FastJet User Manual*, *Eur. Phys. J.* **C72** (2012) 1896 [`1111.6097`].

[92] L. Di Luzio, R. Gröber and M. Spannowsky, *Maxi-sizing the trilinear Higgs self-coupling: how large could it be?*, *Eur. Phys. J.* **C77** (2017) 788 [`1704.02311`].

[93] P. Nogueira, *Automatic Feynman graph generation*, *J. Comput. Phys.* **105** (1993) 279.

[94] J. A. M. Vermaseren, *New features of FORM*, `math-ph/0010025`.

[95] G. Degrassi, P. P. Giardino and R. Gröber, *On the two-loop virtual QCD corrections to Higgs boson pair production in the Standard Model*, *Eur. Phys. J.* **C76** (2016) 411 [`1603.00385`].

[96] S. Borowka, G. Heinrich, S. Jahn, S. P. Jones, M. Kerner, J. Schlenk et al., *pySecDec: a toolbox for the numerical evaluation of multi-scale integrals*, *Comput. Phys. Commun.* **222** (2018) 313 [`1703.09692`].

[97] S. Borowka, G. Heinrich, S. Jahn, S. P. Jones, M. Kerner and J. Schlenk, *Numerical evaluation of two-loop integrals with pySecDec*, *Acta Phys. Polon. Supp.* **11** (2018) 375 [`1712.05755`].

[98] J. Berntsen, T. O. Espelid and A. Genz, *Algorithm 698: DCUHRE: An adaptive multidimensional integration routine for a vector of integrals*, .

[99] G. P. Lepage, *A New Algorithm for Adaptive Multidimensional Integration*, *J. Comput. Phys.* **27** (1978) 192.

[100] M. Jacob and G. C. Wick, *On the General Theory of Collisions for Particles with Spin*, *Annals Phys.* **7** (1959) 404.

[101] S. Dulat, T.-J. Hou, J. Gao, M. Guzzi, J. Huston, P. Nadolsky et al., *New parton distribution functions from a global analysis of quantum chromodynamics*, *Phys. Rev.* **D93** (2016) 033006 [`1506.07443`].

[102] W. Bizoń, U. Haisch and L. Rottoli, *Constraints on the quartic Higgs self-coupling from double-Higgs production at future hadron colliders*, *JHEP* **10** (2019) 267 [`1810.04665`].

[103] ATLAS COLLABORATION collaboration, *Study of the double Higgs production channel $H(\to b\bar{b})H(\to \gamma\gamma)$ with the ATLAS experiment at the HL-LHC*, Tech. Rep. ATL-PHYS-PUB-2017-001, CERN, Geneva, Jan, 2017.

[104] H. Abramowicz et al., *Higgs physics at the CLIC electron–positron linear collider*, *Eur. Phys. J.* **C77** (2017) 475 [`1608.07538`].

[105] F. Boudjema and E. Chopin, *Double Higgs production at the linear colliders and the probing of the Higgs selfcoupling*, *Z. Phys.* **C73** (1996) 85 [`hep-ph/9507396`].

[106] S. Di Vita, G. Durieux, C. Grojean, J. Gu, Z. Liu, G. Panico et al., *A global view on the Higgs self-coupling at lepton colliders*, *JHEP* **02** (2018) 178 [`1711.03978`].

[107] F. Maltoni, D. Pagani, A. Shivaji and X. Zhao, *Trilinear Higgs coupling determination via single-Higgs differential measurements at the LHC*, *Eur. Phys. J.* **C77** (2017) 887 [`1709.08649`].

[108] A. A. Sokolov and I. M. Ternov, *On polarization and spin effects in the theory of synchrotron radiation*, *Sov. Phys. Dokl.* **8** (1964) 1203.

[109] PARTICLE DATA GROUP collaboration, *Review of Particle Physics*, *Chin. Phys.* **C40** (2016) 100001.

[110] A. Denner, S. Dittmaier, M. Roth and M. M. Weber, *Electroweak radiative corrections to single Higgs boson production in e+ e- annihilation*, *Phys. Lett.* **B560** (2003) 196 [`hep-ph/0301189`].

[111] A. Denner, S. Dittmaier, M. Roth and M. M. Weber, *Electroweak radiative corrections to $e^+e^- \to \nu\bar{\nu}H$*, *Nucl. Phys.* **B660** (2003) 289 [`hep-ph/0302198`].

[112] J. Tian, *Study of Higgs self-coupling at the ILC based on the full detector simulation at $\sqrt{s}$ = 500 GeV and $\sqrt{s}$ = 1 TeV*, in *Helmholtz Alliance Linear Collider Forum: Proceedings of the Workshops Hamburg, Munich, Hamburg 2010-2012, Germany*, (Hamburg), pp. 224–247, DESY, DESY, 2013.

[113] T. Hahn, *Generating Feynman diagrams and amplitudes with FeynArts 3*, *Comput. Phys. Commun.* **140** (2001) 418 [`hep-ph/0012260`].

[114] R. K. Ellis and G. Zanderighi, *Scalar one-loop integrals for QCD*, *JHEP* **02** (2008) 002 [`0712.1851`].

[115] S. Carrazza, R. K. Ellis and G. Zanderighi, *QCDLoop: a comprehensive framework for one-loop scalar integrals*, *Comput. Phys. Commun.* **209** (2016) 134 [`1605.03181`].

[116] M. Ahmad et al., *CEPC-SPPC Preliminary Conceptual Design Report. 1. Physics and Detector*, .

[117] TLEP DESIGN STUDY WORKING GROUP collaboration, *First Look at the Physics Case of TLEP*, *JHEP* **01** (2014) 164 [`1308.6176`].

[118] H. Baer, T. Barklow, K. Fujii, Y. Gao, A. Hoang, S. Kanemura et al., *The International Linear Collider Technical Design Report - Volume 2: Physics*, `1306.6352`.

[119] CLIC, CLICDP collaboration, *Updated baseline for a staged Compact Linear Collider*, `1608.07537`.

[120] H. Abramowicz et al., *The International Linear Collider Technical Design Report - Volume 4: Detectors*, `1306.6329`.

[121] V. Shiltsev, *Future Muon Colliders, Higgs and Neutrino Factories*, in *Modern Muon Physics: Selected issues*, (2019), DOI.

[122] D. Schulte, "Conceptual design and future plans." talk at the 105th Plenary ECFA meeting, 2019.

[123] M. Moretti, T. Ohl and J. Reuter, *O'Mega: An Optimizing matrix element generator*, `hep-ph/0102195`.

[124] W. Kilian, T. Ohl and J. Reuter, *WHIZARD: Simulating Multi-Particle Processes at LHC and ILC*, *Eur. Phys. J.* **C71** (2011) 1742 [`0708.4233`].

[125] S. Borowka, C. Duhr, F. Maltoni, D. Pagani, A. Shivaji and X. Zhao, *Probing the scalar potential via double Higgs boson production at hadron colliders*, *JHEP* **04** (2019) 016 [`1811.12366`].